ABSTRACT

Title of Dissertation: METAL SULFIDES FOR HIGH PERFORMANCE

LITHIUM ION AND SODIUM ION BATTERY ANODES

Jingjing Wang, Doctor of Philosophy, 2015

Directed By: Professor Alice C. Mignerey

Department of Chemistry and Biochemistry

Professor Chunsheng Wang (Co-advisor)

Department of Chemical and Biomolecular Engineering

The research described in this dissertation aims to develop facile synthetic routes to fabricate carbon coated metal sulfides (SnS, SnS_2, MoS_2) with sophisticated nanostructure to achieve high capacity and long cycle life in Li-ion and Na-ion batteries, and provide in-depth understanding on their electrochemical behavior.

In this study, a simple solid-state reaction method to synthesize carbon coated tin sulfides (SnS/C, SnS_2/C) nanomaterials was developed, which enables feasible large-scale production for the wide application of battery technology. The as-prepared SnS/C nanospheres exhibit high capacity (900 mAh/g) and long cycle life (200 cycles) at a current density of 227 mA/g in

lithium ion batteries. Tin disulfide (SnS_2) with larger layer distance (5.9 Å) as compared with SnS (3.4 Å) was chosen as an anode material in Na-ion batteries. The as-prepared SnS_2/C nanospheres from solid-state synthesis deliver a high reversible capacity (~600 mAh/g) for hundreds of cycles, demonstrating one of the best cycling performances in all reported SnS_2/C anodes for Na-ion batteries to date. Mechanism studies demonstrate that the superior cycling stability of the SnS_2/C electrode is attributed to the stable nanosphere morphology and structural integrity during charge/discharge cycles.

The MoS_2/C composite with nanoflower morphology was fabricated from a hydrothermal method. MoS_2/C nanomaterials deliver a reversible capacity of 520 mAh/g at 67 mA/g and maintain at 400 mAh/g for 300 cycles at a high current density of 670 mA/g. The stable cycling performance and high coulombic efficiency (~100%) of MoS_2/C nanospheres are ascribed to the highly reversible conversion reaction of MoS_2 during sodiation/desodiation and the formation of a stable solid electrolyte interface (SEI) layer. The MoS_2/C nanomaterial is also synthesized using a one-step spray pyrolysis in which sucrose serves as a carbon source. The MoS_2/C nanomaterials from spray pyrolysis exhibit higher capacity and stable cycling performance in Na-ion batteries. Spray-pyrolysis synthesized MoS_2/C nanomaterials are robust to withstand the volume change during charge/discharge cycles, as evidenced by the stable interface resistance in electrochemical impedance spectroscopy (EIS) analysis and good morphology maintenance after cycling in scanning electron microscopy (SEM) image.

METAL SULFIDES FOR HIGH PERFORMANCE LITHIUM ION AND SODIUM ION BATTERY ANODES

By

Jingjing Wang

Dissertation submitted to the Faculty of the Graduate School of the

University of Maryland, College Park, in partial fulfillment

of the requirements for the degree of

Doctoral of Philosophy

2015

Advisory Committee:

Professor Alice C. Mignerey, Committee Chair

Professor Chunsheng Wang

Professor Sang Bok Lee

Professor Amy Mullin

Professor Bao Yang

Dedicated to Chao Luo, Michelle Luo,

Runzhen Xiong and Honggui Luo,

love never sleeps.

Acknowledgements

I really appreciate the help and contributions of my advisor-Professor Alice Mignerey and co-advisor, Professor Chunsheng Wang for their guidance during my Ph.D. period. I am truly grateful to my advisor since she respects my research interests and always pays attention to what I am doing. To me, she is not only my mentor, but also a caring and respectable family elder. I would like to acknowledge my co-advisor, and during my stay in his research group, I have learn a lot from him about how to be a professional researcher in the field of energy storage. He was born to be a brilliant scientist and I was impressed by his diligence, research ideas and critical thinking. Many thanks to Professor Mignerey and Professor Wang again, without their support and contributions to my work, I could not achieve what I have done. I would like to thank my committee members: Professor Sang Bok Lee, Professor Amy Mullin, Professor Zhihong Nie and Professor Bao Yang for their attention and suggestions to my work.

I would like to acknowledge my colleagues, especially Chao Luo, Dr. Yujie Zhu, Dr. Xiulin Fan, Dr. Jianfeng Mao, Tao Gao, Fudong Han, Dr. Huili Liu, Dr. Liumin Suo , Xiwen Wang, Dr. Marguerite Belt Tonjes, Owen Barron, Chris Ferraioli, Jaime Gomez, Jack Goodell, and Ashley Sexton. As coworkers, they are helpful and would like to offer valuable suggestions to my work. As friends, they are very considerate and would like to share every happiness and toughness. I feel so lucky to have you guys stay around during my Ph.D. period. I would like to thank my other friends: Dr. Huizhi Bai, Junkai Hu, Yue Zheng, kaitlyn Crawford, Lu Liu and Mijin Kim and the friendship between us is a great asset to me.

I am truly grateful to my husband, Chao Luo, my two-year old daughter, Michelle Luo, my parents, Tao Wang and Caiyu Gao, my brother, Jianghao Wang and my parents-in-law, Runzhen

Table of Contents

Chapter 1 Introduction

1.1 Li-ion batteries

Li-ion batteries (LIBs) are commercial devices for portable electronics and have a potential for plug-in hybrid electric vehicles (HEVs) and electrical vehicles (EVs) [1,2]. The working principle of Li-ion batteries is expressed in Figure 1.1 [3]. A typical Li-ion battery contains a positive electrode (cathode) such as $LiCoO_2$, a negative electrode (anode) such as graphite, a porous separator to prevent short-circuit, and an electrolyte to allow fast ion transport. The current collectors, aluminum foil on the cathode and copper foil on the anode, deliver electrons from the redox centers of the electrodes to the external circuit. When discharging, lithium ions move from the anode and insert into the cathode. The active material in the anode is oxidized, while the cathode material is reduced by accepting electrons. Upon charging, lithium ions transport from the cathode to the anode, and the active material in the anode gets reduced because of accepting electrons. The Li-ion battery is considered to be rechargeable since the discharge/charge process is reversible by restoring the chemical energy.

The electrochemical performance of the electroactive materials in LIBs is normally evaluated with coin-cells in the laboratory. The standard electrochemical tests include galvanostatic charge/discharge and cyclic voltammetry (CV). A typical coin-cell setup contains a stainless steel case, a spring, two-electrode configuration, where the working electrode is the active material and the counter electrode is metallic lithium (a half-cell configuration), a separator between the two electrodes, and an electrolyte. A separator is used to avoid the electrical contact between the working and counter electrodes. The electrolyte contains lithium salts ($LiPF_6$)

dissolved in organic solvent (alkyl carbonates), and has a working potential in the range of 0.8-4.5 V. An ideal Li-ion battery has high energy and power density, long cycle life, chemical stability and safety. The cycle life is defined as the number of complete charge/discharge cycles that the battery is able to maintain its capacity at 80% of its original capacity. The energy density of Li-ion batteries, which is expressed by either per unit of weight (W h kg^{-1}) or per unit of volume (W h L^{-1}), can be calculated in a function of the specific capacity and voltage difference between the cathode and anode. Due to the light weight of lithium metal and high reduction potential of Li^+/Li, the Li-ion battery is considered to have the highest energy density to date. Nowadays, the urgent energy demands in large-scale application of electric vehicles give rise to the need for high performance Li-ion batteries with high specific capacity and long cycle life.
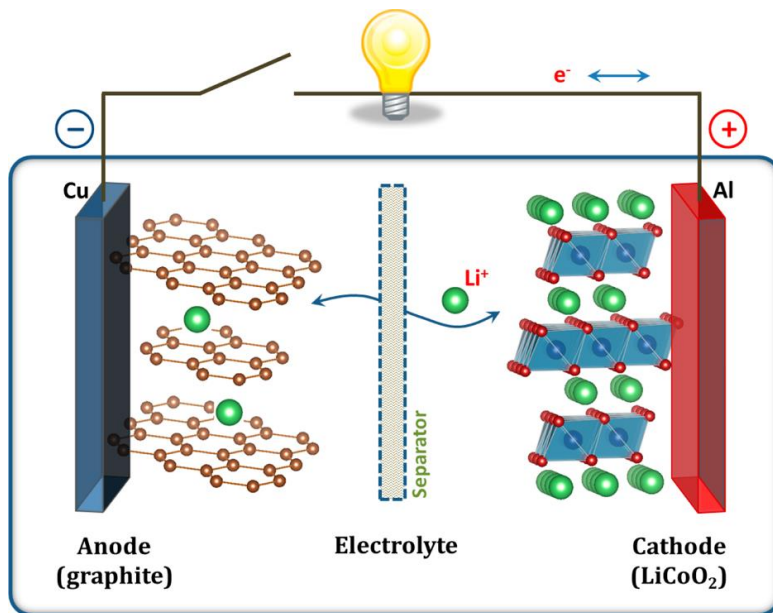
Figure 1.1 Schematic illustration of the working principle of Li-ion batteries [3].

The commercialized Li-ion batteries use $LiCoO_2$ as the cathode material and graphite as the anode material via an intercalation/de-intercalation mechanism. However, the low theoretical

capacity of commercial graphite anodes (372 mAh/g) and $LiCoO_2$ cathodes (137 mAh/g) are unable to power the next generation of energy supply devices [4]. As a consequence, it is of great significance to search for alternative electrode materials with high specific capacity and energy density.

1.2 Anode materials in Li-ion batteries

The research for advanced anode materials is important for large-scale application of Li-ion batteries and has received extensive attention in the past decades [5-7]. The selection of an anode material in Li-ion batteries is dependent on the electroactive sites, suitable working potential, electrical conductivity, cost, chemical stability, and many other factors. Lithium metal was considered as an ideal anode material due to its lowest potential, light weight and extremely high theoretical capacity (3860 mAh/g). However, the formation of lithium dendrites when using lithium metal in contact with organic electrolytes causes thermal runaway, and thus hinders its practical application in LIBs [8]. Due to such safety issues, considerable research attention has been given to alternative candidates. Among them, carbonaceous materials, which can be categorized as graphitic carbon and non-graphitized soft/hard carbon, are the primary candidates and have been commercialized in consumer electronics such as Li-ion battery anode materials.

Graphite can achieve stable cycling performance in Li-ion batteries after introducing ethylene carbonate as a non-aqueous electrolyte. The theoretical capacity of graphite is 372 mAh/g based on the calculation that one lithium ion reacts with six C-atoms in a completely reversible intercalation/de-intercalation process ($Li^+ + C_6 + e^- \rightarrow LiC_6$). The layered structure of graphite provides favorable active sites for lithium ions to intercalate and de-intercalate without causing

3

particle pulverization and mechanical strains, and thus stable cycling performance can be achieved. The non-graphitic soft carbon exists as amorphous structures such as coke and carbon black, and the capacity of such carbonaceous material is relatively low ($xLi^+ + C_6 + xe^- \rightarrow Li_xC_6$, x ~0.5-0.8) [9-11]. Even though hard carbons have higher specific capacity ($xLi^+ + C_6 + xe^- \rightarrow Li_xC_6$, x ~1.2-5), their electrochemical performance in LIBs is constrained by the poor electrical conductivity and irreversible capacity loss [12,13]. Therefore, the low capacity of graphite and soft carbons and the cycling instability of hard carbons cannot meet the industrial requirements in which a capacity higher than 600 mAh/g must be maintained for hundreds of cycles. In recent years, many efforts have been devoted to searching for alternative anode materials with higher capacities than carbonaceous materials.

Metal oxides are investigated as the alternative choice as anode materials in LIBs due to the high specific capacities. Table 1 compares the synthetic routes and electrochemical performance of recently reported metal sulfides [14]. Among them, tin oxides received intensive attention owing to high theoretical capacity, inexpensive cost, and less toxicity as compared with other candidates (Co_3O_4, NiO) [14,15]. In 1997, Idota *et. al.* proposed tin-based amorphous oxide (TCO) as a high-capacity Li-ion battery in which Sn-O as the electroactive site shows a reversible capacity of 500-600 mAh/g [16]. After that, tin oxides were extensively investigated as promising candidates to replace graphite due to its high theoretical capacity as a Li-ion battery anode. The theoretical capacity can reach ca.790 mAh/g based on the reaction mechanism of SnO_2 with lithium ions expressed in a two-step reaction:

$$SnO_2 + 4Li^+ + 4e^- \rightarrow Sn + 2Li_2O \qquad (1.1)$$

$$Sn + 4.4Li^+ + 4.4e^- \leftrightarrow Li_{4.4}Sn \qquad (1.2)$$
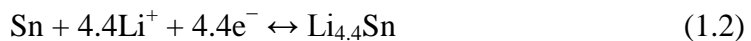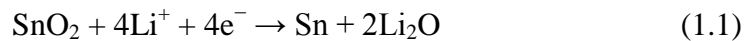
Many efforts have been devoted to fabricating various nanostructured SnO_2, such as nanorods, nanotubes and nanospheres [17-20]. In 2006, Lou *et al.* synthesized SnO_2 hollow nanospheres with a facile one-pot template-free synthesis technique, and the as-prepared SnO_2 nanospheres deliver a charge capacity as high as 1140 mAh/g at a current density of 0.2 C [21]. However, the capacity decays to 645 mAh/g within 40 cycles. Graphene was introduced to form SnO_2/graphene nanoporous electrodes [15]. The design principle is that the nanopores could serve as a buffer space to alleviate volume expansion during lithiation. The experimental observation shows that the novel anode material delivers stable cycling performance in 30 cycles. In 2009, Lou *et al.* prepared coaxial SnO_2/C hollow nanospheres in which carbon is introduced as a physical matrix to buffer the volume expansion. The newly formed SnO_2/C nanospheres can be cycled for hundreds of cycles in Li-ion batteries, while the capacity fading is still observable from ca. 600 mAh/g to 500 mAh/g [22]. The capacity fading is attributed by the large volume expansion stemming from the alloying reaction between Sn and multiple lithium ions (reaction 1, 2). Such intrinsic problems hinder the feasibility of SnO_2 nanoparticles to be used for high performance Li-ion battery anodes.

Table 1.1 Synthetic strategies and electrochemical properties of metal oxides based anode materials in lithium ion rechargeable batteries [14]

Sample	Synthesis method	Specific capacity (mAh/g)	# Cycles
SnO_2	Hydrothermal	> 800	100
TiO_2	Sol-gel process	288	300
MnO_2	Solution method	ca.600	60
α-Fe_2O_3	Hydrothermal	1000	50
Fe_3O_4	Microwave irradiation	650	50
Co_3O_4	Spray pyrolysis	750	100
NiO	Controlled chemical synthesis	410	40

Metal sulfides (MS, MS_2) with layered structure exhibit superior lithium storage capability since the interlayer space facilitates the initial intercalation of lithium ions [23-25]. A typical layered metal sulfide has a lamellar structure with each layer stacking via van der Waals interactions. The single layer consists of numerous S-M-S units, where the metal atoms are sandwiched in the center by sulfur atoms. The recent studies on the electrochemical properties of molybdenum disulfide (MoS_2), tungsten disulfide (WS_2), zirconium disulfide (ZrS_2) and tin monosulfide (SnS) are compared in Table 1.2 [14,26-29].

Table 1.2 Synthetic strategies and electrochemical properties of metal sulfides based anode materials in lithium ion rechargeable batteries [14]

Sample	Synthesis	Specific Capacity (mAh/g)	# Cycles
MoS_2	Hydrothermal	900-1000	80
WS_2	Solid-state reaction	600	100
ZrS_2	Surfactant-assisted chemical synthesis	600	50
TiS_2	Grinding method	340	20
SnS	*In-situ* polymerization	891	500

The MoS_2 nanomaterial synthesized from the hydrothermal method exhibits a specific capacity of 900-1000 mAh/g in LIBs and can be maintained for ~80 cycles [26]. Liu *et al.* reported the synthesis of SnS@polyprrole-nanobelt/carbon-nanotube (SnS@PPy-NB/CNT) and the newly formed anode shows a specific capacity of 891 mA h g^{-1} after 500 cycles at a current density of 1 C in Li-ion batteries [30]. As shown in Table 1.2, other layered metal sulfides (WS_2, ZrS_2, TiS_2) show poor cycling performance as compared with MoS_2 and SnS. The recent studies on MoS_2 and SnS with sophisticated nanostructure design have contributed to state-of-the-art anodes for LIB applications. Based on the fact that the layered structure of MoS_2 enables easier intercalation of lithium ions into the gallery between MoS_2 layers, a high-energy-density and stable Li-ion battery anode has been developed with two-dimensional MoS_2 nanowall by S. Mitro *etc*, which delivers a capacity of 880 mAh/g for 50 cycles [23]. Chen *et al.* introduced carbon nanotubes (CNT) to MoS_2 crystal structure and fabricated MoS_2/CNT nanoflakes for LIB

anodes [31]. The novel electrode exhibits a high capacity of approximately 993 mAh/g for hundreds of cycles, and it is able to preserve its morphology after cycling.

Recently, a facile synthesis of SnS nanobelts with a length/thickness ratio of 100 was developed in consideration that the flexible nanobelts could withstand large volume changes [32]. The specific capacity can be maintained at 500 mAh/g for 50 cycles. Im *et al.* compared the electrochemical performance of metallic Sn, SnO_2 and SnS, in which SnS nanomaterial shows the highest reversible capacity (880 mAh/g) after 70 cycles [33]. The findings from previous studies demonstrate the potential of SnS and MoS_2 and pave the way for the feasibility of high-performance Li-ion batteries.

1.3 Na-ion batteries

Rechargeable Li-ion batteries have been considered the primary candidate to power consumer electronics and the next generation of hybrid electric vehicles (HEVs) because of their light weight and high energy density. However, with higher cost and less abundant distribution of lithium as a resource, it is necessary to search for alternative chemistry to replace LIBs. Table 1.3 lists the comparison between sodium and lithium elements [34]. The sodium ion battery (SIB) is considered as the primary choice due to its similar working principle with LIBs, low cost, and easier access to sodium on the earth. However, the energy density of Na-ion batteries would not exceed that of LIBs because of the higher weight, larger ion radius and lower reducing voltage of sodium as compared with lithium. In recent years, Na-ion batteries have attracted much research attention, especially for large-scale electric energy storage (EES) applications, in which high energy density is not a necessary requirement. The application of EES is also called grid energy

storage. It can store electrical energy from peak periods and is beneficial for peak load management.

Table 1.3 The comparison between Na and Li elements [34]

	Na	Li
Cation radius	97 pm	68 pm
Atomic weight	23 g mol^{-1}	6.9 g mol^{-1}
E_o vs. SHE	-2.7 V	-3.04 V
A-O coordination	Octahedral or prismatic	Octahedral or tetrahedral
Melting point	97.7 °C	180.5 °C
Distribution	Everywhere	70% in South America
Price, carbonates	~$ 0.3 per kg	~$ 6.5 per kg

The working principle of SIBs is similar to that of LIBs. A sodium ion battery based on the intercalation mechanism consists of a cathode with layered structure, a high-capacity anode with alloying mechanism with sodium ions, and organic electrolytes with dissolved sodium salts ($NaPF_6$) [35]. As shown in Fig. 1.2, during discharging, sodium ions transport from the anode and insert into the cathode. The active anode material is oxidized while the cathode material is reduced by accepting sodium ions and electrons. Upon charging, sodium ions extract from the cathode to the anode, and the active material in the anode gets reduced, accepting sodium ions and electrons. In both cases, electrons flow in the opposite direction to sodium ions and can be

delivered from the redox centers to the external circuit by current collectors, such as aluminum foil on the cathode and copper foil on the anode. The reversible movement of sodium ions and the reaction between electrode materials with sodium ions enable the conversion of chemical energy to electrical energy, which is the primary function of battery systems.
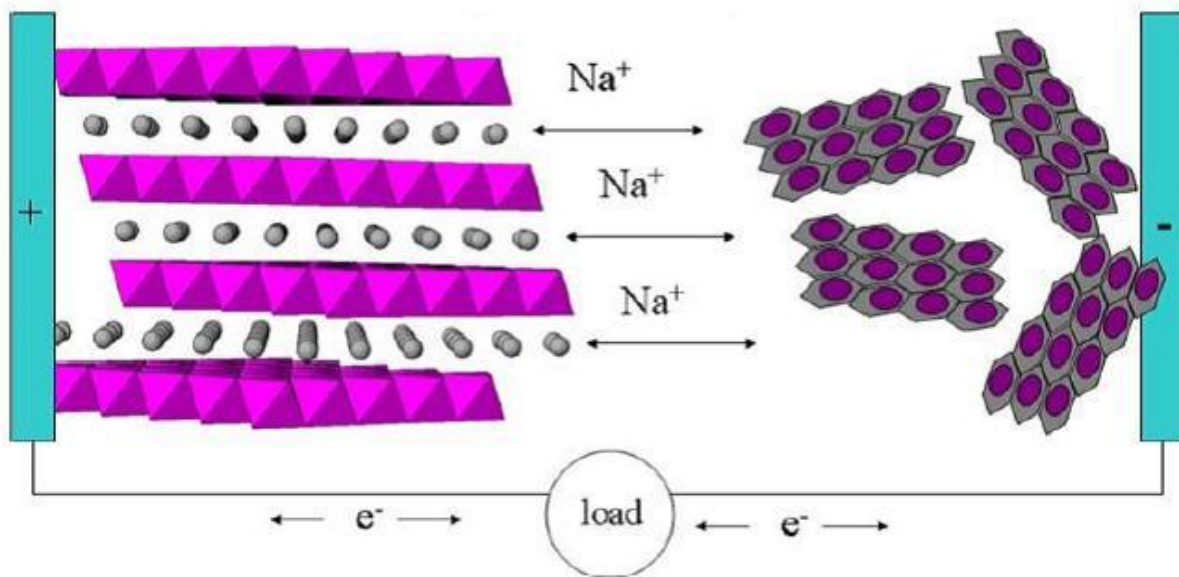
Figure 1.2 Schematic illustration of the working principle of sodium ion batteries [35].

1.4 The challenges of Na-ion batteries

The intercalation chemistry of Na-ion batteries is more complicated than that of Li-ion batteries because of the larger cation radius (1.02 Å) of sodium and its general preference for octahedral or prismatic coordination. Therefore, not many crystalline materials can be used as Na intercalation electrode materials and achieve a stable function in Na-ion batteries.
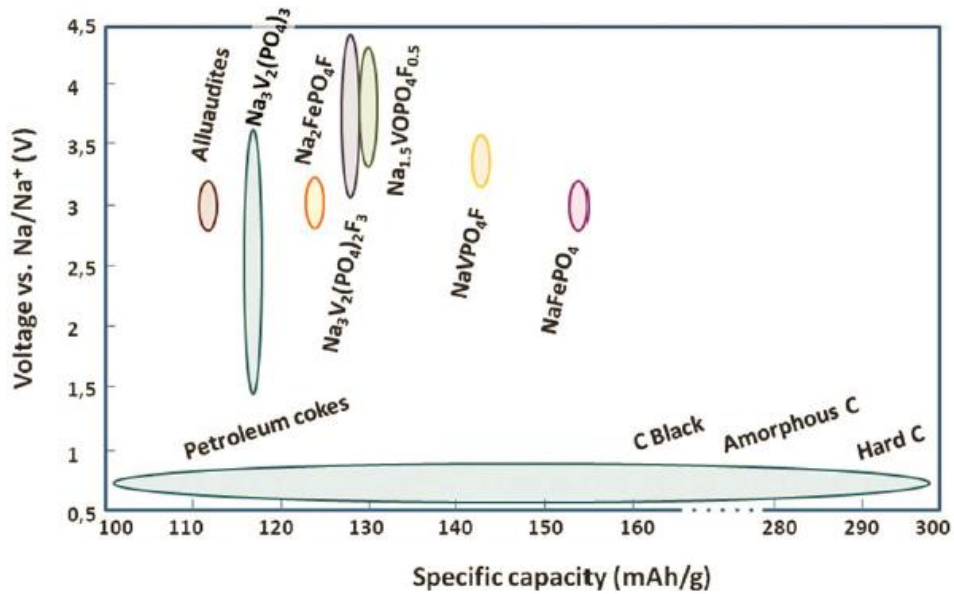
Figure 1.3 Most important cathode and anode materials for Na-ion battery applications [36].

As shown in Fig. 1.3 [36], the proposed cathode materials include layered crystalline chemicals such as $Na_3V_2(PO_4)_3$, and $NaFePO_4F$, which have high working potential vs. Na^+/Na (V), while the anode is mainly composed of different forms of carbon with a low voltage plateau under 1 V. The reasons behind the limited choices for Na-ion battery applications are manifold: (1) more difficult Na insertion chemistry due to larger ion size as compared with Li; (2) slow Na diffusion kinetics in intercalation materials, which is related to the large size of sodium ion; (3) the formation of a solid electrolyte interface (SEI) layer on the surface of electrodes; The formation of a SEI layer mainly happens on the anode because typical electrolytes are not stable at the low operating potential of the anode during cycling. SEI growth results from irreversible electrochemical decomposition of the electrolyte, and it leads to the loss of lithium/sodium, gradual capacity fading, and a more complicated charge transfer processes on the electrolyte-electrode interface and sodium ion transport through the the SEI layer. (4) large volumetric expansion of Na alloys during charging/discharging. Anode candidates, such as metallic tin can

11

alloy with multiple sodium ions, but such alloying results in large volume change and particle pulverization and thus capacity fading is inevitable. Because of these challenges, it is not practical to simply borrow recently developed electrode materials from lithium storage systems for Na-ion battery applications.

1.5 Recent progress for Na-ion battery anodes

To advance the implementation of Na-ion battery technology, it is significant to develop high capacity electrode materials with stable sodium storage capability. In the study of cathode materials, many attempts have been developed by simply replacing lithium as sodium in order to search for a promising cathode candidate for Na-ion batteries. However, the challenges brought by the large size of Na ion render such common routes in cathode research impossible for anodes as evidenced by the intercalation failure of sodium ions into graphite.

1.5.1 Carbon-based material

Graphite, which is the most common and commercialized anode material in LIBs, cannot be intercalated by sodium ions, indicating a complex intercalation process in Na-ion batteries. Only until recently, Yang *et al.* reported that expended graphite with a larger interlayer distance of 4.3 Å could be used for Na-ion battery anode, and delivers a capacity of 183 mAh/g at a current density of 100 mA/g [37].

Among other carbonaceous materials, hard carbon is still the primary choice, even though its cycling performance is not competitive according to commercial requirements. After Steven and Dahn demonstrated the high capacity of hard carbon (300 mAh/g) in Na-ion batteries [38], their

group further investigated the sodium insertion behavior with a solid state ^{23}Na NMR study, in which the Na insertion into layered gallery and nanopore sites of hard carbon was observed in charge/discharge curves [39]. Recent approaches in improving the cycling stability of hard carbon were reported by Amine *et al.* [40]. The fabrication of hard carbon was achieved by different routes and it is found that the hard carbon sample from pyrolysis of polyvinyl chloride (PVC) nanofibers at high temperature exhibits the best cycling performance with a reversible capacity of 271 mAh/g for 150 cycles in Na-ion batteries. It indicates that a proper carbon source, a suitable fabrication temperature, and nanostructure fabrication is important for Na-ion battery applications.

1.5.2 Na-alloys

The potential of group 14 elements in the periodic table to be used as Na-alloys in battery applications was first investigated by Cedar *et al.* [41]. Failed attempts were made for Si and Ge in which no electrochemical activity was found, while the investigation of metallic Sn demonstrated successful cycling with high capacity [42,43]. After that, metallic Sn was realized as a promising candidate for a Na-ion battery anode with an alloying reaction mechanism.

A representative study of metallic Sn is the structural evolution of Sn nanoparticles during sodiation as reported by Wang *et al.* [44]. It is found that Sn nanoparticles can alloy with Na ions to form $Na_{15}Sn_4$ (x = 3.75) via a single phase mechanism in two steps. They conducted *in-situ* TEM studies and the results are significant to show the volumetric expansion of Sn (420%) during sodiation (Fig. 1.4). In their study, Sn nanoparticles show excellent cycling performance without observable particle pulverization and cracks, as evidenced by electron microscopy.

Based on such inspiring findings, increasing research activity has flourished around metallic Sn with sophisticated nanostructure design and fabrication as a Na-ion battery anode.
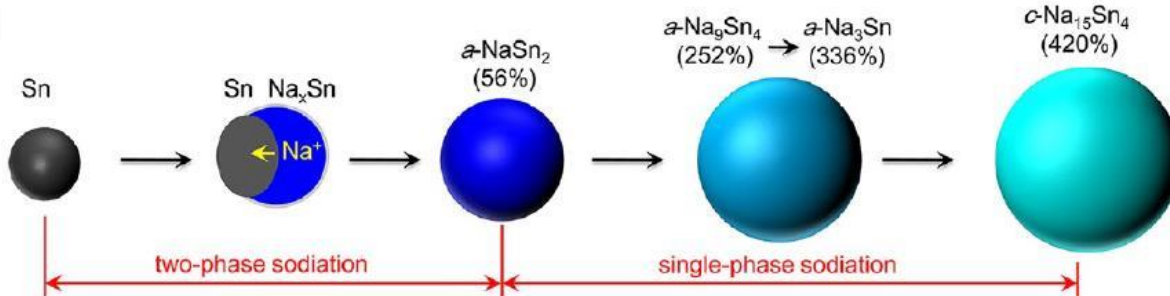
Figure 1.4 Schematic illustration of the structural evolution of Sn during the sodiation [44].

An interesting study was conducted with tin coated viral nanoforests as sodium-ion battery anodes [45]. The Sn nanorods with a unique core-shell structure were fabricated on viral scaffolds and deliver a specific capcity of 405 mAh/g after 150 deep galvanastic cycles. The superior electrochemical performance is attributed to the vertical nanorod assembly design and the additional carbon coating on the surface, which can suppress the volumetric expansion during sodiation. Inspired by these findings, natural wood fiber was developed as a mechanical buffer for a tin anode as reported by Zhu *et al.* [46]. It is pointed out that the softness of the hierarchical wood fiber substrate accommodates the volumetric expansion of the Sn anode, and thus a stable cycling performance was experimentally observed for hundreds of cycles.

1.5.3 Metal oxides and metal sulfides

The research interest on metal oxides was elevated after SbO_2 was reported to show an extremely high reversible capacity (800 mA h g^{-1}) in Na-ion batteries via a conversion reaction mechanism, followed by alloying reactions with sodium ions [47]. The conversion reactions offer an attractive range of large theoretical specific capacities, which enables those metal oxides as

promising Na-ion battery anodes. Among them, SnO_2 is considered as a promising candidate because of its abundance, low cost, high theoretical capacity (1378 mAh g^{-1}), and nontoxic nature [48]. Extensive research has been conducted based on the sodiation mechanism [49]:

$$SnO_2 + Na^+ + e^- \rightarrow NaSnO_2 \qquad (1.3)$$

$$NaSnO_2 + 3Na^+ + 3e^- \rightarrow 2Na_2O + Sn \qquad (1.4)$$

$$Sn + (9/4) Na^+ + (9/4)e^- \rightarrow Na_9Sn_4 \qquad (1.5)$$
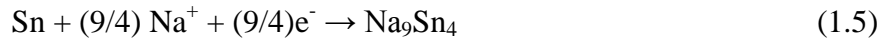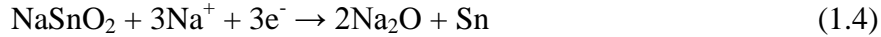
However, a technological bottleneck still exists as the large volume change during charge/discharge results in rapid capacity fading. Recent strategies in addressing this issue focus on introducing carbonaceous material as a wrapping matrix to accommodate the volume change. Wang *et al.* reported SnO_2@graphene nanocomposites in which the active material SnO_2 are anchored on graphene nanosheets, as determined by electron microscopy [48]. The SnO_2/graphene electrode delivers approximately 700 mAh/g for 100 cycles, which is higher than the reversible capacity of pure SnO_2 nanomaterial. It was pointed out that individual SnO_2 nanocrystals were wrapped by flexible and conductive graphene nanosheets and contributed to the better electrochemical performance of SnO_2/graphene nanocomposites. However, the challenges of using SnO_2 for large-scale Na-ion battery implementation are two-fold. First, even though the theoretical capacity is as high as 1378 mAh/g, it is impossible to maintain such a high reversible capacity after deep galvanastic cycling, since only the alloying reaction can undergo reversible de-alloying process and the conversion reaction (Eq. 1.4) is not reversible during desodiation. Secondly, even though the large volume change can be accommodated by introducing graphene or carbon matrix and sophisticated nanostructure growth, the cycling stability is still far from the industry standards, and the rigorous synthetic routes for delicate nanostructures are out of cost

expectation for practical applications. Other metal oxides, such as iron oxides, face the same challenges as the large volume change during sodiation results in rapid particle agglomeration and thus hinders the implementation of Na-ion batteries.

Guided by the successful attempts of metal sulfides as LIB anodes, they are proposed as promising candidates for Na-ion battery anodes. Recently, molybdenum disulfide (MoS_2) is predominantly investigated since it is one of two-dimensional transitional metal dichalcogenides (TMDs) whose structure is akin to graphite. Park *et al.* first reported commercial MoS_2 bulk material for a sodium-ion battery anode, which delivers a reversible capacity of 85 mAh/g after 100 cycles [50]. They proposed an intercalation discharge mechanism of MoS_2/Na determined by the distorted MoS_2 structures and X-ray diffraction (XRD) characterization. A more extensive study on MoS_2 was reported later by David *et al.* with evidence for a conversion mechanism for the sodiation/desodiation process in the MoS_2 anode and the improvement of cycling performance [51]. Recent studies further demonstrate that MoS_2 is a competitive anode material based on the conversion reaction mechanism. The sodiation process of MoS_2 was depicted as an initial insertion process followed by a conversion reaction, leading to the formation of metallic Mo and Na_2S. Inspired by the application of MoS_2/graphene nanomaterial for Li-ion batteries, many efforts have been devoted to sythesizing MoS_2/graphene nanomaterial with novel nanostructure for Na-ion battery anode in consideration of the similar layered structure and better electrical conductivity of graphene. Recently, MoS_2/graphene paper has been proven to undergo a conversion reaction mechanism with Na ions during sodiation and delivers much higher reversible capacity (230 mAh/g) [51]. Three-dimensional MoS_2/graphene microspheres with multiple nanospheres was developed by Lee *et al.* [52]. The novel electrode displays extremely

stable cycling performance (600 cycles) for Na-ion batteries due to the synergistic effect of few-layer MoS_2 nanomaterial and three-dimensional porous graphene composition.

It is acknowledged that the layer-to-layer packed structure is desired for battery application since the interlayer spacing enables better accommodation upon large volume expansion. Another layered metal sulfide SnS_2 has a CdI_2-type structure with each layer stacking via van der Waals interactions. The large interlayer distance (0.59 nm) of SnS_2 facilitates the intercalation/de-intercalation of alkali metal ions (Li^+, Na^+) and is considered as a promising anode material for lithium and sodium storage. Recent knowledge and strategies focus on improving the cycling performance with nanostructure design and conductive graphene/carbon coating. Xie $et\ al.$ reported that the SnS_2@graphene composite can provide a reversible capacity of 725 mAh/g for 60 cycles at a current rate of 20 mA/g, which is the highest experimentally observed capacity of SnS_2 for Na-ion batteries [53]. Table 1.4 summarizes the theoretical and experimentally observed cycling performance of hard carbon, Na-alloys, metal oxides and metal sulfides [54]. Metal sulfides such as Ni_3S_2 can reversibly react with four sodium ions with a capacity of 400 mAh/g for Na-ion batteries [55]. FeS_2 was suggested as an anode with a high theoretical capacity. However, rapid capacity fading occurs from an initial capacity of 447 mAh/g to 70 mAh/g within 50 cycles [56]. Therefore, the cycling performance of these sulfides is not competitive as compared with MoS_2, which has large layer spacing in the crystalline structure. Thus, the characteristic two-dimensional structure and potential in battery applications of MoS_2 are crucial to the development of advanced anode materials for SIBs.

Table 1.4 The theoretical and largest experimental capacities of recent anode materials for Na-ion batteries [54]

Compound	Theoretical Specific Capacity (mAh/g)	Experimental Specific Capacity (mAh/g)	Voltage range (V)
Hard carbon	-	350	0-1.0
Sn	850	850	0.2-1.0
Sb	660	580	0.04-1.5
SnO_2/graphene	1378	600	0-3.0
Fe_3O_4	926	350	0.04-3.0
MoS_2/graphene	671	573	0-3.0
SnS_2/graphene	1135	725	0-3.0
Ni_3S_2	445	400	0.4-2.6
FeS_2	900	447	0-2.6

1.6 The synthesis and energy storage applications of MoS$_2$

As indicated by Fig. 1.5, MoS_2 has a lamellar structure with each layer stacking via van der Waals interactions. In a single-layered MoS_2, there are numerous S-Mo-S units where molybdenum atoms are sandwiched in the center by sulfur atoms.
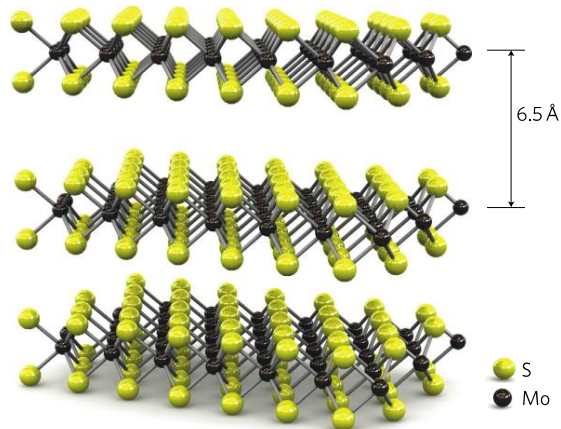
Figure 1.5 Three-dimensional schematic structure of MoS_2 [57].

Due to the similar layered structure to graphite, MoS_2 can also be exfoliated to single or a few layers by chemical or physical methods. The chemical synthetic routes include using molybdic acid and tungstic acid, which are treated with an excess of thiourea in an N_2 atmosphere at high temperature [58]. Another synthesis route involves the reaction between MoO_3 and KSCN under hydrothermal conditions [59]. Due to the weak van der Waals interactions between the MoS_2 layers and the similar structure to graphite, recent strategies for graphene production could be applied to the production of crystalline MoS_2. The introduction of mechanical/physical exfoliation, such as long-time ultrasound sonication and using adhesive tape to create two-dimensional crystals with few layers, open doors for a multitude of applications. A facile liquid phase exfoliation method was reported recently, in which single-layer MoS_2 sheets can be obtained in 1-methyl-2-pyrrolidinone (NMP) assisted with sodium hydroxide (NaOH) [60]. A chemical vapor deposition (CVD) method was developed to fabricate thin film MoS_2 for electronic device applications. In these approaches, various solid precursors such as MoO_3, Mo metal or ammonia tetrathiomolybdate $(NH_4)_2MoS_4$ were used and heated to high temperatures in the presence of sulphur powder/gas and co-deposited onto a substrate [61]. For energy storage

applications, a facile hydrothermal method was developed to prepare MoS_2 nanosheets, in which sodium molybdate (Na_2MoO_4) and thiourea (NH_2CSNH_2) were dissolved in water and heated to high temperature for a long time (24 hours) [62]. To prepare carbon coated MoS_2 nanoparticles, glucose can be simply introduced in the above method. The as-prepared MoS_2 nanoparticles from such hydrothermal methods have single or fewer layers since the typical peak for (002) stacking is not present in the XRD profiles, and indicates the stacking of MoS_2 layers is not the case. Further annealing at high temperature can lead to MoS_2 nanoparticles with better crystallization structure. The investigation of unique MoS_2 two-dimensional structures and the development of facile synthetic routes in large quantities are crucial to advance scalable applications of MoS_2 in different fields.

Molybdenum disulfide (MoS_2) is multifunctional and exhibits a remarkably diverse range of unique properties. It is well recognized as a super lubricant, owing to the weak van der Waals bonds between S–Mo–S layers. MoS_2 also contributes to the research of chemical sensing due to the variance in reactivity between basal and edge sites in functionalized MoS_2 nanosheets. Many research efforts have been devoted to using MoS_2 for photovoltaic applications due to the tunable direct band gap and highly deformable nature of a monolayer of MoS_2 [63]. In addition, the exploration of MoS_2 as a catalyst for hydrogen evolution attracts much attention recently. Finally, an increasing research activity has flourished about employing MoS_2 nanocomposites as high-capacity and stable anode materials for lithium and sodium storage systems. Many nano technological methods are being developed to fabricate MoS_2 nanocomposites in the field of energy storage [51,52,62,63].

It is acknowledged that the layered structure results in an improved intercalation and de-intercalation dynamics of alkaline ions because of the gallery space within layers. Previous studies demonstrate that the lithiation mechanism of MoS_2 is a two-step process:

$$MoS_2 + xLi^+ + xe^- \rightarrow Li_xMoS_2 \tag{1.6}$$

$$Li_xMoS_2 + (4-x)Li^+ + (4-x)e^- \rightarrow 2Li_2S + Mo \tag{1.7}$$
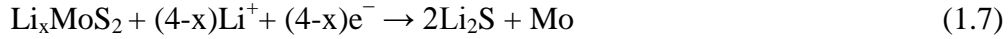
The intercalation of lithium ions into MoS_2 layers occurs with the formation of Li_xMoS_2. In the subsequent step, a conversion reaction takes place where Mo^{4+} in Li_xMoS_2 is reduced to Mo metal with the formation of Li_2S. During lithiation, its characteristic two-dimensional structure acts as a host lattice to provide reaction sites for lithium intercalation and de-intercalation without significant irreversible structural change of the host lattice. Thus, lithium-ions can diffuse between MoS_2 layers without causing a significant volume change and lead to high cycling reversibility in Li-ion batteries. Recently, conductive additives such as carbon nanotubes, conductive polymers and graphene have been incorporated to exfoliated MoS_2 since it is a poor electron conductor. The concordant fast transport of electrons and ions within the electrode is essential to realize great reaction kinetics. A facile synthesis of hierarchical MoS_2/Polyaniline (PANI) nanowires demonstrates high specific capacity (1062.7 mAh/g) and long cycle life (50 cycles) in Li-ion batteries [64]. The hierarchical textures offer large contact area and tensile PANI chains mitigate large lithiation-induced strain during cycling. After the first attempt by Park *et al.*,[51] the research interests of using MoS_2 as a Na-ion battery anode have been elevated. Extensive research has been done with two strategies: the fabrication of MoS_2 nanomaterial and the incorporation of a conductive carbon matrix. Lee and Kang *et al.* reported three-dimensional MoS_2/graphene microspheres with multiple nanospheres that display extremely stable cycling

performance (600 cycles) for Na-ion batteries [52]. G. Wang *et al.* reported the synthesis of MoS$_2$/reduced graphene oxide (RGO) nanocomposites with a facile one-pot hydrothermal method [53]. The newly formed anode material delivers excellent sodium storage capability and the synergistic effect between MoS$_2$ and graphene was elucidated with computational calculations. The superior cycling performance of MoS$_2$ nanocomposites as lithium ion and sodium ion battery anodes make them promising candidates to replace traditional anode materials and the in-depth mechanism investigation paves the way for the feasibility of high-performance Na-ion batteries.

1.7 Motivation and objectives of this research

Rechargeable lithium ion and sodium ion batteries have promoted considerable revolution to state-of-the-art energy storage technologies. To advance such technologies, it is of great significance to search for alternative anode materials with high specific capacity and energy density to substitute for conventional graphite and carbonaceous anode materials.

Firstly, molybdenum disulfide (MoS$_2$) and tin sulfides (SnS, SnS$_2$) are proposed as promising anode materials in LIBs and SIBs due to their high specific capacity, low cost and large availability. During lithiation, the insertion reaction between graphite and lithium ions results in a low capacity. In contrast, tin sulfides can form lithium-rich alloys, which offer high theoretical capacities in the range of 1136-1230 mAh/g [65]. The conversion reaction mechanism of MoS$_2$ with alkaline ions (Li$^+$, Na$^+$) and unique graphene-like structure enable superior cycling performance with high capacity and long cycle life in LIBs and SIBs.

22

Secondly, metal sulfides with two-dimensional structure are selected in this study. The layered structure of MoS_2 and SnS_2 has attracted a lot of attention because of its unique two-dimensional structure. The layer-to-layer stacked structure is desirable since it facilitates reversible alkaline ion insertion/extraction without causing large volume expansion. The interlayer distance between MoS_2 layers is 6.2 Å, and the value of SnS_2 crystalline structure is 5.9 Å. Therefore, it is expected to develop high performance Li-ion & Na-ion battery anodes with MoS_2 and SnS_2 nanomaterials.

Thirdly, the electrochemical behavior of anode materials during lithiation/sodiation is still far from clear, and fundamental studies are necessary to advance battery technologies. It is well recognized that the discharge mechanism of anode materials involves the intercalation chemistry, alloying and conversion reactions. This study focuses on tin sulfides and MoS_2 because their electrochemical behavior covers the insertion chemistry, alloying and conversion reactions. A comprehensive investigation of these metal sulfides will provide in-depth understanding for the electrochemical behavior of other anode candidates. Such fundamental research will pave the way for future research on rechargeable batteries.

The goals of this research are as follows: (1) search for advanced anode materials with high capacity and stable cycling performance in LIBs and SIBs; (2) reveal the discharge mechanism of MoS_2 and tin sulfides (SnS, SnS_2) during lithiation/sodiation; (3) develop new synthetic routes of MoS_2 and tin sulfides nanoparticles in large quantities; (4) minimize the volumetric expansion of MoS_2 and tin sulfides due to the conversion and alloying reactions with alkaline ions to maintain the structural integrity during cycling; (5) improve the reaction kinetics of MoS_2 and tin sulfides with the introduction of conductive carbonaceous materials.

1.8 Overview

To fulfill the research objectives, the rest of the dissertation is organized as follows.

In Chapter 2, a facile one-pot synthesis of tin sulfide/carbon (SnS/C) nanospheres is presented, which enables feasible large-scale production of SnS nanoparticles. The electrochemical performance of SnS/C nanospheres is evaluated in LIBs and compared under different voltage ranges. It is found that SnS/C nanospheres show less stable cycling performance in a narrower working potential (0.01-1.5 V). The reasoning of superior electrochemical performance and capacity degradation in a narrower potential is discussed with observations from electron microscopy.

Chapter 3 describes a simple solid-state reaction method utilized to synthesize carbon coated SnS_2 (SnS_2/C) anode materials by annealing metallic Sn, sulfur powder and polyacrynitrile (PAN) in a sealed vacuum glass tube. As compared with the conventional hydrothermal method, which is time-consuming and requires further purification, the new method is more feasible for large scale production of SnS_2 nanomaterial. The purpose of this preliminary research is to demonstrate the feasibility of employing SnS_2 as an advanced anode material in SIBs and to discuss the reaction kinetics of the SnS_2/C electrode after cycling.

In Chapter 4, the fabrication of molybdenum disulfide/carbon (MoS_2/C) nanospheres is presented along with their use as Na-ion battery anodes. The advantages of employing MoS_2/C nanospheres are discussed in detail and the electrochemical performance is compared with MoS_2 nanosheets without carbon coating. Many characterization tools such as *ex-situ* XRD (X-ray diffraction), EIS (electrical impedance spectroscopy), and FTIR (fourier transform infrared spectroscopy) have been utilized to understand the electrochemical behavior of MoS_2. A

comprehensive discussion of the reversibility of the conversion reaction between MoS_2 and sodium ions is provided. Therefore, the investigation on the electrochemical performance and sodiation/desodiation mechanism of MoS_2/C nanospheres provides insights for the feasibility of high-performance Na-ion batteries.

Chapter 5 gives the development of the synthesis of MoS_2/C nanomaterial is achieved via a one-step spray pyrolysis in which sucrose is introduced as a carbonaceous material. The electrochemical properties of MoS_2/C nanomaterial for Na-ion battery applications are discussed. The MoS_2/C composite synthesized with spray pyrolysis is robust to withstand the volume change during charge/discharge cycles and the reaction kinetics have been investigated by electrochemical impedance spectroscopy (EIS) analysis and rate capability testing. To better understand the superior cycling performance of MoS_2/C nanomaterial, the ability to preserve its morphology after cycling is demonstrated in details from *ex-situ* scanning electron microscopy (SEM) and transmission electron microscopy (TEM) images.

In Chapter 6, the work related with tin sulfides (SnS, SnS_2) and molybdenum disulfide for battery applications is summarized. Future work proposed includes the synthesis of unique one-dimensional SnS_2/C nanofibers with the electrospinning technique and their application for Na-ion battery anodes. Another direction would be the *in-situ* TEM investigation to observe and understand the volume change of metal sulfides during cycling.

Chapter 2

One-pot synthesis of SnS/C nanospheres for high-capacity lithium ion battery anode with long cycle life

2.1 Introduction

Rechargeable lithium ion batteries have versatile applications such as portable electronics, power tools and have a potential for widespread implementation on plug-in hybrid electric vehicles.[1,2] To advance such technologies, it is of great importance to develop high capacity electrode materials with stable lithium storage capability[66,67]. In recent years, many efforts have been devoted to searching for alternative anode materials with higher capacities than graphite (372 mAh/g) [68-70]. Tin-based materials received intensive attention owing to high theoretical capacity, inexpensive cost, and less toxicity as compared with other anode candidates (Sb, Pb) [71,72]. Recent studies focus on tin sulfides (SnS, SnS_2), in consideration of the formation of an amorphous Li_2S buffer matrix originating from the conversion reaction ($SnS + 2Li^+ + 2e^- \rightarrow Sn + Li_2S$) [73,74]. However, there are internal stresses stemming from the alloying process ($Sn + 4.4Li^+ + 4.4e^- \rightarrow Li_{4.4}Sn$). The large amount of lithium intercalation induces anisotropic volume expansion, which triggers particle pulverization and insufficient contact with the current collector and results in rapid battery degradation [75,76]. Therefore, the existence of large volume change has been considered as a critical issue that hinders the practical application of tin sulfides in lithium storage.

2.1.1 SnS nanomaterials as Li-ion battery anodes

Extensive research has been done to mitigate these problems with two strategies: the fabrication of MoS_2 nanomaterial and the incorporation of a conductive carbon matrix. Recently, conductive additives such as carbon nanotubes, conductive polymers and graphene have been incorporated into SnS, since it is a poor electron conductor [77-80]. The concordant fast transport of electrons and ions within the electrode is essential to realize great reaction kinetics. Recently, a facile synthesis of SnS nanobelts with a length/thickness ratio of 100 was first developed in recognition that the flexible nanobelts could withstand large volume change [81]. The specific capacity can be maintained at 500 mAh/g for 50 cycles, but the capacity fading still exists. The fabrication of one-dimensional SnS material attracts much research interest since one-dimensional structures such as nanowires, nanorods, and nanobelts can offer larger surface-to-volume ratio as compared to higher dimensional structures [82,83]. These one-dimensional nanostructures enable uniform arrangement of active material and there is substantial space between individual nanofibers or nanowires to allow the volume expansion or contraction based on lithium insertion/deinsertion process [84]. Recently, one-dimensional SnS nanorods with carbon coating were synthesized and deliver stable cycling performance in Li-ion batteries. The electrochemical performance of metallic Sn, SnO_2 and SnS was compared as reported by Im *et al*., in which SnS showed the highest reversible capacity (880 mAh/g) after 70 cycles [82]. In their study, SnS nanoparticles were synthesized from photolysis of a 1:1 TMT (tetramethyl tin)/H_2S mixture. However, the photolysis synthesis is not favorable for large-scale application because of the time-consuming fabrication, rigorous reaction condition, undesirable chemical usage and uncontrollable nanomaterial morphology.

2.1.2 Scope and objectives of this study

In this study, SnS/C nanospheres are fabricated with a facile all-solid-phase synthetic route in which metallic Sn, sulfur powder and polyacrynitrile (PAN) is annealed under vacuum. Firstly, this synthesis route enables easier mass production of SnS/C nanomaterials. Secondly, the annealed SnS/C nanomaterials can be directly used without further purification. The SnS/C nanospheres show superior lithium storage capability with high reversible capacity (~900 mA/g) after 200 deep galvanostatic cycles. Extensive results from *ex-situ* XRD and cyclic voltammograms (CV) indicate that the reversible formation of Sn and Li-rich alloys when cycled between 0.01-1.5 V. It is found that the further lithiation at higher potential (3 V) has a significant contribution to the cycling performance of SnS, in which the nanosphere morphology is maintained without obvious particle pulverization and aggregation, leading to high capacity retention after hundreds of charge/discharge cycles, as demonstrated by *ex-situ* SEM and XRD studies.

2.2 Experimental

Synthesis: All chemicals were purchased from Sigma Aldrich and used as received. Tin, sulfur powder and polyacrynitrile (PAN) polymer were mixed in a weight ratio of 2:1:3 respectively, in which PAN is added as a carbon source. The reactants were sealed in a glass tube under vacuum. The desired product SnS/C was collected after the sealed glass tube was annealed in an oven at 600 °C for 3 hours.

Characterization: SEM images were taken using a Hitachi SU-70 analytical ultra-high resolution SEM (Japan); TEM images were taken with a JEOL (Japan) 2100F field emission

28

TEM; TGA was carried out using a thermogravimetric analyzer (TA Instruments, USA) with a heating rate of 5 °C min^{-1} in argon; the XRD pattern was recorded with a Bruker Smart1000 (Bruker AXS Inc., USA) using CuKα radiation; Raman measurements were performed on a Horiba Jobin Yvon Labram Aramis using a 532 nm diode-pumped solid-state laser, attenuated to give ~900 µW power at the sample surface.

Coin-cell performance tests: The *SnS/C* powder was mixed with carbon black and sodium alginate binder to form a slurry at the weight ratio of active material/carbon black/sodium alginate as 80:10:10. The electrode was prepared by casting the slurry onto copper foil and drying in a vacuum oven at 100 °C overnight. Coin cells for lithium batteries were assembled with lithium foil as the counter electrode, 1 M LiPF$_6$ in a mixture of ethylene carbonate/diethyl carbonate (EC/DEC, 1:1 by volume) as the electrolyte, and Celgard®3501 (Celgard, LLC Corp., USA) as the separator. Electrochemical performance was tested using an Arbin battery test station (BT2000, Arbin Instruments, USA). All the cyclic voltammograms measurements were carried out using a Gamry Reference 3000 Potentiostat/Galvanostat/ZRA with a scan rate of 0.1 mV/s.

2.3 Results and Discussion

2.3.1 Structural and composition characterization of SnS/C nanospheres

SnS/C nanospheres are prepared from a facile all-solid-state synthetic method, in which metallic Sn, sulfur powder and polyacrynitrile (PAN) are annealed in a sealed glass tube under vacuum. This synthesis route is easier to scale up and the product after heat treatment can be used directly without any purification as compared with the hydrothermal route [83]. This method

29

is more economical in the atomic scale since each reagent contributes to the final product. In this work, tin monosulfide (SnS) is formed due to the addition reaction between metallic Sn and sulfur, while the *in-situ* carbonization of PAN occurs simultaneously to enhance the electrical conductivity and act as an accommodating matrix. Figure 2.1a shows the crystallization structure of SnS characterized by X-ray diffraction (XRD). The conspicuous broadening in the range of 15-30 degrees is ascribed to the existence of amorphous carbon. The peaks are in good agreement with a hexagonal structure of SnS (JCPDS No.33-1375) [84] and the main peaks can be indexed with characteristic crystal planes. The crystal structure and vibration properties of the SnS/C composite are further elucidated by Raman spectroscopy shown in Fig. 2.1b. The Raman spectra of SnS/C composite exhibits two distinct peaks at 190 cm^{-1} and 225 cm^{-1}, which are typical Raman active modes A_g owing to in-plane vibrational modes of hexagonal layered structured SnS [85]. There are two broad bands at 1364 cm^{-1} (D-band) and 1600 cm^{-1} (G-band) respectively, revealing the presence of in-plane vibration of sp^2-bonded carbon atoms and vibrational modes from sp^3-bonded carbon atoms in amorphous carbon [86].
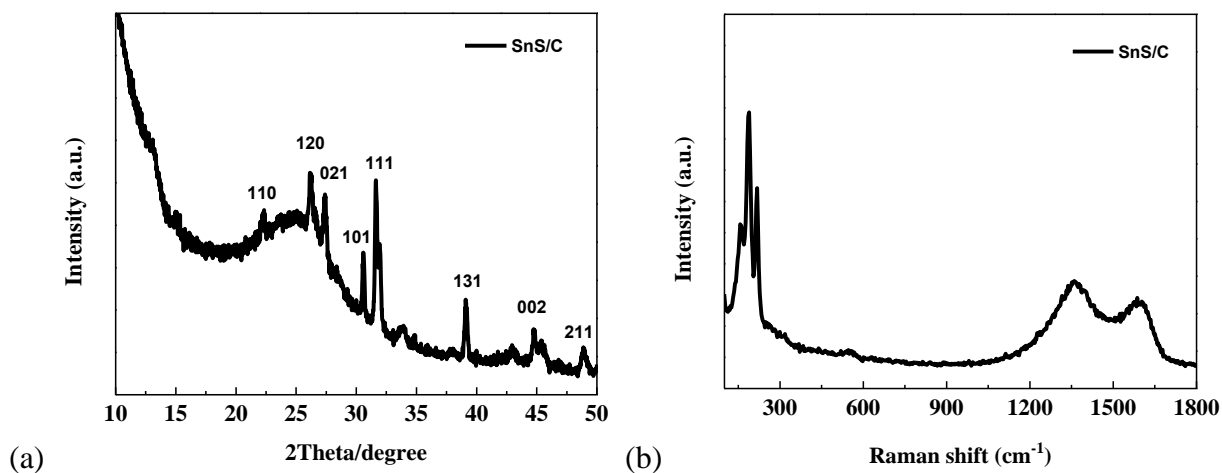

Figure 2.1 (a) XRD characterization and (b) Raman spectra of SnS/C nanospheres.

The weight ratio of SnS is approximately 38% as demonstrated by the TGA result as shown in Fig. 2.2 and calculated based on Eq. 2.1.

$$\text{SnS (wt\%)} = 100\% \times \frac{\text{molecular weight of SnS}}{\text{molecular weight of SnO2}} \times \frac{\text{final weight of SnO2}}{\text{initial weight of SnS/C composite}} \qquad (2.1)$$
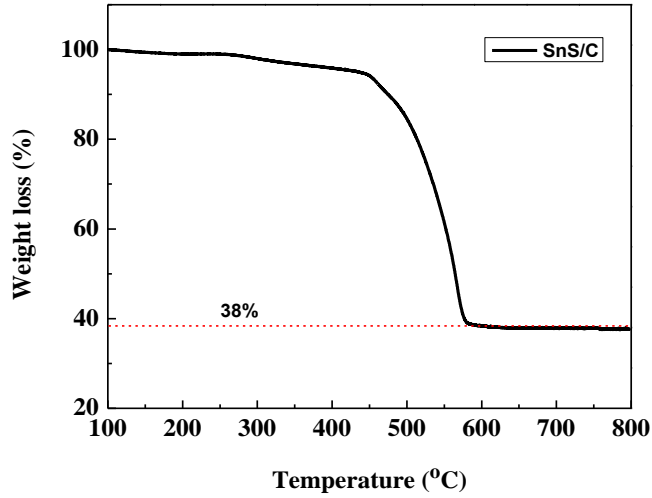

Figure 2.2.TGA result of SnS/C composite from 25 ^{o}C to 800 ^{o}C at a rate of 5 ^{o}C /min in air.

The morphology of the as-prepared SnS/C composite is revealed by scanning electron microscopy (SEM), transmission electron microscopy (TEM) images, and energy dispersive X-ray spectroscopy (EDS) mapping. From Fig. 2.3(a) and 2.3(b), it is clear that SnS forms typical spherical nanoparticles with conformal carbon coating due to *in-situ* carbonization of PAN after annealing. The average diameter of the SnS/C composite is ~200 nm as demonstrated by TEM image (Fig. 2.3(b)). The existence of amorphous carbon, Sn and S is demonstrated by the elemental mapping image of SnS/C, as shown by Fig. 2.3(c)-(f). The EDS mapping confirms that SnS is uniformly distributed in an amorphous carbon matrix.
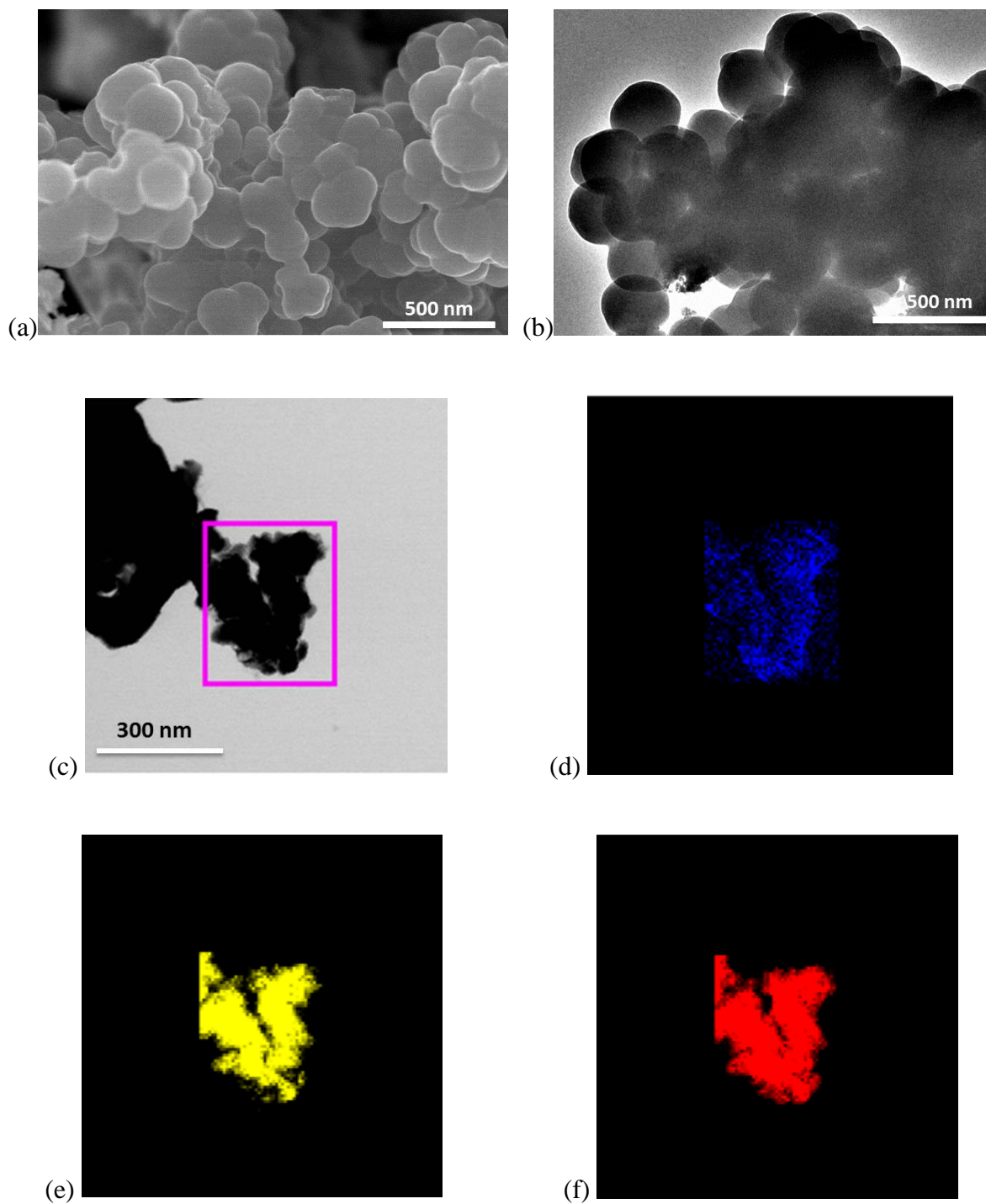
31

Figure 2.3 (a) SEM image and (b) TEM image of SnS/C composite; (c) EDS mapping image of SnS/C composite; (d) EDS mapping image of element C; (e) EDS mapping image of element S; (f) EDS mapping image of element Sn.

2.3.2 Electrochemical properties of SnS/C nanospheres

The electrochemical properties of the SnS/C composite are investigated in coin-cells with lithium metal as the counter electrode. The charge and discharge curves of the SnS/C electrode shown in Fig. 2.4(a) were measured between 0.01-3 V vs. Li^+/Li at a current density of C/5 (1 C = 1136 mA/g). During initial lithiation, there is an obvious plateau at 1.1 V, which is attributed to the conversion reaction between SnS and lithium ions ($SnS + 2Li^+ + 2e^- \rightarrow Sn + Li_2S$). A sloping curve is observed in the range of 0.3-0.75 V, which is indicative of the lithium alloying process. To further understand the electrochemical behavior of SnS/C nanospheres, cyclic voltammograms (CV) curves were measured for the initial five cycles with a cut-off potential window of 0.01-3 V as shown in Fig. 2.4(b). When discharged from 3 V to 0.01 V, three reductive peaks at 1.1, 0.6 and 0.01 V respectively are observed, and these are ascribed to the conversion reaction between SnS and Li^+ and the formation of Li-rich alloys. An obvious broadening shoulder is observed at 0.6 V owing to the formation of a solid electrolyte interface (SEI) film on the electrode surface during initial lithiation. There are two corresponding oxidation peaks/shoulder at 0.3 V and 0.6 V due to the de-alloying process. In the subsequent cycles, despite the reductive peak at 1.1 V shifting to higher potential of 1.3 V, the other reductive peaks and corresponding oxidative peaks are still present, demonstrating the highly reversible electrochemical reactions with lithium ions.
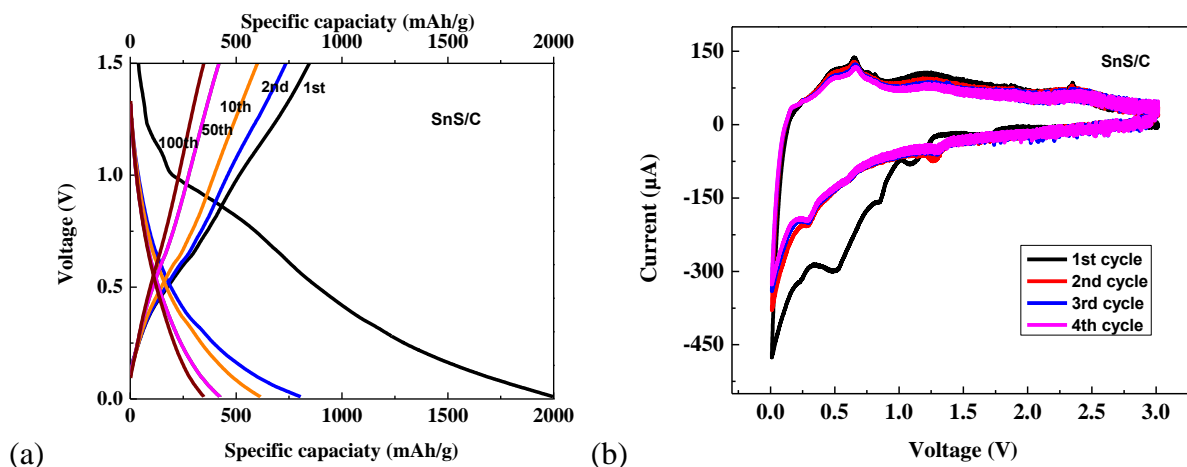
Figure 2.4 (a) Charge and discharge profiles of SnS/C electrode vs. Li^+/Li with a cut-off window of 0.01-3 V (b) Cyclic voltammograms of SnS/C electrode between 0.01-3 V of the first 5 cycles with a scan rate of 0.1 mV/s.

Figure 2.5 shows the cycling performance of the SnS/C electrode based on the total capacity (Fig. 2.5(a) and 2.5(b)) and specific capacity of SnS (Fig. 2.5(c) and 2.5(d)) in different recharge settings, the cycling performance of carbonized PAN (Fig. 2.5(e)) and rate capability of the SnS/C electrode (Fig. 2.5(f)) in lithium ion batteries. The specific capacity of the SnS/C electrode achieves ~1200 mAh/g in the initial cycle at a current density of 227 mA/g. All the specific capacities are calculated based on SnS after subtracting the contribution from carbon, which is about 350 mAh/g at the same current density as shown in Fig. 2.5(e). In subsequent cycles, the charge capacity (delithiation) of SnS/C electrode retains at 900 mAh/g for 200 deep galvanostatic cycling. The coulombic efficiency for the SnS/C electrode after the initial cycle is close to 100%, demonstrating efficient lithium ion insertion and extraction processes. However, the charge capacity declines to 350 mAh/g after 100 cycles when cycled in a lower potential window of 0.01-1.5 V (Fig. 2.5(d)).

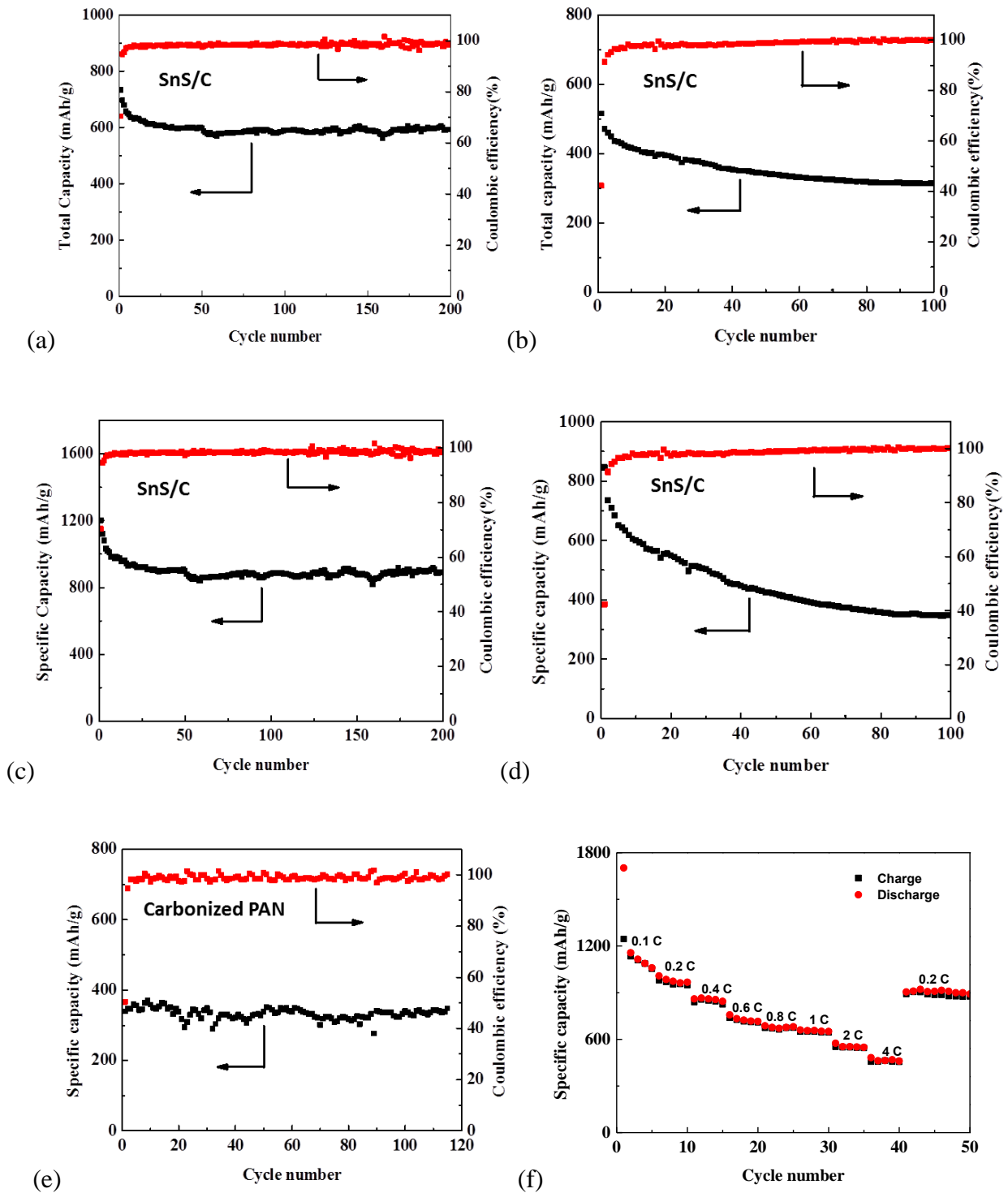Figure 2.5 Cycling performance of the SnS/C electrode based on the total capacity in the potential range (a) 0.01-3 V; (b) 0.01-1.5 V ; Cycling performance of the SnS/C electrode based on SnS in the potential range (c) 0.01-3 V; (d) 0.01-1.5 V; (e) Cycling performance of carbonized PAN at a current density of 0.2 C; (f) Rate performance of the SnS/C electrode at different current rates cycled between 0.01 and 3 V.

The rate performance of SnS/C electrode is investigated at various current rates from 0.1 C to 4 C cycled between 0.01-3 V. As shown in Fig. 2.5(f), except for the capacity fading in the initial five cycles due to the large volume change, it exhibits stable cycling performance with increased lithium ion intercalation/de-intercalation processes, which is an indication of its fast reaction kinetics with lithium ions. The specific capacity of the SnS/C electrode is 900 mAh/g at a current rate of 0.2 C. Even at a high current rate of 1 C, the charge capacity of SnS/C electrode is 722 mAh/g, and it recovers to its initial capacity (900 mAh/g) immediately after the current density decreases to 0.2 C. The fast reaction kinetics of the SnS/C electrode is associated with the *in-situ* carbonization of PAN, in which the electrical conductivity is greatly enhanced by the carbon coating.

2.3.3 Effect of cutoff voltage on lithium storage performance of SnS/C anode

It is acknowledged that a narrower potential window is more favorable to the cycling stability due to a shortened lithiation/delithiation process, smaller volume change and less mechanical stress in the electrode during long-term galvanostatic cycling. Much improved cycling performance of SnS/C electrode has been observed when cycled in an enlarged potential window in lithium-ion batteries. The cycled SnS/C cell between 0.01-1.5 V mainly undergoes the reversible alloying and de-alloying processes, as demonstrated by CV scans. The large volume change induced by the formation of lithium-rich alloys ($Li_{4.4}Sn$) causes structural pulverization, results in insufficient contact with the current collector, and leads to battery malfunction in extended cycling. To further elucidate the electrochemical mechanism, *ex-situ* studies in terms of SEM images and XRD diffraction patterns of the cycled SnS/C cells were carried out. Figure 2.6 shows the morphology changes of the SnS/C electrode for two recharge settings. As

36

evidenced by the SEM image, the fresh SnS/C electrode shows a regular spherical shape with an average diameter of ~200 nm, consistent with the as-prepared SnS/C composite. After cycling between 0.01-1.5 V, the agglomeration of the active material occurs due to irreversible volume change during lithiation. As a comparison, the SEM image of a cycled SnS/C cell with an enlarged potential window (0.01-3 V) demonstrates that SnS can maintain spherical shape in extended cycling.

Figure 2.7 shows the structural changes between a fresh SnS/C electrode, a discharged cell, a cycled cell in a lower potential range of 0.01-1.5 V and a cycled cell in an enlarged potential range of 0.01-3 V in XRD patterns. To understand the structural change at lithiation state, the cell was fully discharged to 0.01 V, then charged to 3 V (or 1.5 V) and maintained at 3 V (or 1.5 V) for 24 hours. Before XRD measurements, the electrode was immersed in dimethyl carbonate (DMC) to remove $LiPF_6$. The diffraction profiles of the fresh SnS/C electrode show characteristic peaks at 30 and 31 degrees, which are indexed to the (101) and (111) crystalline planes in the hexagonal structure of SnS. The crystalline Cu diffraction pattern, attributed to the copper current collector, was demonstrated by peaks at 43, 51 degrees. The existence of a peak at 27 degree is due to the addition of carbon black in the electrode. After lithiation (discharge), the SnS in the SnS/C electrode converts to Li_2S and Li_xSn. No crystal peaks can be observed in the discharged electrode and charged cell at 3 V, probably due to the formation of an amorphous structure. After one deep discharging/charging cycle to a fully delithiation state at 1.5 V, the existence of crystalline Sn was observed, as evidenced by the characteristic peak of metallic Sn at 31 degree and 33 degree [22].
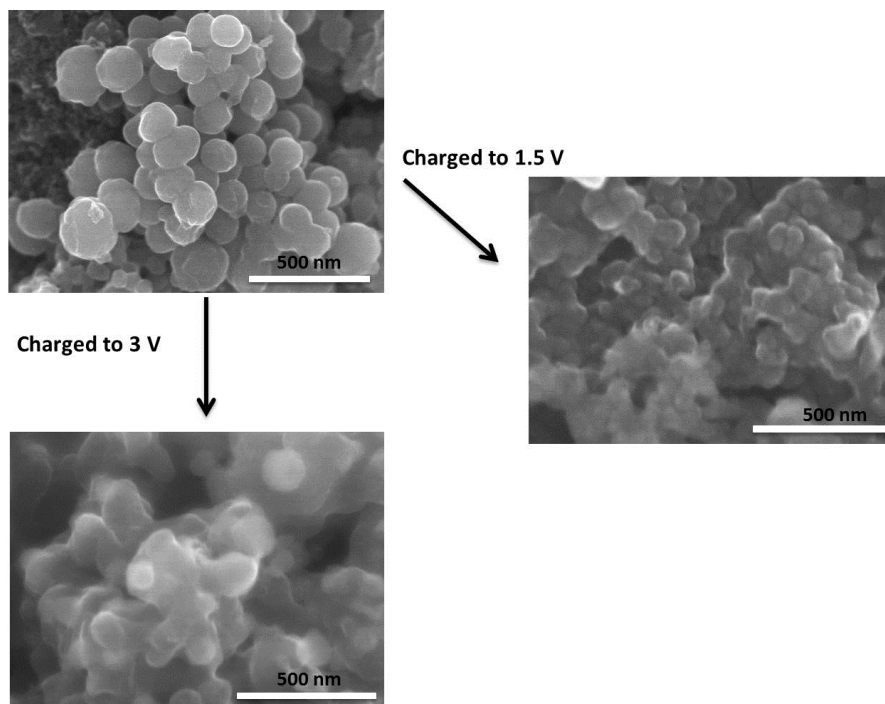
Figure 2.6 Structural changes of fresh SnS/C electrode when charging to 1.5 V and charging to 3 V after deep discharge/charge cycles as shown in SEM images.

The crystalline phase can be assigned to tetragonal Sn (JCPDS 89-4898). The *ex-situ* XRD studies provides strong evidence for the reversible formation of Sn and Li-rich alloys when charged to 1.5 V, which further explains the capacity fading of the SnS/C electrode in a narrower potential window. The formation of crystalline Sn is evidenced by the (101) lattice plane with an interlayer distance of 0.27 nm and (001) direction with an interlayer distance of 0.31 nm, which further confirms the existence of crystalline Sn. These findings are consistent with ex-situ XRD measurements, demonstrating the formation of crystalline Sn when cycled between 0.01-1.5 V.
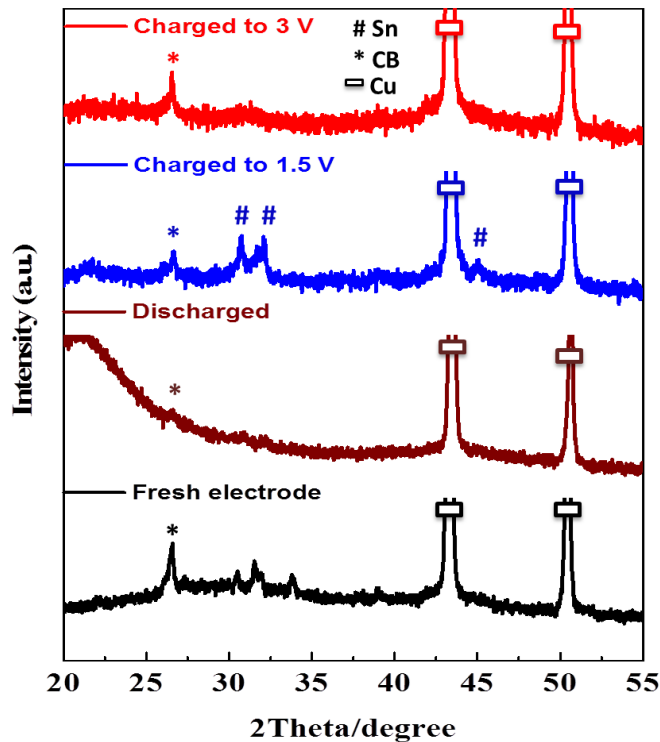
Figure 2.7 Structural changes of SnS/C electrodes before cycling, after discharge/charge cycles between 0.01-1.5 V and after discharge/charge cycles between 0.01-3 V (CB = carbon black).

2.4 Conclusion

The main challenge to advance high-power lithium-ion storage is accommodating the volumetric change caused by the large amount of lithium ion intercalation and maintaining the electrode integrity. The SnS/C composite was prepared with a facile one-pot synthetic route by annealing the mixture of metallic tin and sulfur powder with *in-situ* carbonization of PAN. The SnS/C electrode delivers an extremely high initial capacity (1200 mAh/g) and retains at 900 mAh/g after 200 cycles at a current density of 227 mA/g, which is the best cycling performance to date. CV scans of SnS/C electrode show conspicuous peaks for the conversion reaction and redox peaks for the reversible formation and decomposition of Li-rich alloys. From *ex-situ* SEM

images of the fresh electrode, cycled SnS/C electrode between 0.01-1.5 V, and cycled SnS/C electrode between 0.01-3 V, the cycled SnS/C electrode in an enlarged recharge setting shows regular spherical shape without structural cracks, demonstrating its ability to maintain structural integrity and contributing to its superior lithium-ion storage capability. The superior cycling performance of the SnS/C electrode and the findings from *ex-situ* SEM and XRD pave the way for the feasibility of high-performance Li-ion batteries.

Chapter 3

Solid-State Fabrication of SnS$_2$/C Nanospheres for High Performance Na-Ion Battery Anode

3.1 Introduction

As promising substitutions to lithium ion batteries (LIBs), sodium ion batteries (NIBs) have attracted much attention for renewable energy storage due to low cost, inexhaustible sodium resources and similar insertion chemistry with lithium ions [87-90]. The current Na-ion batteries face severe challenges from low energy density and poor cycling stability, since sodium intercalation induces anisotropic volume expansion, which triggers particle pulverization and insufficient contact with the current collector [91]. Previous studies on the exploration of low-cost cathode materials, including selenium, NaFePO$_4$, and transitional metal oxides and sodium sulfate [89, 92-94], have achieved great success in the fabrication of high performance cathode materials. The anode material studies focus on carbonaceous materials [95-98], metals (Sn, Sb) [99-101], and metal oxides [102,103], all of which suffer from either low capacity or poor cycle life. The exploration of advanced anode materials with high capacity and long cycle life has emerged as a primary bottleneck for the development of high performance Na-ion batteries.

To pursue a high performance anode material, the particle pulverization induced by sodium ion insertion/extraction has to be alleviated. The layered structure is favorable for ion intercalation/de-intercalation, and the interlayer spacing enables better accommodation upon large volume expansion. Among metal sulfides [104-106], SnS_2 has a CdI_2-type structure with each layer stacking via van der Waals interactions [107]. Its large interlayer distance (0.59 nm) facilitates the intercalation/de-intercalation of alkali metal ions (Li^+, Na^+) and it is considered as a promising anode material for lithium and sodium storage [108-113]. Inspired by the similar two dimensional structure of graphene, Xie *et al.* reported that SnS_2@graphene composite can provide a reversible capacity of 725 mAh/g for 60 cycles at a current rate of 20 mA/g [114]. Recently, Zhang *et al.* reported SnS_2 with reduced graphene oxide composite for a sodium ion battery anode, which can deliver a high charge capacity of 649 mAh g^{-1} at a current rate of 100 mA g^{-1} [115]. However, it still suffers from capacity loss after long-term cycling. Meanwhile, the preparation of SnS_2/graphene composite involves the complex hydrothermal synthesis of SnS_2 from $SnCl_4$ precursor, reduction of graphene oxide and complicated purification process from the mixture of tin (IV) chloride, and thioacetamide (TAA) [116]. Therefore, it is not feasible for large scale production of uniform nanomaterial.

This work describes the synthesis of carbon coated SnS_2 nanomaterial using a solid-state route in which metallic Sn, sulfur powder and polyacrynitrile (PAN) are annealed in a sealed vacuum glass tube. Firstly, this synthetic route enables mass production of SnS_2/C nanomaterials. Secondly, the annealed SnS_2/C nanomaterials can be directly used for electrode preparation without further purification. Thirdly, the large interlayer distance of SnS_2 synthesized using the solid state reaction can effectively accommodate the volume changes in the sodiation, and the carbon from carbonized PAN significantly improves the electrical conductivity of pure SnS_2.

42

Experimental observations demonstrate that SnS_2/C nanomaterials show superior sodium storage capability with high reversible capacity (~600 mA/g) after 100 deep galvanostatic cycles. Extensive results from *ex-situ* scanning electron microscopy (SEM) show that the nanosphere morphology is maintained without obvious particle pulverization and aggregation, leading to high capacity retention after hundreds of charge/discharge cycles.

3.2 Experimental

Synthesis: All chemicals were purchased from Sigma Aldrich and used as received. Tin, sulfur and polyacrylonitrile (PAN) were mixed with a ratio of 2:3:5 (Sn/S/PAN) by weight and sealed in a glass tube under vacuum. The sealed glass tube was annealed in an oven at 600 °C for 3 h. The SnS_2/Carbon composites were collected as a black powder.

Material Characterization: SEM images were taken using a Hitachi SU-70 analytical ultra-high resolution SEM (Japan); TEM images were taken using a JEOL (Japan) 2100F field emission TEM; TGA was carried out using a thermogravimetric analyzer (TA Instruments, USA) with a heating rate of 5 °C min^{-1} in argon; the XRD pattern was recorded with a Bruker Smart1000 (Bruker AXS Inc., USA) using CuKα radiation; Raman measurements were performed on a Horiba Jobin Yvon Labram Aramis using a 532-nm diode-pumped solid-state laser, attenuated to give ~900 µW power at the sample surface.

Electrochemical measurements: The as-prepared SnS_2/C powder was mixed with carbon black and sodium alginate binder to form a slurry of active material/carbon black/sodium alginate at the weight ratio of 80:10:10, respectively. Coin cells for sodium-ion batteries were assembled with sodium foil as the counter electrode, 1 M $NaPF_6$ in a mixture of fluoroethylene

carbonate/dimethyl carbonate (FEC/DMC, 1:1 by volume) as the electrolyte and Celgard 3501 as the separator. The electrochemical performance was tested using an Arbin battery test station (BT2000, Arbin Instruments, USA). Both the charge and discharge current density and specific capacity were calculated based on the mass of SnS_2 in the electrode. Cyclic voltammograms were recorded using a Solatron 1260/1287 Electrochemical Interface (Solatron Metrology, UK) with a scan rate of 0.1 mV/s between 0.005 and 2.5 V (versus Na/Na^+).

3.3 Results and Discussion

3.3.1 The synthesis and structural characterization of SnS_2/C composite

Figure 3.1 shows the synthesis of the SnS_2/C composite via a facile solid-state reaction in a sealed glass tube. The SnS_2 is formed on a carbon matrix, which is generated by the carbonization of the PAN. Since the melting point of metallic Sn (231.9 °C) is much lower than the boiling point (445 °C) of sulfur, gaseous sulfur at 600 °C can completely react with liquid Sn in the sealed tube to form SnS_2 and uniformly disperse on the carbon matrix formed from carbonization of the PAN. By this method, the composition of SnS_2/C nanomaterials can be precisely controlled and be produced in large quantities.

The crystalline structure of SnS_2 was characterized using the X-ray diffraction pattern (XRD), as shown in Fig. 3.2(a). All the peaks can be indexed to 2T-type layered structure of SnS_2 (PDF 00-023-0677), with a calculated lattice parameter of a = 3.162 ± 0.003 Å and c = 5.890 ±0.003 Å. The absence of impurity peaks indicates the formation of pure crystalline SnS_2. Since no graphite peaks are observed in the XRD, the carbon formed from carbonization of PAN exists as amorphous carbon. The graphitization degree of carbon in SnS_2/C was further characterized with

Raman spectra, as shown in Fig. 3.2(b). The typical Raman active A^1_g mode of SnS_2 is observed as a sharp peak at 313 cm^{-1}, owing to in-plane vibrational modes within a sulfur-tin-sulfur plane [117,118].
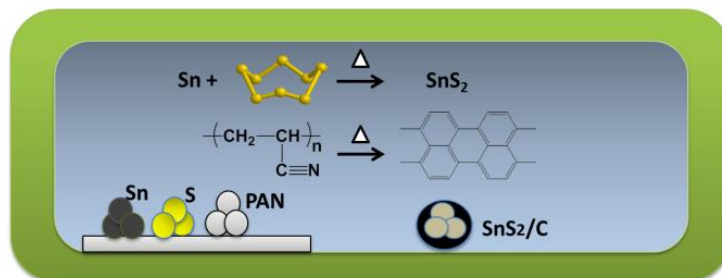

Figure 3.1 Schematic illustration of solid-state synthesis route of SnS_2/C nanomaterials.

(a)

(b)
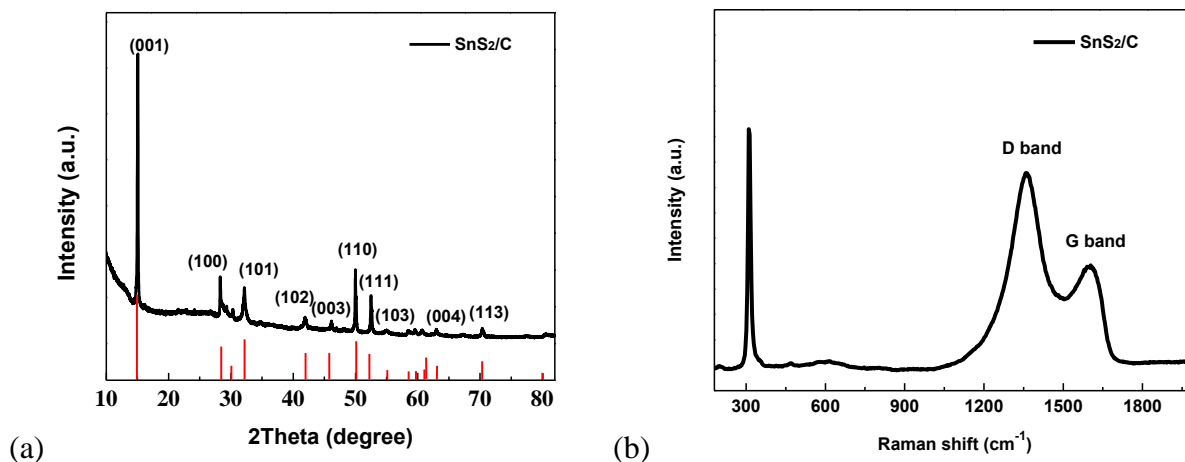
Figure 3.2 (a) X-ray diffraction pattern of the as-prepared SnS_2/C composite; (b) Raman spectra of SnS_2/C composite at room temperature using 532 nm wavelength excitation.

The Raman spectra exhibit two broad bands at 1350 cm^{-1} (D-band) and 1600 cm^{-1} (G-band), corresponding to typical in-plane vibration of sp^2-bonded carbon atoms and vibrational modes from sp^3-bonded carbon atoms in amorphous carbon, respectively [119]. The intensity ratio of the D/G band is 2/1, as demonstrated by Fig. 3.2(b). The high peak ratio of the D band to G band

demonstrates the low graphitization of carbon in SnS_2/C, which is consistent with the XRD result in Fig. 3.2(a).

3.3.2 Composition analysis and morphology of SnS_2/C composite

The SnS_2 content in the SnS_2/C composite was determined using thermogravimetric analysis (TGA), as shown in Fig. 3.3. The major weight loss in the range of 450-600 ^{o}C is attributed to the combustion of C to CO_2 gas and the oxidation of SnS_2 to SO_2 gas when the sample was oxidized in air from 25 ^{o}C to 800 ^{o}C [120]. Based on the weight loss and Eq. 3.1, the weight ratio of SnS_2 in the composite is calculated as 41%.
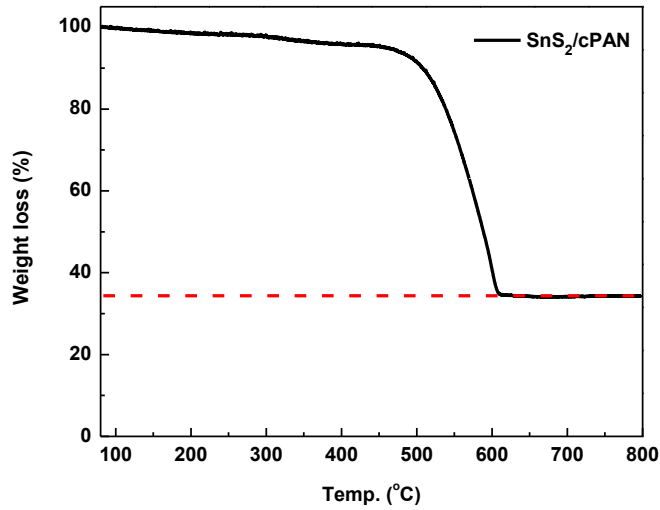
Figure 3.3 TGA results of SnS_2/Carbonized PAN (SnS_2/C) composite from 25 ^{o}C to 800 ^{o}C in air at a heating rate of 5 ^{o}C/min.

$$SnS_2\,(wt\%) = 100\% \times \frac{Mw \text{ of SnS2}}{Mw \text{ of SnO2}} \times \frac{\text{mass of SnO2}}{\text{mass of SnS2/C composite}} \qquad (3.1)$$

Mw: Molecular weight

The scanning electron microscopy (SEM) image is shown in Fig. 3.4(a). The as-prepared SnS$_2$/C nanomaterial forms regular nanosphere morphology with a diameter about 200 nm. This is because the carbonaceous material tends to form a regular sphere-like morphology in the solid-state reaction. The spheroidizing of PAN also limits the growth of the SnS$_2$ crystal in the c-axis direction during the synthesis, thus forming nanospheres [121]. The nanosphere morphology of the SnS$_2$/C composite is also seen in the transmission electron microscopy (TEM) image in Fig. 3.4(b) with a clear round shape. The distribution of amorphous carbon, Sn and S is further demonstrated by elemental mapping images of SnS$_2$/C, as shown by Fig. 3.5(a)-(d). The Energy-dispersive X-ray spectroscopy (EDS) confirms that SnS$_2$ is uniformly distributed in the amorphous carbon matrix.

(a) 500 nm   (b) 500 nm
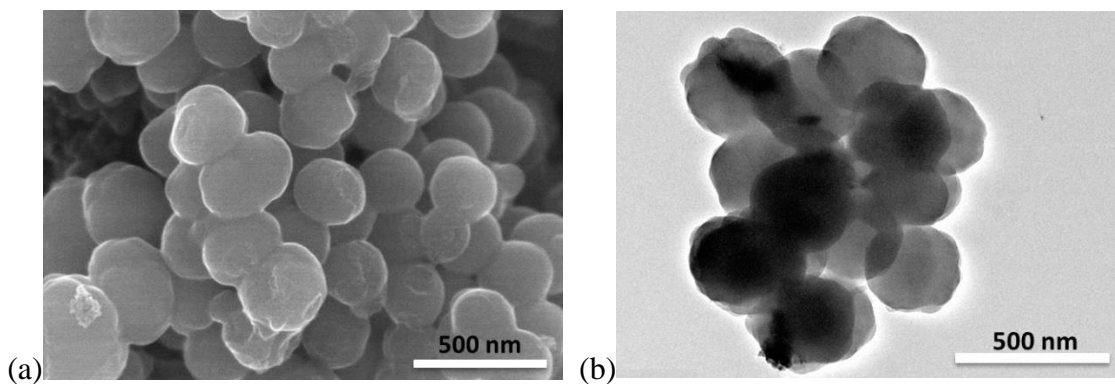
Figure 3.4 (a) SEM image of SnS$_2$/C composite; (b) TEM image of SnS$_2$/C composite.
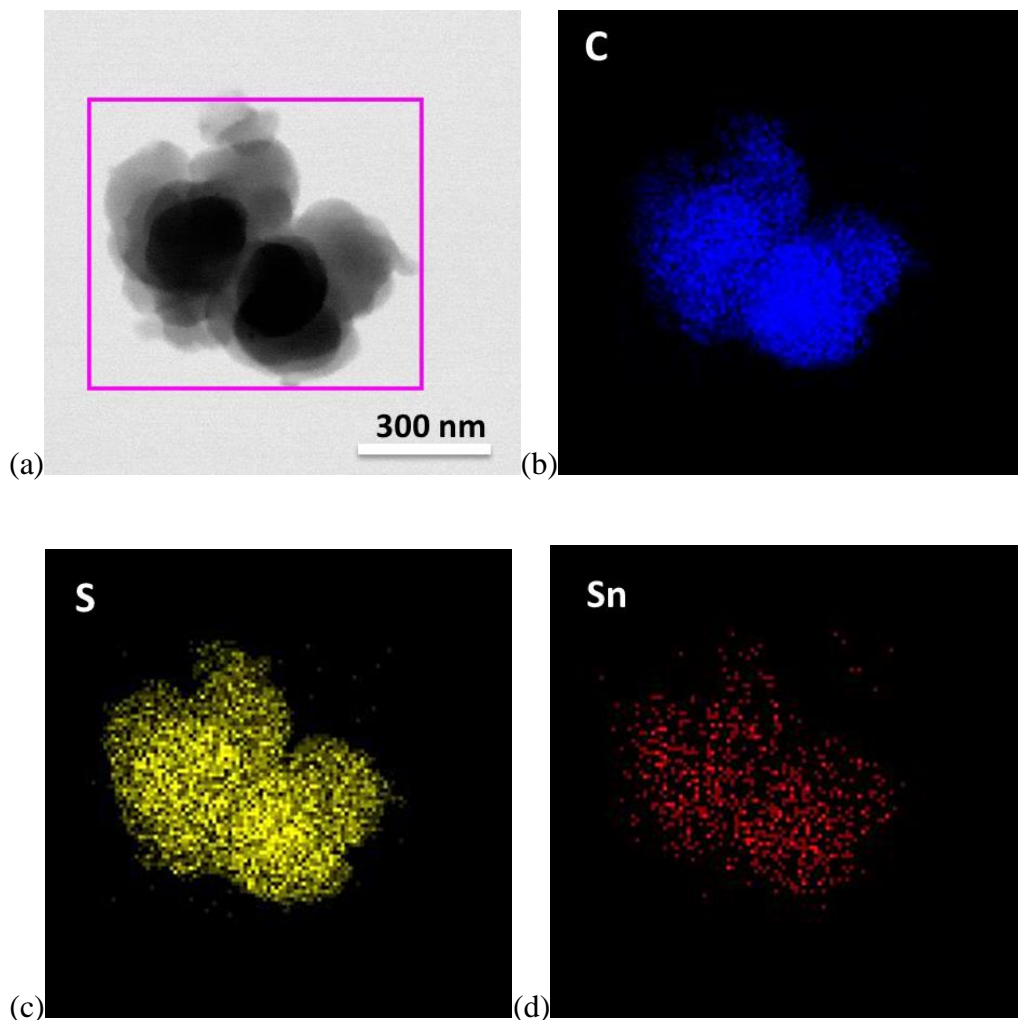
Figure 3.5 (a) EDS mapping image of SnS_2/C composite; (b) EDS mapping image of element C; (c) EDS mapping image of element S; (d) EDS mapping image of element Sn.

3.3.3 Cycling performance of SnS_2/C nanospheres for SIBs

The electrochemical properties of SnS_2/C nanospheres were investigated in coin-cells using sodium metal as the counter electrode. To understand the discharge mechanism, cyclic voltammogram (CV) curves of the SnS_2/C electrode were measured at a scanning rate of 0.1 mV/s during the initial three cycles. Figure 3.6(a) shows that the initial sodiation process exhibits three cathodic peaks at 1.3 V, 0.9 V, 0.25 V, respectively and a very small shoulder at 0.6 V. The

peak at 1.3 V is ascribed to the formation of Na_xSnS_2 in which sodium ions intercalate into SnS_2 layers [114,115]. The peak at 0.9 V is due to the conversion reaction between Na_xSnS_2 and sodium ions ($Na_xSnS_2 + (4-x)Na^+ + (4-x)e^- \rightarrow Sn + 2Na_2S$) and the small shoulder at 0.6 V is due to the formation of irreversible solid electrolyte interphase (SEI) in the 1st cycle [115]. The peak at 0.25 V corresponds to the alloying process between metallic Sn and sodium ions. ($Sn + yNa^+ + ye^- \rightarrow Na_ySn$, $0 < y < 3.75$) During the anodic scan to 2.5 V, there are three corresponding oxidation peaks/shoulder at 0.3 V, 1.1 V and 1.8 V, respectively due to the desodiation process. The oxidation peak at 0.3 V corresponds to the desodiation process of Na_xSn to form metallic Sn and the peak at 1.1 V is attributed to the formation of Na_xSnS_2. The peak at 1.8 V is very inconspicuous and may correspond to the de-insertion process of Na_xSnS_2. In the subsequent cycles, the reductive peak at 0.3 V shifts to higher potential at 0.45 V, which is attributed to an activation process.
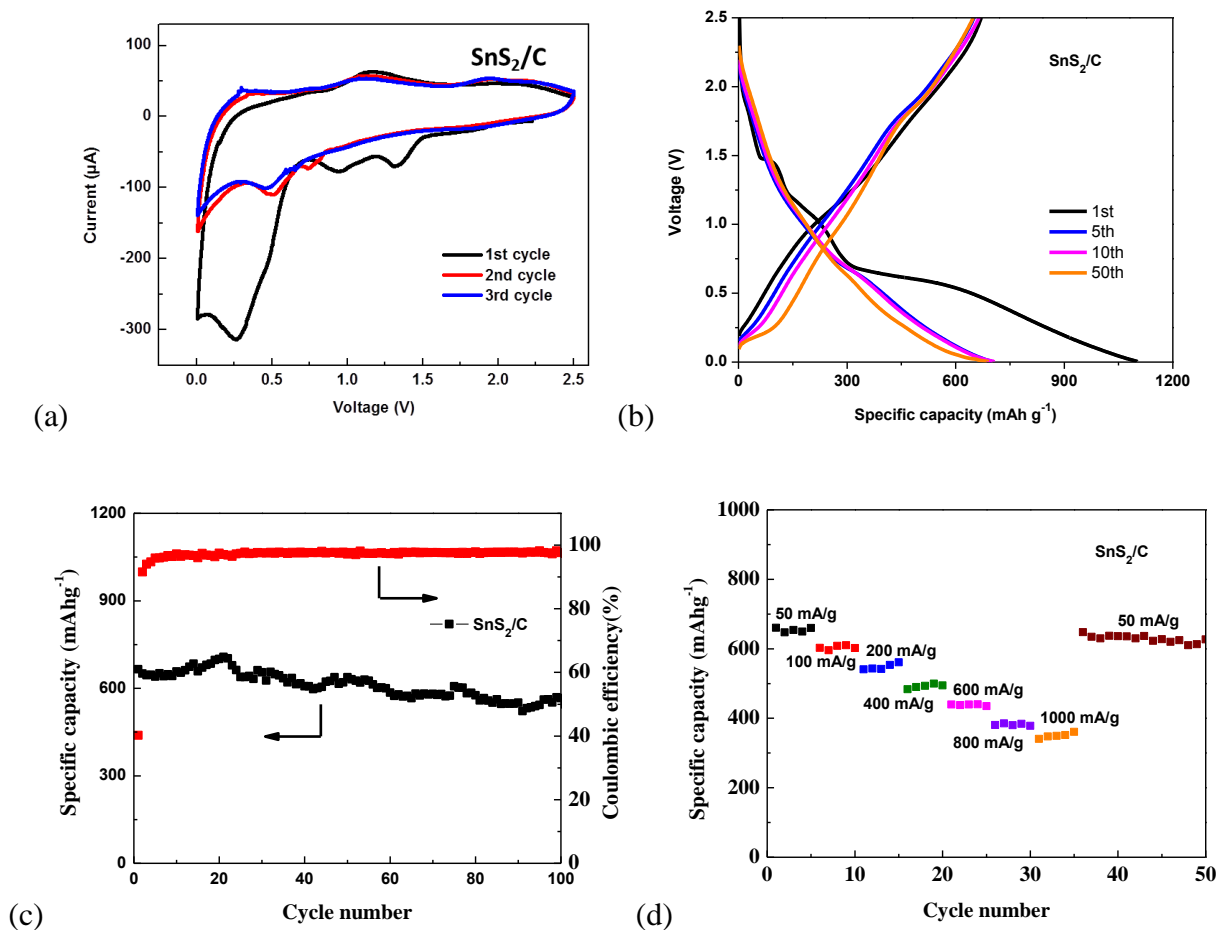
Figure 3.6 (a) Cyclic voltammetry curves of SnS_2/C electrode scanning from 5 mV to 2.5 V at a scanning rate of 0.1 mV/s; (b) Charge-discharge profiles of SnS_2/C electrode at a current density of 50 mA/g; (c) Cycling performance of SnS_2/C electrode at a current density of 50 mA/g; (d) rate capability of SnS_2/C electrode at various current densities in Na-ion batteries.

Figure 3.6(b) shows the galvanostatic charge and discharge behavior of the SnS_2/C electrode measured between 0.005-2.5 V at a current density of 50 mA/g. During initial sodiation, the plateau at higher voltage (1.4 V) is attributed to the intercalation of sodium ions into SnS_2 layers without composition change [114,122]. The slope plateau at 0.8-0.6 V corresponds to the conversion reaction between sodium ions and Na_xSnS_2, in which metallic Sn and Na_2S are formed, and the formation of solid electrolyte interphase (SEI) due to reduction of electrolytes. A sloping curve is

observed at a lower voltage, which is indicative of the alloying reaction between sodium ions and Sn ($Sn + yNa^+ + ye^- \rightarrow Na_ySn$, $0 < y < 3.75$). The SnS_2/C electrode delivers an extremely high capacity (1100 mAh/g) during the first sodiation, which is partially contributed by the irreversible formation of an SEI layer. In the subsequent cycles, the SnS_2/C electrode exhibits stable cycling performance and a high reversible capacity (600 mAh/g) is maintained after 50 cycles, as shown by the charge/discharge curves of the 2nd cycle, 10th cycle, 50th cycle. All the specific capacities are calculated based on SnS_2 after subtracting the contribution from carbon, which is about 100 mAh/g at the same current density.

The electrochemical performance upon galvanostatic cycling between 0.005 and 2.5 V at a current density of 50 mA/g is shown in Fig. 3.6(c). Though there is a large irreversible capacity loss (60%) in the first discharge (sodiation) and charge (desodiation) due to the formation of SEI layer, the SnS_2/C electrode displays a stable capacity of around 600 mAh/g for 100 cycles with capacity loss of only 0.14% per cycle. Meanwhile, the Coulombic efficiency quickly increases to ~100% after the first five cycles, demonstrating an efficient sodium ion intercalation/deintercalation process. The rate capability of the SnS_2/C electrode at high current rates is demonstrated in Fig. 3.6(d). The electrode delivers stable charge capacity of 660 mAh/g at 50 mA/g. As the current density increases to 1 A g^{-1}, the charge capacity still remains at 360 mAh/g. After the current density decreases back to 50 mA/g, the capacity of SnS_2/C electrode recovers to its initial capacity (660 mAh/g). The good rate capability of SnS_2/C electrode is an important indicator of its fast reaction kinetics in Na-ion batteries. The SnS_2/C nanospheres synthesized from solid-state reaction shows one of the best performances for Na-ion battery anodes to date [114-116].

3.3.4 Mechanism studies

The mechanism for the highly stable cycling behavior of the SnS$_2$/C electrode was investigated by analysis of the electrochemical impedance spectroscopy (EIS) at the 1st, 5th, 10th and 50th cycles and shown in Fig. 3.7 using the equivalent circuit shown as the inset. The fitted resistances are given in Table 3.1. The EIS of the SnS$_2$/C electrode is characterized by a depressed semi-circle in the high frequency region and a straight sloping line in the low frequency region. The resistance at the intersection of high frequency represents electrolyte resistance (R_1), the semi-circle corresponds to interface impedances (SEI impedance R_2, and charge transfer resistance R_3), and the low-frequency slope line is due to the Na-ion diffusion resistance in the SnS$_2$/C particles. As shown in Fig. 3.7 and Table 3.1, the interface resistance R_2+R_3 decreases in the first 5 cycles due to the activation process, and then become stable after the 5th cycle. The stable impedance between 10th cycle and 50th cycle demonstrates the robustness of the stable SEI layer and the robust structural integrity during charge/discharge cycles.
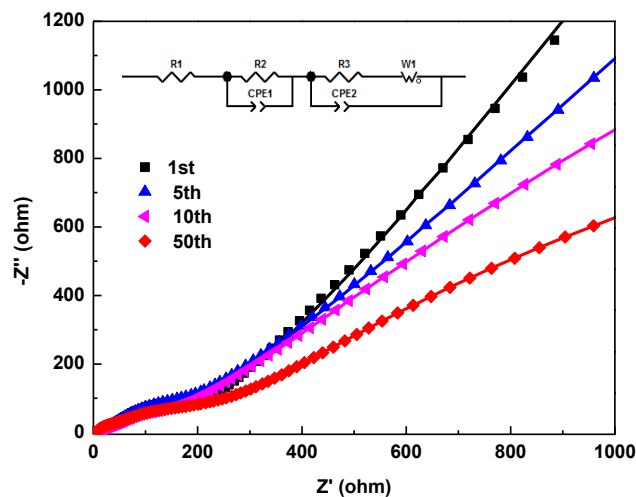
Figure 3.7 Experimental (dot) and simulated (line) electrochemical impedance spectra of SnS$_2$/C electrode after one cycle, five cycles, ten cycles and fifty cycles in Na-ion batteries.

Table 3.1 Resistances of the equivalent circuit obtained for different cycle number of the battery

Cycle number	R_1 (Ω)	R_2 (Ω)	R_3 (Ω)	CPE1 -T(Ω)	CPE1 -P(Ω)	CPE2 -T(Ω)	CPE2 -P(Ω)
1	15.22	270.7	N/A	7.685 2E-5	0.584 78	N/A	N/A
5	7.2	23.1	94.54	3.997 3E-6	0.827 83	2.005 1E-5	0.794 51
10	11.24	23.47	38.07	5.575 3E-6	0.801 73	1.530 6E-5	0.806 68
50	5.656	33.14	41.29	5.214 1E-6	0.787 15	1.658 5E-5	0.785 76

Figure 3.8 SEM image of SnS$_2$/C electrode after 50 charge/discharge cycles in Na-ion batteries.

The morphology of SnS_2/C electrode after 50 cycles was investigated by SEM. As shown in Fig. 3.8, the regular spherical 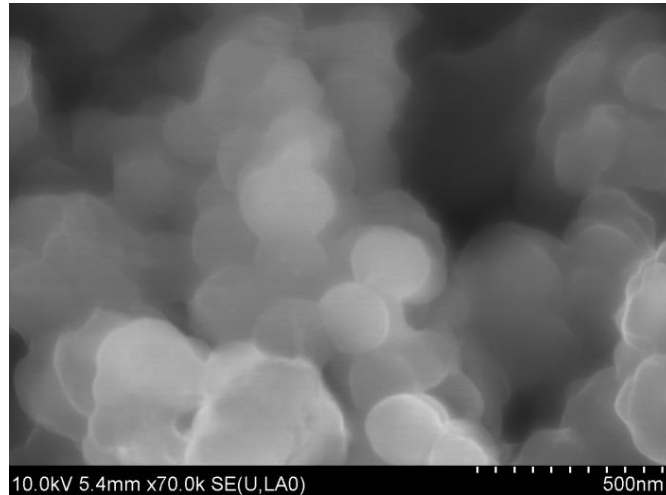particles can be clearly observed underneath the thin SEI layer formed during the first sodiation. The result was further confirmed by the TEM image of cycled SnS_2/C electrode, as shown in Fig. 3.9. It shows that SnS_2/C nanospheres maintain their morphology after 50 cycles, and the particle diameter remains about 200 nm. There are no observable structural cracks, particle pulverization or volume expansion induced by the large strain during repeated charge/discharge cycles. The SnS_2/C nanospheres are capable of maintaining the morphology after 50 cycles in Na-ion batteries since the regular spherical shape is clearly observed. The result demonstrates that the SnS_2/C electrode is able to maintain its structural and morphological integrity after cycling without severe particle pulverization, which contributes to the stable cycling performance in Na-ion batteries. Such features make the solid-state formed SnS_2/C nanospheres promising anode materials for high-performance Na-ion batteries.
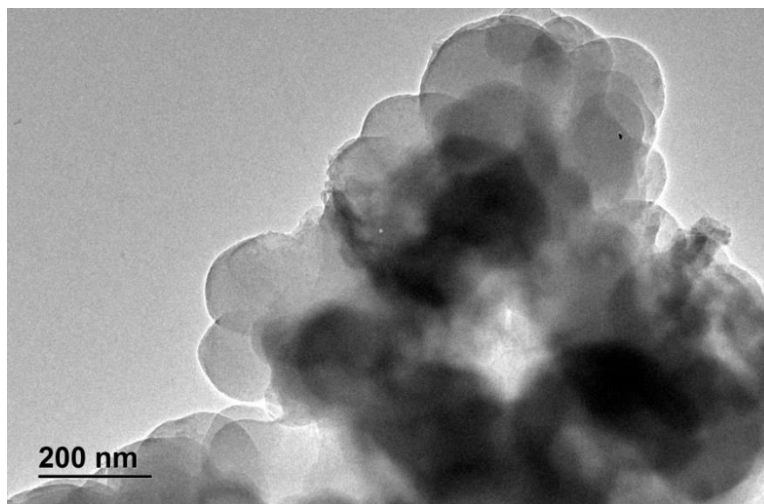
Figure 3.9 TEM image of SnS_2/C electrode after 50 cycles in Na-ion batteries.

3.4 Conclusions

The SnS_2/C nanospheres were synthesized using solid-state reaction through annealing the mixture of metallic tin, sulfur powder and PAN in a sealed vacuum glass tube. The 41% of crystal SnS_2 nanoparticles are uniformly dispersed on the carbon matrix to form 200 nm SnS_2/C composite sphere particles. The carbonization of PAN at high temperature provides a conductive carbon matrix to improve the electrical conductivity of SnS_2. The SnS_2/C anode can deliver a high specific capacity of 660 mAh/g at 50 mA/g, maintain a reversible capacity of 570 mAh/g after 100 cycles and retain capacity of 360 mAh/g even at 1 A/g. The SnS_2/C composite is robust to withstand the volume change during charge/discharge cycles as evidenced by the stable interface resistance in EIS analysis and good morphology maintenance after cycling in SEM images.

Chapter 4

An Advanced MoS$_2$/Carbon Anode for High Performance Sodium-Ion Batteries

The results presented in this chapter have been published in *Small*:

J. Wang, C. Luo, T. Gao, A. Langrock, A. C. Mignerey, C. Wang, *Small,* **2015**, *11,* 472-480 (Cover image).

4.1 Introduction

Lithium-ion batteries, the main energy supply for portable electronics, are considered as the prime candidates to power the next generation of electric vehicles (EVs) and hybrid electric vehicles (HEVs) [1,2,123]. However, the concerns on the availability and distribution of lithium resource in the earth's crust render the necessity to develop new battery chemistries. Among them, sodium-ion batteries have attracted much attention due to low cost, large resource availability, and similar insertion chemistry with lithium ions [124-126]. Inspired by Li-ion battery chemistry, a large number of cathode materials, such as transitional metal oxides, were investigated in Na-ion batteries [127,128]. However, there are not as many attempts on improving electrochemical performance of anode materials as that for cathode materials. Up to now, proposed anode materials include carbonaceous materials [129], Na-alloys (Sn, Sb) [130,131] and binary compounds (metal oxides, metal sulfides) [132-134]. Due to the similar chemistry to Li-ion batteries, carbonaceous anode materials are widely used in Na-ion batteries [135]. Recent reports on carbon nanosheet derived from peat moss [136] and hollow carbon nanowires [137] demonstrate a

reversible sodium-ion intercalation/deintercalation with specific capacities in the range of 200-300 mAh/g. Some metals (Sn, Sb) can alloy with Na exhibiting a high capacity of 400-600 mAh/g [130,131]. However, it is very difficult to maintain the high capacity during charge/discharge cycles due to the large volume change. In this regard, anode materials with high capacity and superior cycling stability are urgently needed for Na-ion batteries.

4.1.1 Previous studies of MoS_2 for energy storage applications

Recently, there is growing research interest in layered MoS_2 as an anode material for Li-ion [138,139] and for Na-ion batteries [140]. The unique layered structure is favorable for initial ion intercalation/de-intercalation, and the conversion chemistry enables high theoretical capacity. Molybdenum disulfide (MoS_2) is one of the two-dimensional transition metal dichalcogenides (TMDs) [141,142]. MoS_2 has a lamellar structure with each layer stacking via van der Waals interactions. In a single-layered MoS_2, there are numerous S-Mo-S units where molybdenum atoms are sandwiched in the center by sulfur atoms with strong covalent bonding. Due to the structural similarity to graphite but larger interlayer space, MoS_2 has been explored as an anode for high power Li-ion batteries [143-145]. The lithiation process of MoS_2 was depicted as an initial insertion process followed by a conversion reaction, leading to the formation of metallic Mo and Li_2S [146-149]. However, the delithiation mechanism is still in debate. It is unclear whether the delithiation process is dominated by the oxidation of Mo metal to MoS_2 or the oxidation of Li_2S to S [150, 151].

Due to the chemical similarity between lithium ion and sodium ion, MoS_2 can also be used in Na-ion batteries. David *et al.* reported MoS_2/graphene paper for Na-ion batteries and revealed the conversion reaction mechanism for MoS_2 and Na ions during sodiation [140]. However, the

desodiation mechanism was not clear. According to the conversion reaction between one MoS_2 molecule and four sodium ions, the theoretical capacity of MoS_2 is 670 mAh/g [152]. However, the MoS_2/graphene paper still suffers from low capacity (230 mAh/g) and poor cycle life (only 20 cycles). Thus, advanced nanostructure fabrication and fundamental understanding of the sodiation/desodiation mechanism are critical to circumvent the main challenges and obtain a stable cycling performance of the MoS_2 anode.

4.1.2 Overview of this study

In this study, MoS_2/C nanospheres with three-dimensional flower-like architecture were fabricated for use as a Na-ion battery anode. The MoS_2/C nanospheres react with Na-ion through a fully successive intercalation and conversion reaction. The MoS_2/C nanospheres exhibit a specific capacity of 520 mAh/g at 0.1 C (1 C = 670 mA/g) and maintain 400 mAh/g at 1 C for 300 cycles and demonstrate one of the best electrochemical performances as anode materials in Na-ion batteries. High cycling stability of MoS_2/C nanospheres is attributed to the formation of a stable solid electrolyte interface (SEI) layer on the MoS_2/C nanospheres in fluoroethylene carbonate (FEC)-based electrolyte, and the fully reversible conversion reaction of MoS_2 during sodiation/desodiation.
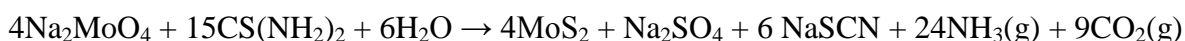
4.2 Experimental

4.2.1 Synthesis of nanostructured MoS_2 and MoS_2/C

Synthesis of MoS_2 nanosheets: All chemicals were purchased from Sigma Aldrich and used as received. A mass of 100 mg of $Na_2MoO_4 \cdot 2H_2O$ and 133 mg of NH_2CSNH_2 were dissolved in

20 mL deionized water and stirred for 10 min. The solution was then transferred into a Teflon-lined stainless steel autoclave and annealed at 240 $^{\circ}$C for 24 h. After that, the black precipitates were collected by centrifugation, washed with deionized water for three times and ethanol once, and dried in a vacuum oven at 80 $^{\circ}$C for 12 h.

The reaction for the synthesis process is believed to be:

$$4Na_2MoO_4 + 15CS(NH_2)_2 + 6H_2O \rightarrow 4MoS_2 + Na_2SO_4 + 6\ NaSCN + 24NH_3(g) + 9CO_2(g)$$

Synthesis of MoS$_2$/C nanospheres: All chemicals were purchased from Sigma Aldrich and used as received. A mass of 100 mg of $Na_2MoO_4 \cdot 2H_2O$ and 133 mg of NH_2CSNH_2 were dissolved in 20 mL deionized water, and then 334 mg of sucrose was added into the solution. After stirring for 10 minutes, the solution was clear and transferred into a Teflon-lined stainless steel autoclave. The reaction started after heat treatment at 240 $^{\circ}$C for 24 h. After that, the black precipitates were collected by centrifugation, washed with deionized water and ethanol, and dried in a vacuum oven at 80 $^{\circ}$C for 12 h. The MoS$_2$/C nanospheres were annealed in a conventional tube furnace at 800 $^{\circ}$C for 2 h in a stream of 5% hydrogen in argon flow.

4.2.2 Material characterization and electrochemical testing tools

Material Characterizations: SEM images were taken with a Hitachi SU-70 analytical ultra-high resolution SEM (Japan); TEM images were taken with a JEOL (Japan) 2100F field emission TEM; TGA was carried out using a thermogravimetric analyzer (TA Instruments, USA) with a heating rate of 5 $^{\circ}$C min^{-1} in argon; the XRD pattern was recorded using a Bruker Smart1000 (Bruker AXS Inc., USA) using CuKα radiation; Raman measurements were performed on a Horiba Jobin Yvon Labram Aramis using a 532 nm diode-pumped solid-state

laser, attenuated to give ~900 μW power at the sample surface. Fourier transform infrared spectroscopy (FTIR) was recorded with a NEXUS 670 FT-IR Instrument.

Electrochemical measurements: The MoS_2 or MoS_2/Carbon powders were mixed with carbon black and sodium alginate binder to form a slurry of active material/carbon black/sodium alginate at the weight ratio of 70:20:10. Coin cells for sodium-ion batteries were assembled with sodium foil as the counter electrode, 1 M $NaPF_6$ in a mixture of fluoroethylene carbonate/dimethyl carbonate (FEC/DMC, 1:1 by volume) as the electrolyte and Celgard 3501 as the separator. Electrochemical performance was tested using an Arbin battery test station (BT2000, Arbin Instruments, USA). Both the charge and discharge current density and specific capacity were calculated based on the mass of MoS_2 in the electrode. Cyclic voltammograms were recorded using a Solatron 1260/1287 Electrochemical Interface (Solatron Metrology, UK) with a scan rate of 0.1 mV/s between 0.005 and 2.5 V (versus Na/Na^+).

4.3 Results and discussion

4.3.1. Material Characterization

The crystal structures of as-prepared MoS_2 nanosheets and MoS_2/C nanospheres were characterized using X-ray diffraction (XRD), as shown in Fig. 4.1(a). The diffraction profiles demonstrate the phase purity of MoS_2 with crystallized hexagonal structure (JCPDS 65-0160). MoS_2/C nanospheres show conspicuous peaks at $33^°$ and $59^°$, which are indexed to the (100) and (110) planes of crystalline MoS_2, respectively [153]. The shift of the (002) peak from $14.2^°$ to $16.5^°$ is triggered by the intercalation of carbon sheets (amorphous carbon) between MoS_2 sheets, and the peak at $16.5^°$ is induced by the interlayer distance between the carbon layer and the MoS_2

layer [153, 154, 155]. Raman spectra of MoS$_2$ nanosheets and MoS$_2$/C nanospheres are shown in Fig. 4.1(b). The hexagonal layered structure of MoS$_2$ is indicated by two peaks located at 383 cm^{-1} and 408 cm^{-1}, which are typical first-order Raman active modes E^l_{2g} and A_{1g} due to in-plane vibrational modes within the sulfur-molybdenum-sulfur layer [156]. The Raman spectrum of MoS$_2$/C nanospheres exhibits two broad bands at 1360 cm^{-1} (D-band) and 1598 cm^{-1} (G-band), besides typical peaks from hexagonal structured MoS$_2$. The G-band and D-band reveal the presence of in-plane vibration of sp^2-bonded carbon atoms and vibrational modes from sp^3-bonded carbon atoms in amorphous carbon [157].
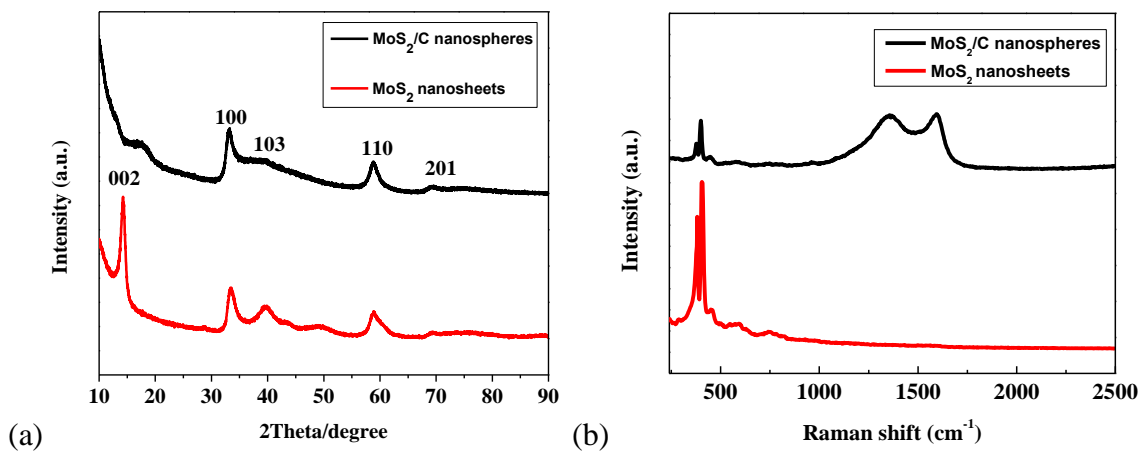

Figure 4.1 (a) XRD characterization of as-prepared MoS$_2$ and MoS$_2$/C nanospheres; (b) Raman spectra of as-prepared MoS$_2$ and MoS$_2$/C nanospheres.

To determine the weight ratio of MoS$_2$ to carbon in the sample, thermogravimetric analysis (TGA) was carried out from 25 ^{o}C to 800 ^{o}C in air, as shown in Fig. 4.2(a). The residue of MoS$_2$/C composite after TGA is MoO$_3$, as confirmed by X-ray diffraction pattern in Fig. 4.3 (MoO$_3$, JCPDS 005-0508). A major weight loss is observed in the range from 300 °C to 400 °C,

which is due to the weight loss induced by oxidation of C into CO_2 and MoS_2 into MoO_3 with the formation of SO_2 gas [139,158], based on the following reactions:

$$2\ MoS_2(s) + 7\ O_2(g) \rightarrow 2\ MoO_3(s) + 4\ SO_2(g) \qquad (4.1)$$

$$C + O_2 \rightarrow CO_2 \qquad (4.2)$$
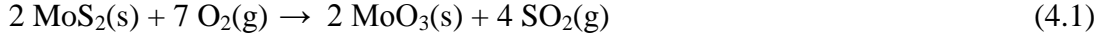
The weight loss due to the sublimation of nano-size MoO_3 was observed after 700 ^{o}C. The sublimation temperature of nanoscale MoO_3 may be lower than that of bulk MoO_3 powder (1155 ^{o}C), and most of the MoO_3 nanoparticles sublimed at 730 ^{o}C. MoO_3 nanoparticles may also begin to melt at a temperature lower than its melting point (795 ^{o}C) owing to the small size and large surface area of MoO_3 nanoparticles, similar phenomenon has been observed for other nanoparticles. Thus, it is possible that a small portion of MoO_3 nanoparticles grow into bulk MoO_3 at the temperature below the melting point of MoO_3. The resulting bulk MoO_3 will have a high boiling temperature of 1155 ^{o}C, thus left (5%) as solid MoO_3 at 730 ^{o}C. The remaining solid was characterized with XRD, and it is MoO_3 as evidenced by Fig. 4.3 with characteristic (020), (040) and (060) peaks at 14, 26, 39 degrees, respectively. The weight percentage of MoS_2 was further calculated to be 66.7% for MoS_2/C nanospheres according to Eq. 4.3:

$$MoS_2\ (wt\%) = 100 \times \frac{M_{MoS_2}}{M_{MoO_3}} \times \frac{Final\ weight\ of\ MoO3}{Initial\ weight\ of\ MoS2-C}\ (\text{M: molecular weight}) \quad (4.3)$$
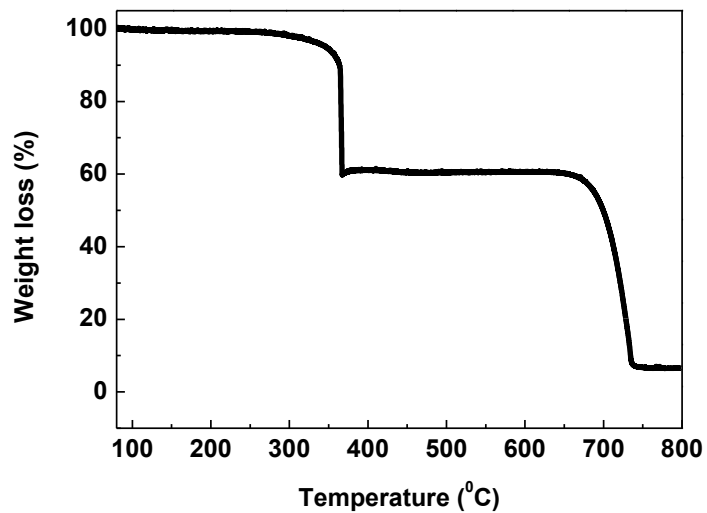
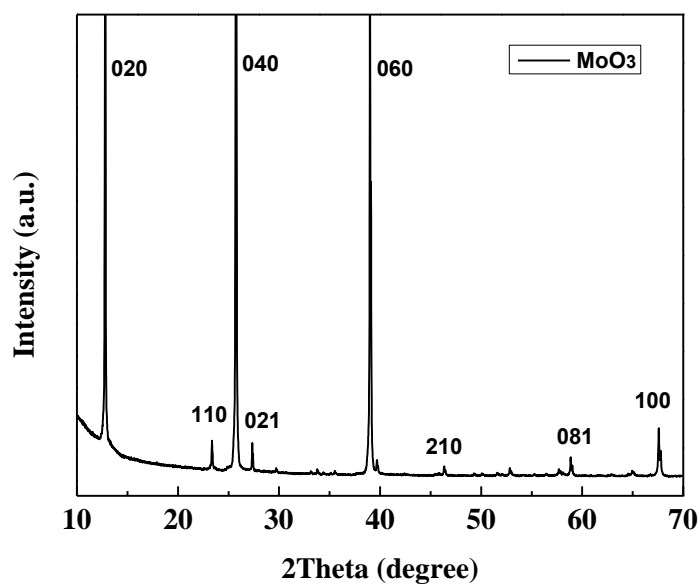Figure 4.2 TGA result of nanostructured MoS$_2$/C nanospheres in air from room temperature to 800 ^{o}C at a heating rate of 5 ^{o}C /min.

Figure 4.3 XRD characterization of MoO$_3$ resulting from TGA heating of MoS$_2$/C nanospheres in air.
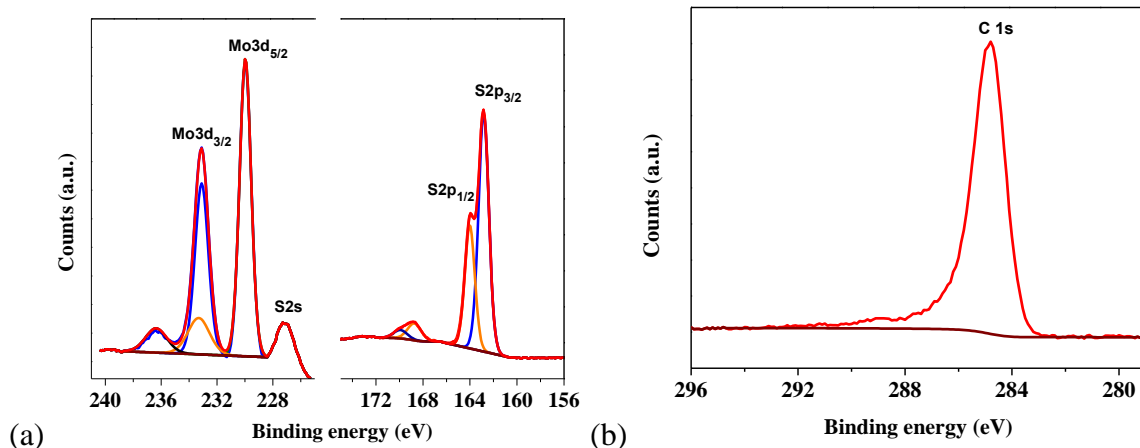
Figure 4.4 (a) XPS spectra of MoS$_2$/C composite showing Mo 3d, S 2s; (b) XPS spectra showing the C 1s peak.

Figure 4.4 shows the X-ray photoelectron spectroscopy (XPS) spectra of the MoS$_2$/C binding energy peaks with C1s reference peak at 284.8 eV. The presence of MoS$_2$ and carbon components are demonstrated by the characteristic Mo and S with an elemental ratio of ~1:2 and the prominent peak of C1s at 284.8 eV. The Mo 3d spectra shows a Mo^{6+} 3d$_{3/2}$ peak at 236 eV, a Mo^{4+} 3d$_{3/2}$ peak at 233 eV, a Mo^{4+}3d$_{5/2}$ peak at 229 eV, and the S 2s peak is detected at 227 eV. The Mo^{6+} 3d$_{3/2}$ peak presents with a small portion (18%) as compared with Mo^{4+} 3d, which is possibly due to the oxidation of Mo^{4+} in the atmosphere or the small residue of the reactant Na$_2$MoO$_4$. The S 2p spin orbit split peaks constrained with a spin orbit splitting of 1.18 eV and an area ratio of 0.5 (S 2p$_{1/2}$:S 2p$_{3/2}$ = 0.5) are shown in the range of 160-168 eV. The shoulder peak at 169 eV corresponds to the oxidized sulfur. A sharp peak of C1s is detected at 284.8 eV with a small portion of graphitic carbon in the region of 286-289 eV.
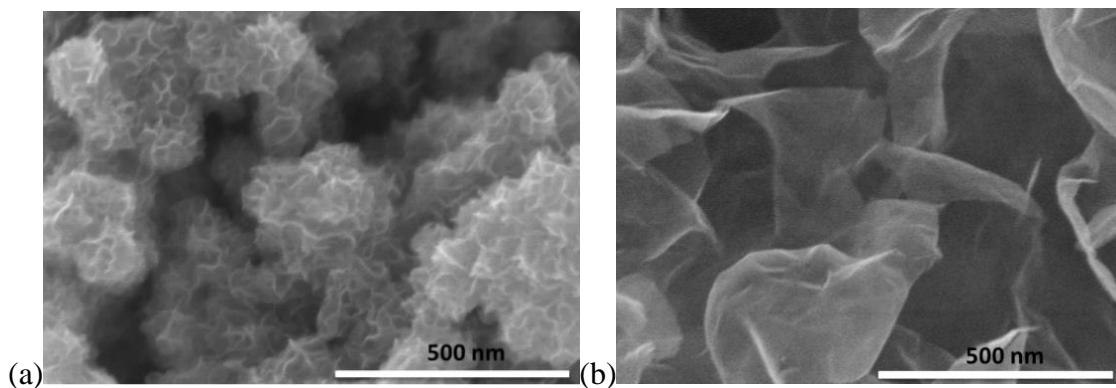
Figure 4.5 SEM images of (a) MoS$_2$/C nanospheres; (b) MoS$_2$ nanosheets.

The morphology of as-prepared MoS$_2$/C and MoS$_2$ is revealed by SEM, TEM images and energy dispersive X-ray spectroscopy (EDS) mapping. As indicated by Figure 4.4, the as-prepared MoS$_2$ forms two-dimensional nanosheets, while MoS$_2$/C displays flower-like three-dimensional nanosphere architecture after *in situ* carbon coating. The introduction of carbon remarkably reduces the size and morphorlogy of the MoS$_2$ nanosheets. The distinct ring pattern of selected-area electron diffraction (SAED) in the insets of Figure 4.5a and 4.5b reveals the crystalline nature of MoS$_2$ nanosheets and MoS$_2$/C nanospheres, which is consistent with the XRD results in Fig. 4.1a.

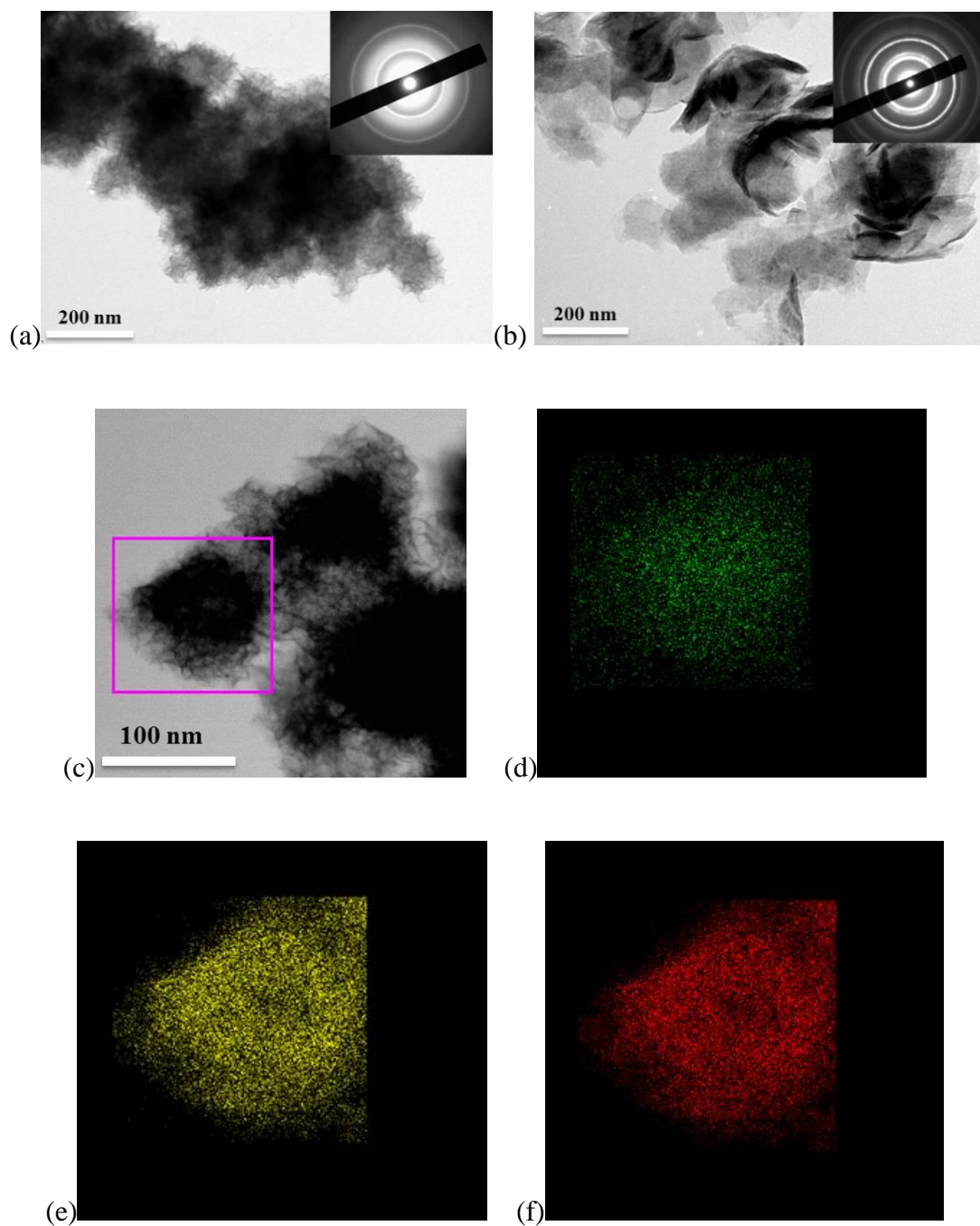Figure 4.6 (a) TEM image of MoS$_2$/C nanospheres (indexed with SAED); (b) TEM image of MoS$_2$ nanosheets (indexed with SAED); (c) elemental mapping images of MoS$_2$/C nanospheres; (d) elemental mapping image of C; (e) elemental mapping image of S; (f) elemental mapping image of Mo.
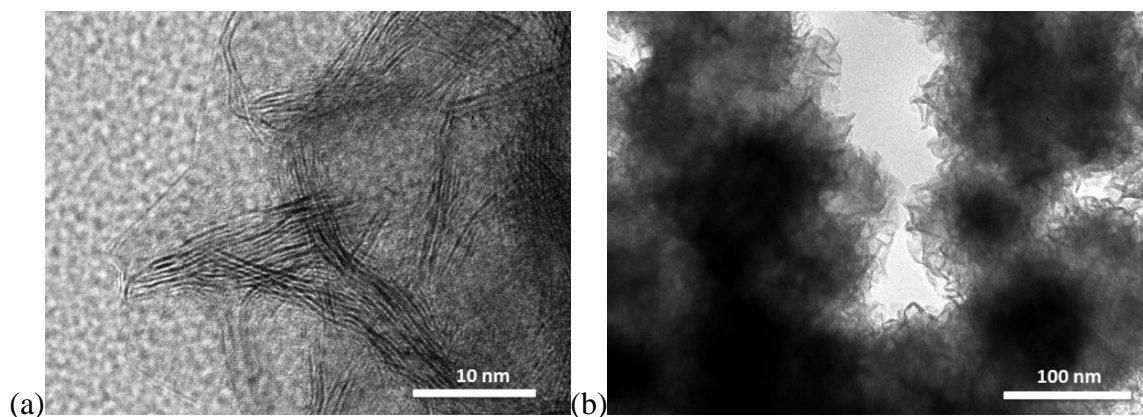
Figure 4.7 (a) High-resolution transmission electron microscopy (HRTEM) image of MoS_2/C composite; (b) TEM image of MoS_2/C composite.

The existence of amorphous carbon, Mo and S is demonstrated by elemental mapping image of MoS_2/C nanospheres as shown by Fig. 4.6(c)-(f). The EDS mapping confirms that MoS_2 is uniformly distributed in amorphous carbon matrix. To further elucidate the morphology of MoS_2/C composite, HRTEM characterization was carried out and shown in Fig. 4.7(a). The layered structure of hexagonal crystalline MoS_2 is demonstrated and the interlayer distance is consistent with previous literature [156]. The flower-like morphology and dispersion of MoS_2 in amorphous carbon are revealed in the TEM image of the MoS_2/C composite as shown in Fig. 4.7 (b).

4.3.2 Electrochemical performance

The electrochemical properties of MoS_2 nanosheets and MoS_2/C nanospheres were evaluated using coin cells with sodium metal as a counter electrode. Figure 4.8a and 4.8b show the cyclic voltammograms (CV) of a MoS_2 (nanosheets) electrode and a MoS_2/C (nanospheres) electrode in the initial five cycles, respectively. The CV curves of MoS_2 show reductive peaks at 1.2 V, 0.7 V and the corresponding oxidation peaks/shoulder at 0.6, 1.7 and 2.2 V in the first cycle (Fig.

4.8(a)). In the second sodiation, the reductive peak at 1.2 V shifts to a higher potential of 1.4 V, and the intensity of the peak at 0.7 V is reduced, while the oxidation peaks are slightly increased. The CV peaks are stable during the subsequent four cycles, demonstrating a highly reversible and stable sodiation/desodiation process. The sodiation peak at 1.4 V is attributed to intercalation of sodium ions into MoS_2 interlayers.

$$MoS_2 + xNa^+ + xe^- \rightarrow Na_xMoS_2 \qquad (4.4)$$

The peak at 0.7 V is due to the conversion reaction

$$Na_xMoS_2 + (4-x)Na^+ + (4-x)e^- \rightarrow 2Na_2S + Mo \; [140] \qquad (4.5)$$
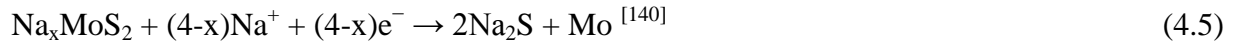
The corresponding desodiation peaks demonstrate three successive reversible reactions. The intensity decrease of the peak at 0.7 V in the following cycles suggests that the SEI film is formed on the electrode surface at this potential. SEI film formation leads to irreversible capacity loss and low Coulombic efficiency in the first cycle. The CV scans of the MoS_2/C electrode show similar peaks but are less prominent due to interference of the Na-ion insertion/extraction with the carbon coating layer. In addition, the stable redox peaks in Fig. 4.8(a) and 4.8(b) illustrate the good cycling stability of the MoS_2 and MoS_2/C electrodes.
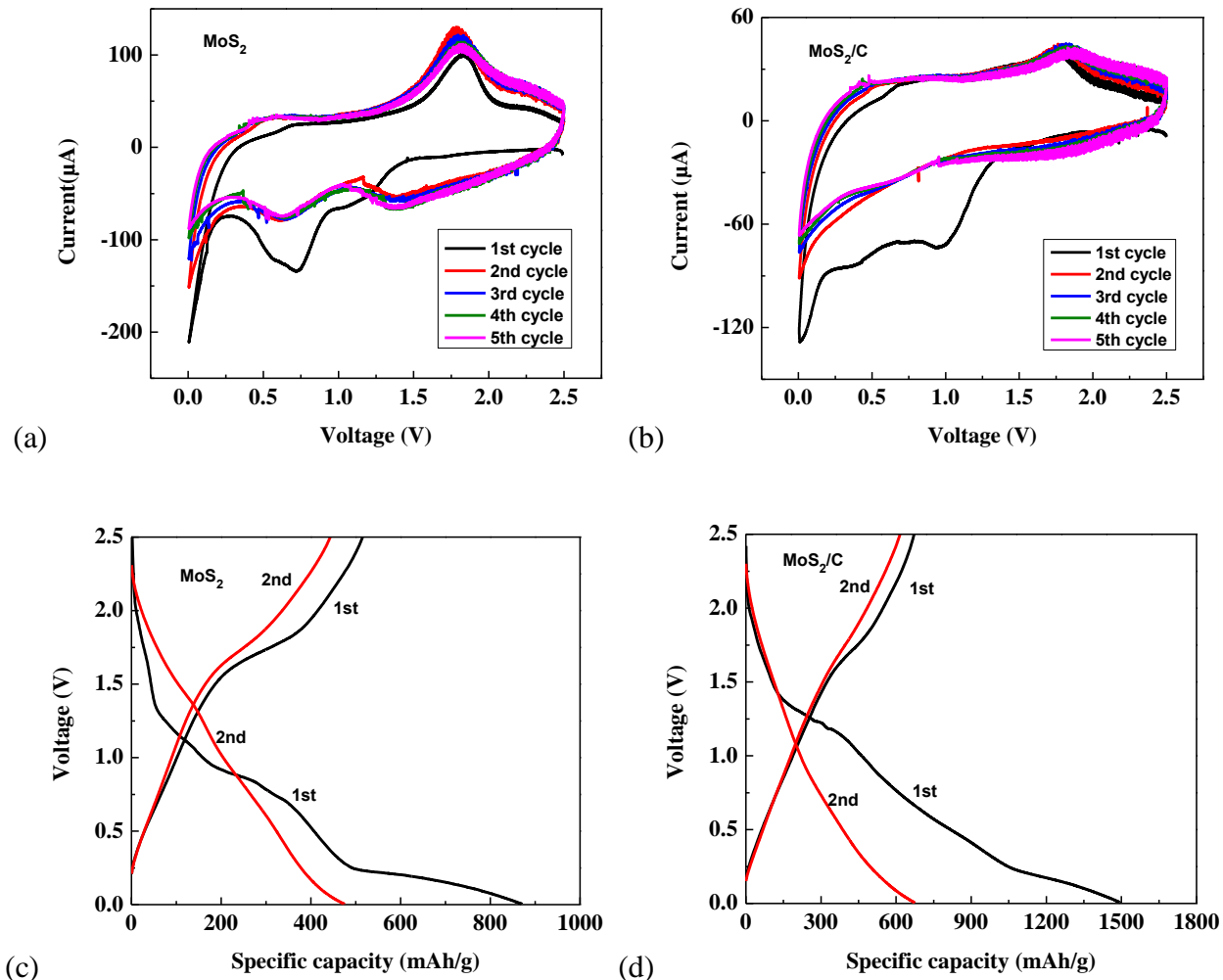
Figure 4.8 (a) Cyclic voltammograms of the MoS_2 electrode and (b) MoS_2/C electrode between 0.005 V-2.5 V with a scan rate of 0.1 mV/s; (c) Charge and discharge profiles of the MoS_2 electrode and (d) MoS_2/C electrode vs. Na^+/Na with a cut-off window 0.005 V-2.5 V.

The charge and discharge curves of the MoS_2 electrode and the MoS_2/C electrode with a cut-off window between 0.005 V and 2.5 V at a current density of 0.1 C are shown in Fig. 4.8(c) and 4.8(d). During initial sodiation, three phase transitions located at 1.4 V and 0.7 V and 0.2-0.005 V are observed in MoS_2 and MoS_2/C electrodes, which is consistent with the CV scans in Fig. 4.8(a) and 4.8(b). The first phase transition corresponds to the intercalation of sodium ions to the MoS_2 interlayer, and the second phase transition is ascribed to the conversion reaction. The

plateau at 0.2-0.005 V is due to insertion of the Na-ion into the interface between Mo and Na_2S. For the MoS_2/C electrode, a sloping curve is observed and no conspicuous potential plateau can be detected in the subsequent sodiation processes. This phenomenon is consistent with the CV curves of MoS_2/C electrode. However, the sloping plateau at 1.7 V is still visible, revealing the highly reversible oxidation reaction from Mo to MoS_2. Meanwhile, the MoS_2/C electrode displays an exceptional high desodiation capacity at 671 mAh/g in the initial cycle. The capacity of the MoS_2/C electrode is very close to the theoretical capacity (670 mAh/g) of MoS_2, which is calculated based on one MoS_2 molecule reacting with four sodium ions in the conversion reaction (Eq. 4.4, Eq. 4.5).

The cycling stability of MoS_2 and MoS_2/C electrodes was investigated at 0.1 C. As indicated by Fig. 4.9 (a), the Coulombic efficiencies of both MoS_2 and MoS_2/C electrodes after 10 cycles are close to 100%, revealing high stability of the SEI film formed in the FEC (fluoroethylene carbonate)-based electrolyte. It has been revealed that FEC can stabilize the formation of the SEI film on the electrode surface, leading to stable cycling performance [159]. All the specific capacities are calculated based on MoS_2 after subtracting the contribution from carbon, which is about 100 mAh/g at the same current density.
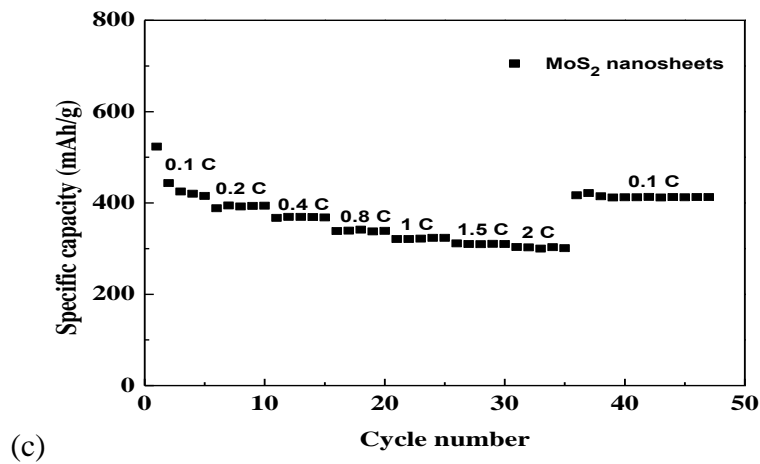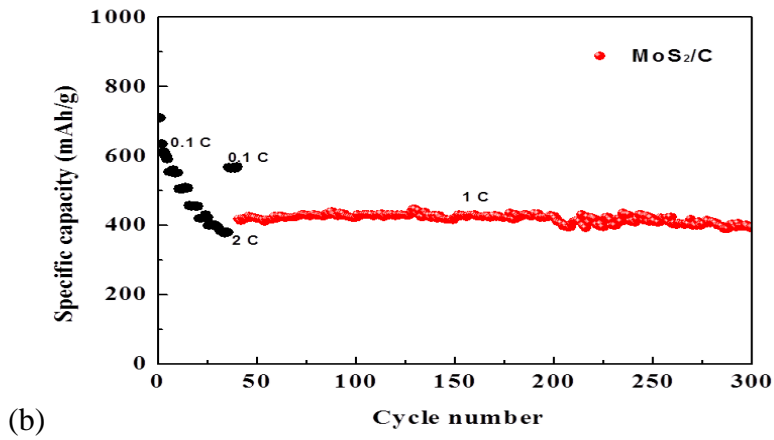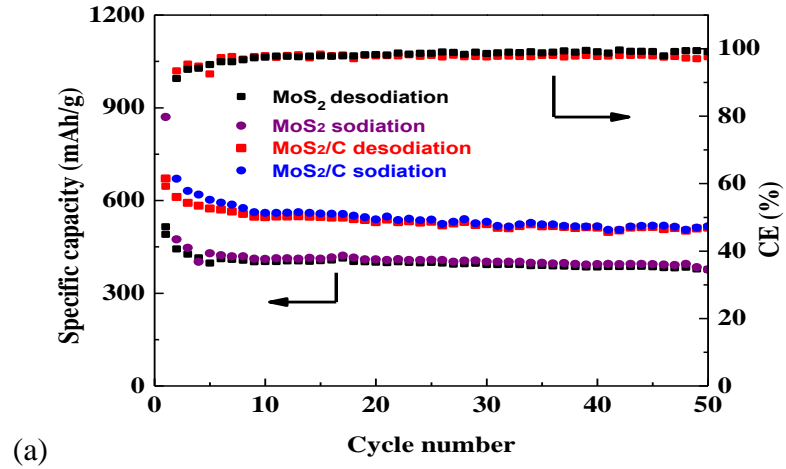
Figure 4.9 (a) Cycling performance of the MoS₂/C electrode in FEC added electrolyte (red squares, desodiation cycles; blue circles, sodiation cycles), and the MoS₂ electrode (black squares, desodiaiton cycles; purple circles, sodiation cycles. (b) Rate capability of MoS₂/C electrode (1 C = 670 mA/g); (c) Rate capability of MoS₂ electrode.

71

The MoS$_2$/C electrode displays a much higher capacity than that of the MoS$_2$ electrode. It delivers a high capacity (671 mAh/g) in the first cycle, and retains at 520 mAh/g for 50 cycles, while the MoS$_2$ electrode delivers a reversible capacity of only 360 mAh/g for 50 cycles. The cycling performance of the MoS$_2$ electrode and MoS$_2$/C electrode at high current rates is demonstrated in Fig. 4.9(b) and Fig. 4.9(c), respectively. During the charge/discharge cycles, both MoS$_2$ and MoS$_2$/C electrodes show stable cycling performance in Na-ion batteries. Even at a high current rate of 2 C, the charge capacity of MoS$_2$/C electrode is 390 mAh/g, which is an indication of its fast reaction kinetics with sodium ions. After the current density decreases to 0.1 C, the capacity of MoS$_2$/C electrode recovers to its initial capacity immediately (520 mAh/g). After rate capacity measurement, the MoS$_2$/C electrode is further cycled at a high current of 1 C to investigate the long-term cycling stability. At 1 C, the MoS$_2$/C electrode maintains a reversible capacity of 400 mAh/g for 300 cycles without obvious capacity fading (Fig. 4.9(b)). Similarly, the MoS$_2$ electrode also shows highly stable cycling capacity, although the capacity of MoS$_2$ is lower than that of MoS$_2$/C. The capacity fading of the initial cycles at a current density of 0.1 C is due to the large volume expansion during initial discharge. After that capacity loss, the MoS$_2$ electrode shows great rate capability. As current density increases from 0.1 C to 2 C, the capacity decreases from 420 mAh/g to 300 mAh/g. The charge capacity of MoS$_2$ retains 68% of its initial capacity at a current density up to 2 C. Furthermore, the capacity increases to its initial capacity (410 mAh/g) after the current density returns to 0.1 C.

The higher capacity of the MoS$_2$/C electrode is ascribed to the improved reaction kinetics by carbon coating, as further confirmed by electrical impedance spectra (EIS) of both the MoS$_2$ and MoS$_2$/C. The role of the carbon coating can be understood in three aspects: (1) smaller particle size: The introduction of carbon remarkably reduces the particle size as evidenced by SEM

72

images. (2) morphological change: The as-prepared MoS_2 exhibits nanosheet morphology while the carbon coated MoS_2 displays spherical particles, as shown by TEM images. The colloidal carbonaceous material tends to form a 3D sphere-like morphology [153,160]. (3) better electrical conductivity: The electrochemical impedance spectroscopy (EIS) measurements shown in Fig. 4.10 demonstrate that the carbon coating significantly enhances the electrical conductivity of the active material-MoS_2.

To investigate the role of carbon coating in the reaction kinetics of MoS_2, the reaction kinetics of MoS_2 with and without carbon coating were measured using EIS. The EIS curves of both MoS_2 electrodes show one depressed semi-circle in high frequency region and a straight sloping line in low frequency region. The semi-circle and a sloping line correspond to charge transfer impedance within the electrode and ion diffusion resistance, respectively. From Fig. 4.10, the MoS_2/C electrode material has extraordinary lower R_{ct} (~600 Ω) as compared with the MoS_2 electrode material (R_{ct} = ~3500 Ω), demonstrating that MoS_2/C electrode has faster reaction kinetics. The superior rate capability of the MoS_2/C electrode further confirms the essential role of carbon coating on enhancing the electrical conductivity and reaction kinetics. The small size, large surface area and short ion diffusion pathway enables easier access to Na^+, leading to exceptional battery performance.
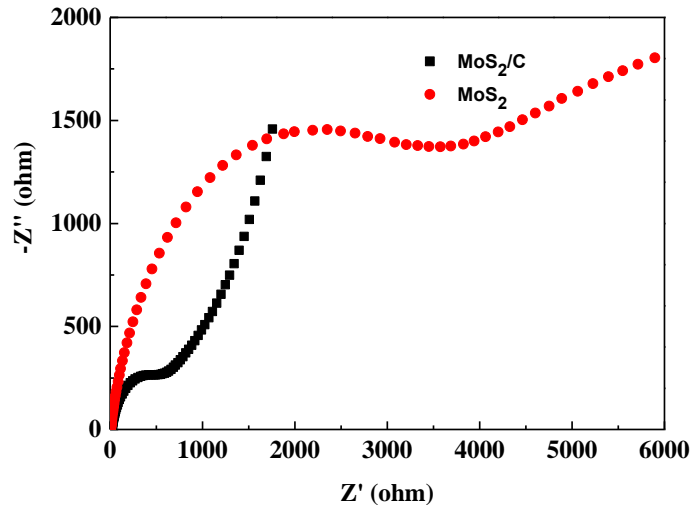
Figure 4.10 Nyquist plots of fresh MoS$_2$/C electrode and MoS$_2$ electrode in Na-ion batteries.

4.3.3 Mechanism investigation

The mechanism behind the high Coulombic efficiency, high capacity and exceptional cycling stability of MoS$_2$/C anode is investigated. The high Coulombic efficiency of MoS$_2$/C anode may be attributed to the robustness of the SEI film that can effectively accommodate volume changes. Figure 4.11 shows the morphology of the MoS$_2$/C electrode after 50 deep charge/discharge cycles. As evidenced by the SEM image, the SEI coating and volume expansion during sodiation changes flower-like MoS$_2$/C nanospheres into solid spherical nanoparticles. Meanwhile, the morphology of MoS$_2$/C electrodes after 50 cycles in FEC electrolyte was characterized using TEM (Fig.4.11(b)). Despite the particle size of MoS$_2$/C nanospheres increasing from 200 nm to 300 nm due to sodium-ion intercalation/de-intercalation, the regular nanosphere morphology is still maintained in FEC electrolyte. A shell is formed on the surface of flower-like MoS$_2$/C nanospheres, demonstrating the formation of the SEI film on the surface of MoS$_2$/C nanospheres. The SEI layer coating on the MoS$_2$/C electrode was further confirmed by FTIR. Figure 4.12

74

shows the FTIR spectra of MoS$_2$/C nanospheres, fresh MoS$_2$/C electrode and cycled MoS$_2$/C electrode. The cycled MoS$_2$/C electrode was immersed in diethylcarbonate (DEC) for 24 hours to remove NaPF$_6$. As indicated by Fig. 4.12, there are two conspicuous peaks at 1400 cm^{-1} and 1572 cm^{-1} in the spectra of cycled MoS$_2$/C electrode, representing the stretching vibration of the carbonate groups of FEC and DMC in SEI layer [161], while peaks at 1400 cm^{-1} and 1572 cm^{-1} are absent in the spectra of MoS$_2$/C powder and fresh MoS$_2$/C electrode.
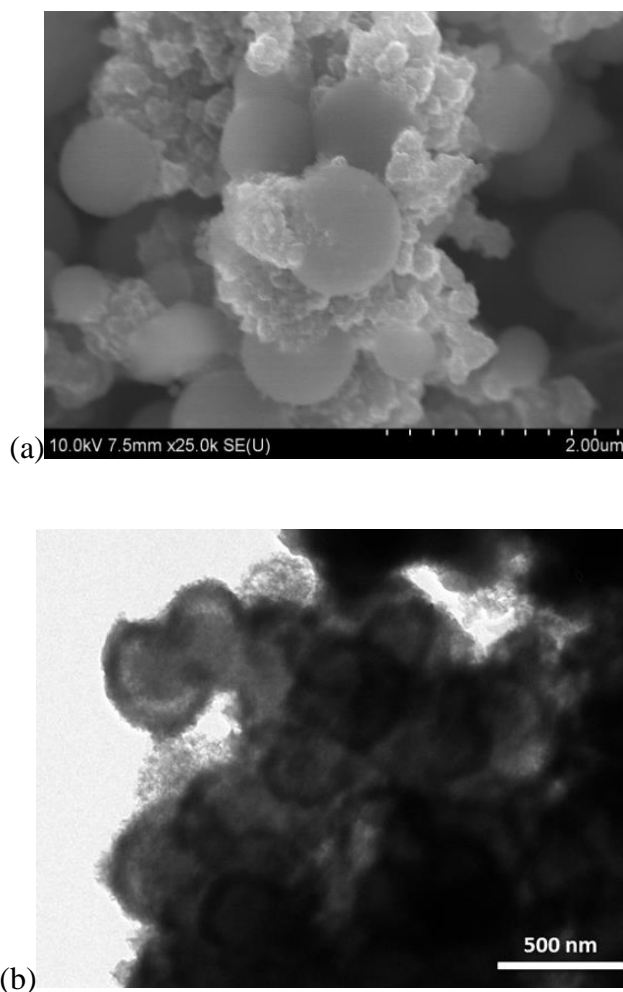

(a)

(b)

Figure 4.11 (a)The SEM image of MoS$_2$/C nanospheres after 50 cycles in Na-ion batteries; (b) The TEM image of MoS$_2$/C nanospheres after 50 cycles in Na-ion batteries.
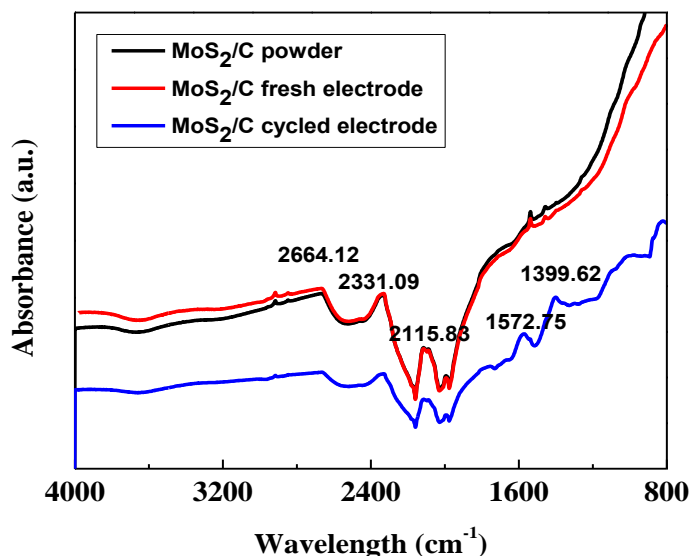
Figure 4.12 FTIR spectra of MoS$_2$/C nanosphere powders (black curve), fresh MoS$_2$/C electrode without cycling (red curve), and MoS$_2$/C electrode after 50 charge/discharge cycles(blue curve) in Na-ion batteries.

The conversion reaction mechanism (Na$_x$MoS$_2$ + (4-x) Na$^+$ + 4e$^-$ → 2Na$_2$S + Mo) in MoS$_2$/C electrodes, suggested by CV and galvanostatic charge/discharge profiles in Fig. 4.8, was further confirmed by the structural evolution during sodium-ion intercalation and extraction. *Ex-situ* XRD studies were carried out to compare the composition changes of fresh MoS$_2$/C electrode, fully discharged and charged electrodes, as plotted in Fig. 4.13.

To understand the structural change at sodiation state, the cell was fully discharged to 5 mV, then charged to 2.5 V and maintained at 2.5 V for 24 hours. Before XRD measurements, the electrode was immersed in DEC to remove NaPF$_6$. The fresh MoS$_2$/C electrode shows the characteristic (100) peak at 33 degrees, suggesting the crystalline structure of MoS$_2$. The peaks at 43, 51 degrees in the XRD pattern are attributed to the copper current collector. The existence of a peak at 27 degrees is due to the addition of carbon black in the electrode. After sodiation

76

(discharge), the MoS_2 in the MoS_2/C electrode converts to Mo and Na_2S. The existence of Na_2S was revealed by its characteristic peak at 39 degrees (JCPDS No. 03-0933) and a weak signal from unreacted MoS_2 was shown in the fully discharged cell. No crystal Mo peaks can be observed in the discharged MoS_2/C electrode, probably due to the formation of amorphous Mo [162,163]. At desodiation after one fully discharge/charge cycle, the existence of crystalline MoS_2 was observed, as evidenced by the characteristic (100) peak at 33 degrees. It is worth noticing that a small peak of Na_2S was also observed in the fully charged electrode, which is due to the incomplete reaction of Na_2S during the desodiation process. Meanwhile, crystalline sulfur is not detected, suggesting the complete reaction from Na_2S to MoS_2 rather than S during desodiation.
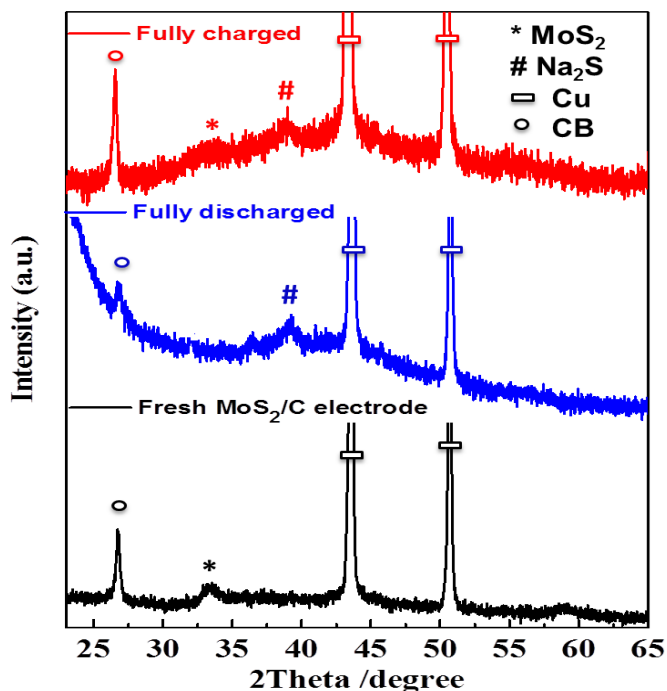
Figure 4.13 Structural changes of MoS_2/C electrodes before and after discharge/charge cycles (peaks of MoS_2 are labeled as *, # for Na_2S, squares for Cu current collector and circles for carbon black).

4.4 Conclusion

In summary, flower-like MoS_2/C nanospheres were fabricated as Na-ion battery anodes. The MoS_2/C nanospheres show high capacity, long cycle life and exceptional rate capability in Na-ion batteries. They deliver a reversible capacity of 520 mAh/g at a current density of 0.1 C. After increasing the current density to 1 C, MoS_2/C nanospheres maintain a specific capacity of 400 mAh/g for 300 cycles, demonstrating the exceptional cycling ability and fast reaction kinetics. Such an excellent electrochemical performance of the MoS_2/C anode in Na-ion batteries is ascribed to the carbon coating, small size and the formation of a stable SEI layer. The superior battery performance of MoS_2/C nanospheres demonstrates that MoS_2 is a promising anode material for Na-ion batteries. Furthermore, the reversibility of the conversion reaction between MoS_2 and sodium ions was demonstrated by *ex-situ* XRD. The electrochemical performance and reversible sodiation/desodiation mechanism of MoS_2/C nanospheres paves the way for the feasibility of high-performance Na-ion batteries.

Chapter 5

One-Step Aerosol Spray Pyrolysis of MoS$_2$/C Nanospheres for High-Capacity and Stable Na-Ion Battery Anode

5.1 Introduction

In Chapter 4, MoS$_2$/C nanoflowers were fabricated via hydrothermal method and the novel material shows superior electrochemical performance (520 mAh/g) with reversible conversion reaction for sodium storage [164]. Despite the excellent cycling performance shown by MoS$_2$/C or MoS$_2$/graphene composite, the preparation process involves the time-consuming and low yield hydrothermal synthesis of MoS$_2$, energy-consuming thermal reduction of graphene oxide and complicated purification process [164,166]. Therefore, it is not feasible for large scale production of uniformed nanomaterial.

Herein, for the first time, MoS$_2$/C nanomaterial was *in-situ* synthesized with aerosol spray pyrolysis in which ammonia tetrathiomolybdate ((NH$_4$)$_2$MoS$_4$) was used as a precursor solution and sucrose as a carbon source. This synthetic route enables mass production of MoS$_2$/C nanomaterials for Na-ion battery application with a low cost and facile one-pot synthesis. The annealed MoS$_2$/C nanomaterials can be directly used for electrode preparation without further purification. This is distinctly different from the hydrothermal method and makes the spray pyrolysis method more feasible for scalable application. The introduction of sucrose improves the electrical conductivity and reaction kinetics of MoS$_2$, since the carbonized sucrose serves as a conductive matrix for MoS$_2$. Meanwhile, it seems that the colloidal carbonaceous material tends

to form a 3D sphere-like morphology [167]. Experimental observations show that the as-prepared MoS_2/C composite forms a sphere-like nanostructure and shows superior sodium storage capability with high reversible capacity (~600 mA/g) after 100 deep galvanostatic cycles. Extensive results from *ex-situ* scanning electron microscopy (SEM) and transmission electron microscopy (TEM) images show that the nanosphere morphology is preserved without obvious particle pulverization and aggregation, leading to high capacity retention after hundreds of charge/discharge cycles.

5.2 Experimental

5.2.1 Material synthesis and structural characterization

Synthesis: All chemicals were purchased from Sigma Aldrich and used as received. The MoS_2/C composite was prepared by aerosol spray pyrolysis of the aqueous solution of ammonium tetrathiomolybdate $(NH_4)_2MoS_4$ and sucrose. The synthetic process is depicted in Fig. 5.1. The aqueous solution of $(NH_4)_2MoS_4$ and sucrose is used as the precursor solution and sprayed by an ultrasonic atomizer. The aerosol is transported with the flow of carrier gas through a high temperature tube furnace, in which the sample was heated up to 700 °C. The resulting product was filtered and collected as black powder. A mass of 1g $(NH_4)_2MoS_4$ and 2 g sucrose were mixed and dissolved in 200 mL of deionized water, and the clear red solution was stirred at room temperature for 2 hours. The USP system for aerosol spray was flushed with N_2 prior to solution addition. The solution was heated up to 700 °C under N_2 and remained at 700 °C for 4 hours. A fine orange-red mist was observed during the heat treatment and the final product was collected on the cooler as black powder.
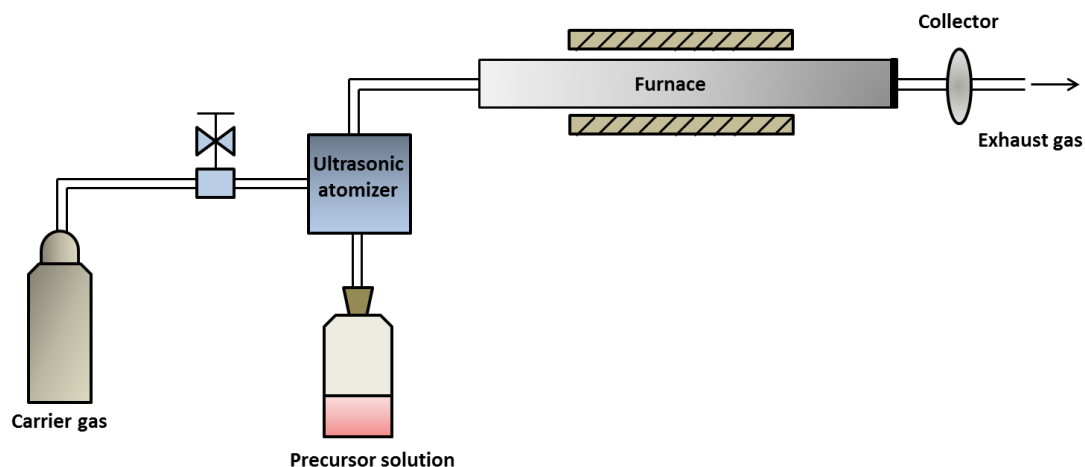
Figure 5.1 Schematic representation showing synthesis of MoS$_2$/C composite.

Material Characterizations: SEM images were taken by a Hitachi SU-70 analytical ultra-high resolution SEM (Japan); TEM images were taken by a JEOL (Japan) 2100F field emission TEM; TGA was carried out using a thermogravimetric analyzer (TA Instruments, USA) with a heating rate of 5 °C min^{-1} in argon; the XRD pattern was recorded using a Bruker Smart1000 (Bruker AXS Inc., USA) using CuKα radiation; Raman measurements were performed on a Horiba Jobin Yvon Labram Aramis using a 532-nm diode-pumped solid-state laser, attenuated to give ~900 µW power at the sample surface. X-ray photoelectron spectroscopy (XPS) analysis was performed on a high sensitivity Kratos AXIS 165 X-ray photoelectron spectrometer using monochronic AlKα radiation.

5.2.2 Coin-cell assembly and characterization

Electrochemical measurements: The as-prepared MoS$_2$/Carbon composite was mixed with carbon black and sodium alginate binder to form a slurry at the weight ratio of 70:20:10. Coin cells for sodium-ion batteries were assembled with sodium foil as the counter electrode, 1 M NaPF$_6$ in a mixture of fluoroethylene carbonate/dimethyl carbonate (FEC/DMC, 1:1 by volume)

as the electrolyte and Celgard 3501 as the separator. The electrochemical performance was tested using an Arbin battery test station (BT2000, Arbin Instruments, USA). Both the charge and discharge current density and specific capacity were calculated based on the mass of MoS_2 in the electrode. Cyclic voltammograms were recorded using a Solatron 1260/1287 Electrochemical Interface (Solatron Metrology, UK) with a scan rate of 0.1 mV/s between 0.005 and 2.5 V (versus Na/Na^+).

5.3 Results and Discussion

5.3.1 Spray-pyrolysis synthesis of MoS$_2$/C composite

The XRD pattern shown in Fig. 5.2(a) demonstrates the phase purity of MoS_2 with crystallized hexagonal structure (JCPDS 65-0160). The MoS_2/C composite shows conspicuous peaks at 33° and 59°, which are indexed to (100) and (110) planes of crystalline MoS_2, respectively [168]. The typical (002) reflection peak at 14.2° is not observed in the MoS_2/C composite, indicating that the material contains few layers graphene-like MoS_2 [169].

(a)

(b)
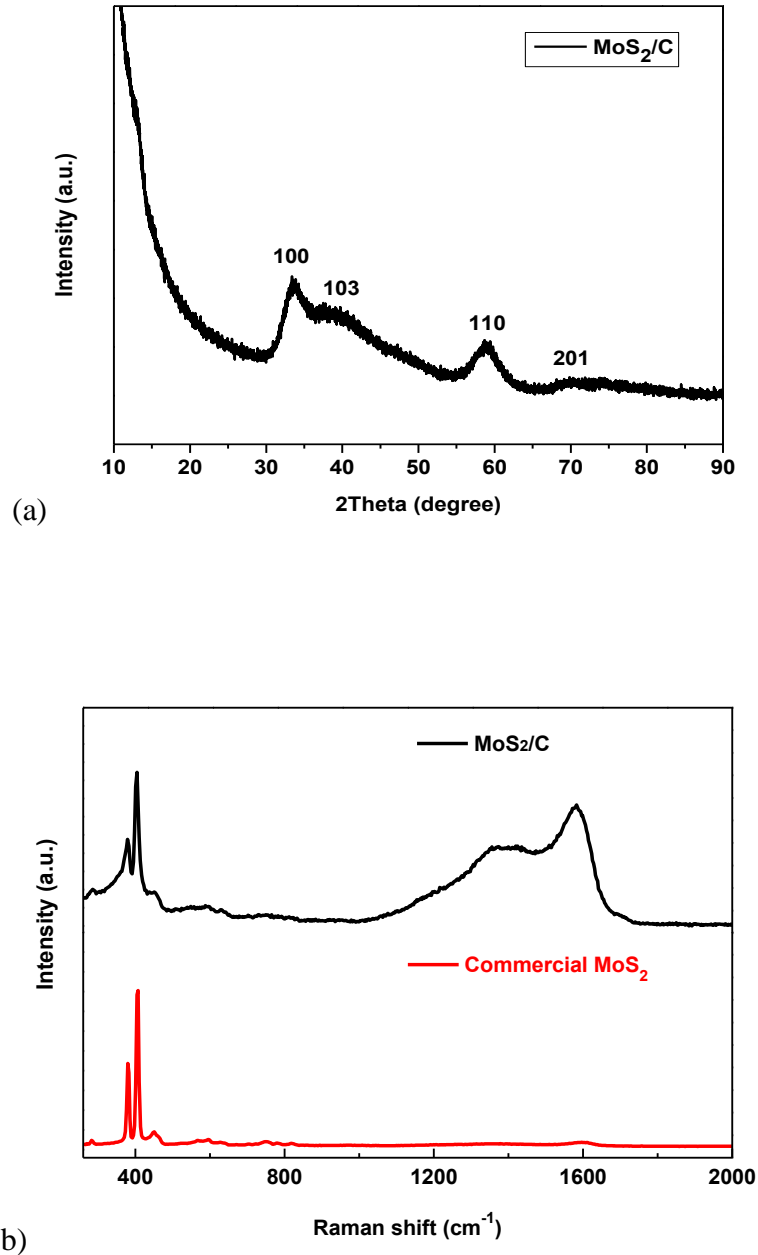
Figure 5.2 (a) XRD of aerosol-spray formed MoS_2/C composite; (b) Raman spectra of MoS_2/C composite at room temperature using 532 nm wavelength excitation.

Raman spectra of MoS_2/C composite in the range of 300-2000 cm^{-1} and 300-500 cm^{-1} are shown in Fig. 5.2(b). As shown in Fig. 5.2(b), there are two typical peaks of hexagonal layered structure of MoS_2 located at 383 and 408 cm^{-1}, which are attributed to first-order Raman active

modes E^I_{2g} and A_{1g}, due to in-plane vibrational modes within the sulfur-molybdenum-sulfur layer [170]. The Raman spectrum of MoS$_2$/C nanospheres exhibits two broad bands at 1360 cm^{-1} (D-band) and 1598 cm^{-1} (G-band), and the intensity ratio of the D/G bands is 3:4 as demonstrated by Fig. 5.2(b). The G-band and D-band reveal the presence of in-plane vibration of sp^2-bonded carbon atoms and vibrational modes from sp^3-bonded carbon atoms in amorphous carbon [171].

5.3.2 Composition analysis with TGA, XPS and electron microscopy
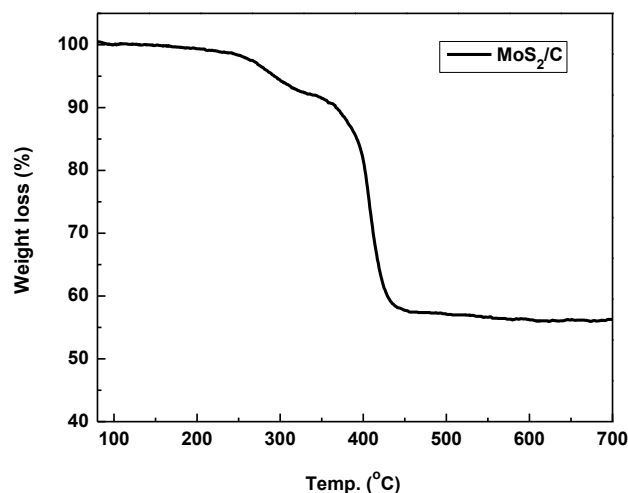
Figure 5.3 TGA results of MoS$_2$/Carbonized sugar (MoS$_2$/C) composite from 25 ^{o}C to 800 ^{o}C in air at a heating rate of 5 ^{o}C/min.

The weight ratio of MoS$_2$ to carbon in the sample was characterized by thermogravimetric analysis (TGA) as shown in Fig. 5.3, which was carried out in air from room temperature to 800 ^{o}C. A small weight loss is observed (2%) when the temperature is less than 100 °C due to the

evaporation of water on the surface of MoS_2/C composite. A further weight loss of 10% between 100 and 350 °C is attributed to the carbon oxidization in air. A major weight loss is observed in the range from 350 °C to 400 °C, which is due to the weight loss induced by oxidation of C to CO_2 and MoS_2 to MoO_3 [164,172]. The TGA result indicates that the as-prepared MoS_2/C nanospheres contain 62.2% of MoS_2 and 37.8% of amorphous carbon.

(a)

(b)

(c)

Figure 5.4 XPS spectra of MoS$_2$/C composite showing (a) Mo 3d; (b) S 2p; (c) C 1s.

Figure 5.4 shows the X-ray photoelectron spectroscopy (XPS) peak fitted Mo 3d, S 2p and C 1s spectra for the MoS$_2$/C powder with the C 1s reference peak at 284.8 eV. The presence of MoS$_2$ and carbon components are demonstr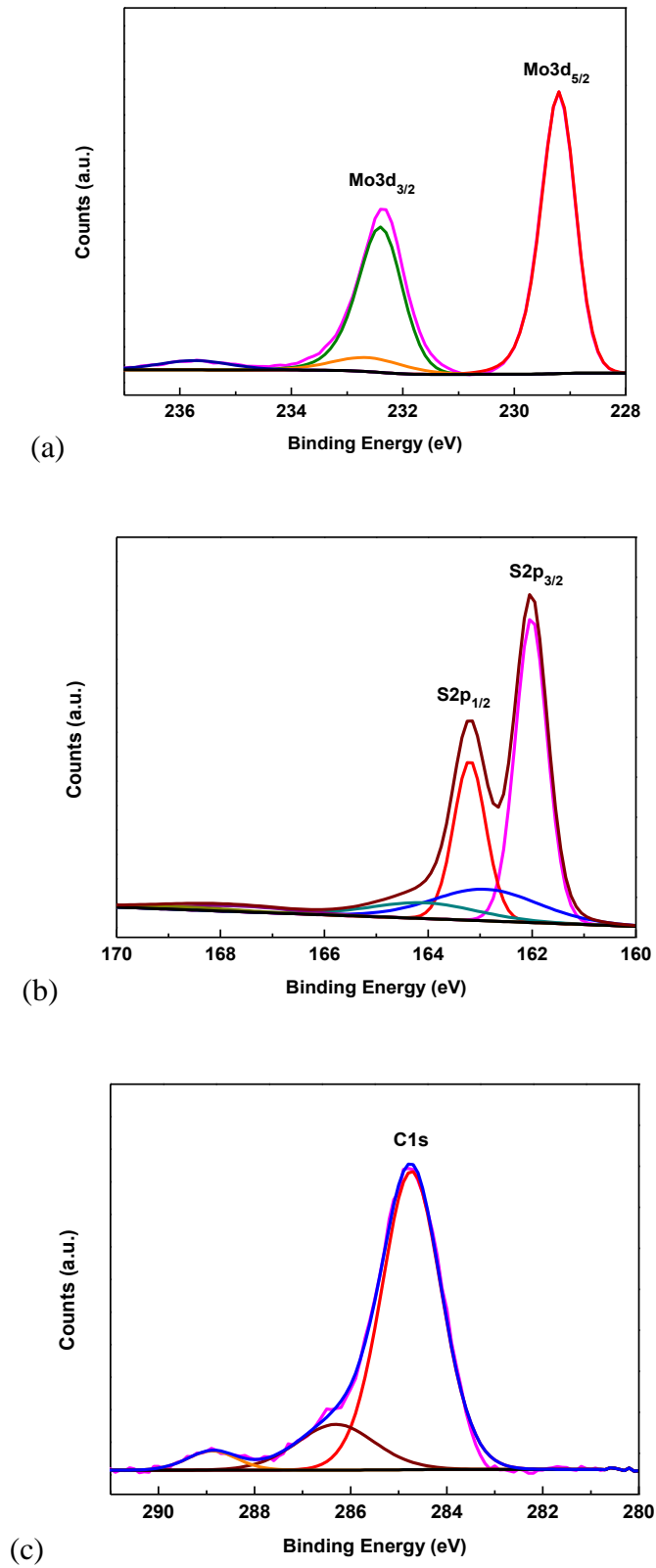ated with the characteristic Mo and S elemental ratio of ~1:2. From Fig. 5.4(a), the binding energy position of the Mo^{4+} 3d$_{5/2}$ peak is 229.3 eV and the Mo^{4+} 3d$_{3/2}$ is at a higher binding energy of 232.4 eV. The Mo 3d doublet at higher binding energy, shown as small shoulder curves at 232.5 eV and 235.8 eV, corresponds to Mo^{6+} 3d, and is possibly due to the oxidation of Mo^{4+} in the atmosphere or the small amount of residue of the reactant (NH$_4$)$_2$MoS$_4$. From Fig. 5.4(b), the S 2p spin orbit split peaks constrained with a spin orbit splitting of 1.18 eV and an area ratio of 0.5 (S 2p$_{1/2}$:S 2p$_{3/2}$ = 0.5). The existence of oxidized sulfur (SO$_x^{2-}$, X ≥ 2) is detected at higher binding energy position of 168 eV, and is a very small portion (4.5%) as compared with S 2p. Figure 5.4(c) shows a sharp peak of C 1s at 284.8 eV, which is due to C-C or C-H bonding. A small portion of graphitic carbon (C-O or COOR) is detected at higher binding energy (289 eV and 286.4 eV).
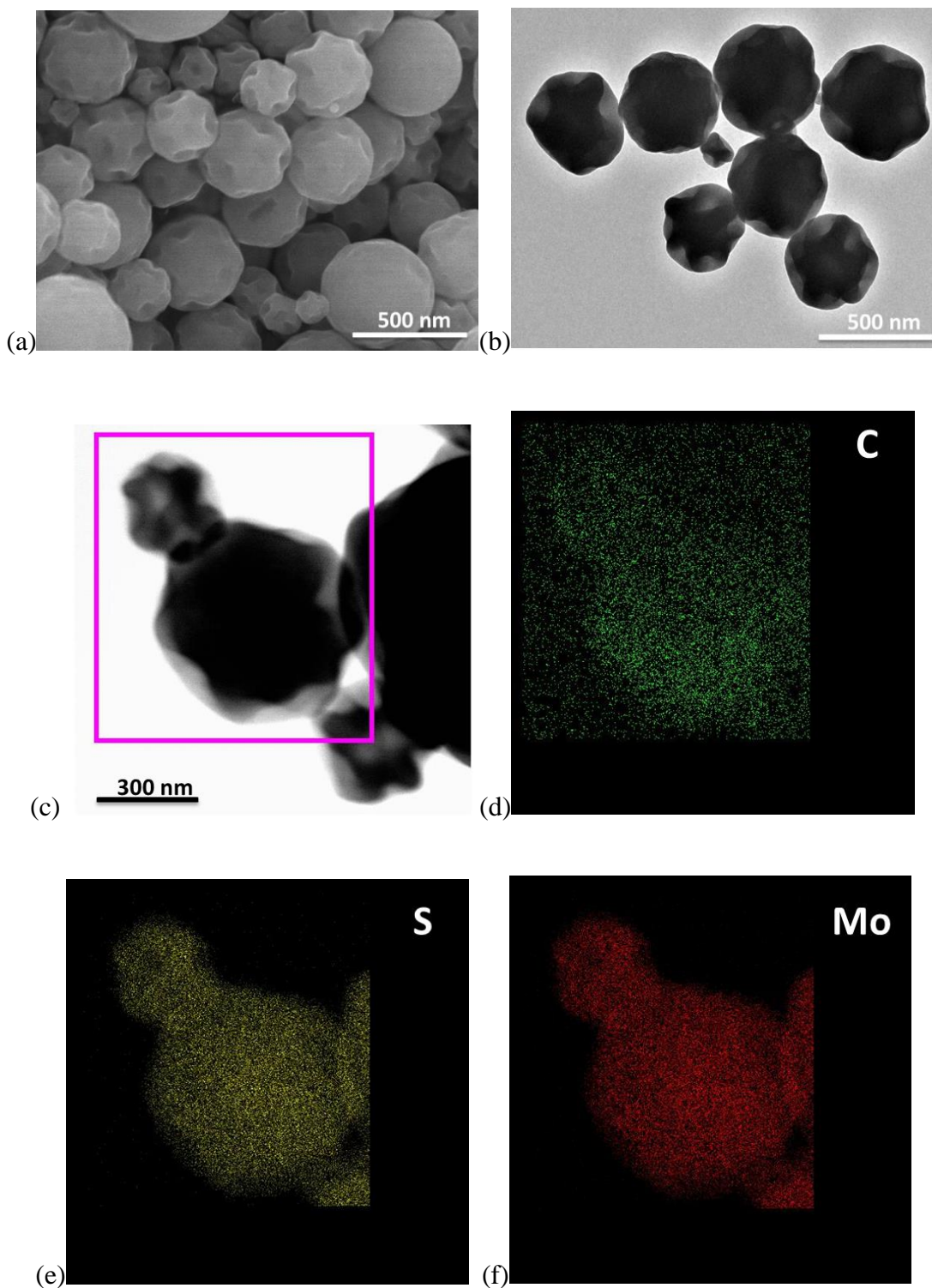
Figure 5.5 (a) SEM image of aerosol-spray formed MoS$_2$/C composite; (b) TEM image of aerosol-spray formed MoS$_2$/C composite; (c) elemental mapping images of MoS$_2$/C composite; (d) elemental mapping image of C; (e) elemental mapping image of S; (f) elemental mapping image of Mo.

Figure 5.5 displays the scanning electron microscopy (SEM) and transmission electron microscopy (TEM) images of MoS_2/C composite. After *in situ* carbon coating, MoS_2/C composite displays three-dimensional nanosphere morphology with particle size in the range of 200-500 nm. The existence of amorphous carbon, Mo and S is demonstrated by Energy-Dispersive X-ray Spectroscopy (EDX) mapping, as shown in Fig. 5.5(c)-(f). The result confirms that MoS_2 is uniformly distributed in the amorphous carbon matrix.

5.3.3 The electrochemical properties of MoS_2/C nanospheres

The electrochemical properties of MoS_2/C nanospheres are evaluated using coin cells with sodium metal as a counter electrode. The charge and discharge curves of MoS_2/C electrode with a cut-off window between 5 mV and 2.5 V at a current density of 0.1 C is shown in Fig. 5.6(a). (1C = 670 mA/g) During initial sodiation, one flat plateau is observed at 0.3 V, which is ascribed to the conversion reaction between MoS_2 and sodium ions. During desodiation, a sloping plateau at 1.7 V is visible, revealing the oxidation reaction from Mo to MoS_2 [165]. Figure 5(b) shows the cyclic voltammograms (CV) of MoS_2/C (nanospheres) electrode in the initial three cycles. The CV curves of MoS_2/C show the reductive peaks at 1.2 and 0.3 V and one corresponding oxidation peak at 1.7 V in the first cycle. The sodiation peak in 1.2 V is attributed to the intercalation of sodium ions into the MoS_2 interlayer ($MoS_2 + xNa^+ + xe^- \rightarrow Na_xMoS_2$). The peak at 0.3 V is due to the conversion reaction: $Na_xMoS_2 + (4-x) Na^+ + (4-x) e^- \rightarrow 2Na_2S + Mo$.
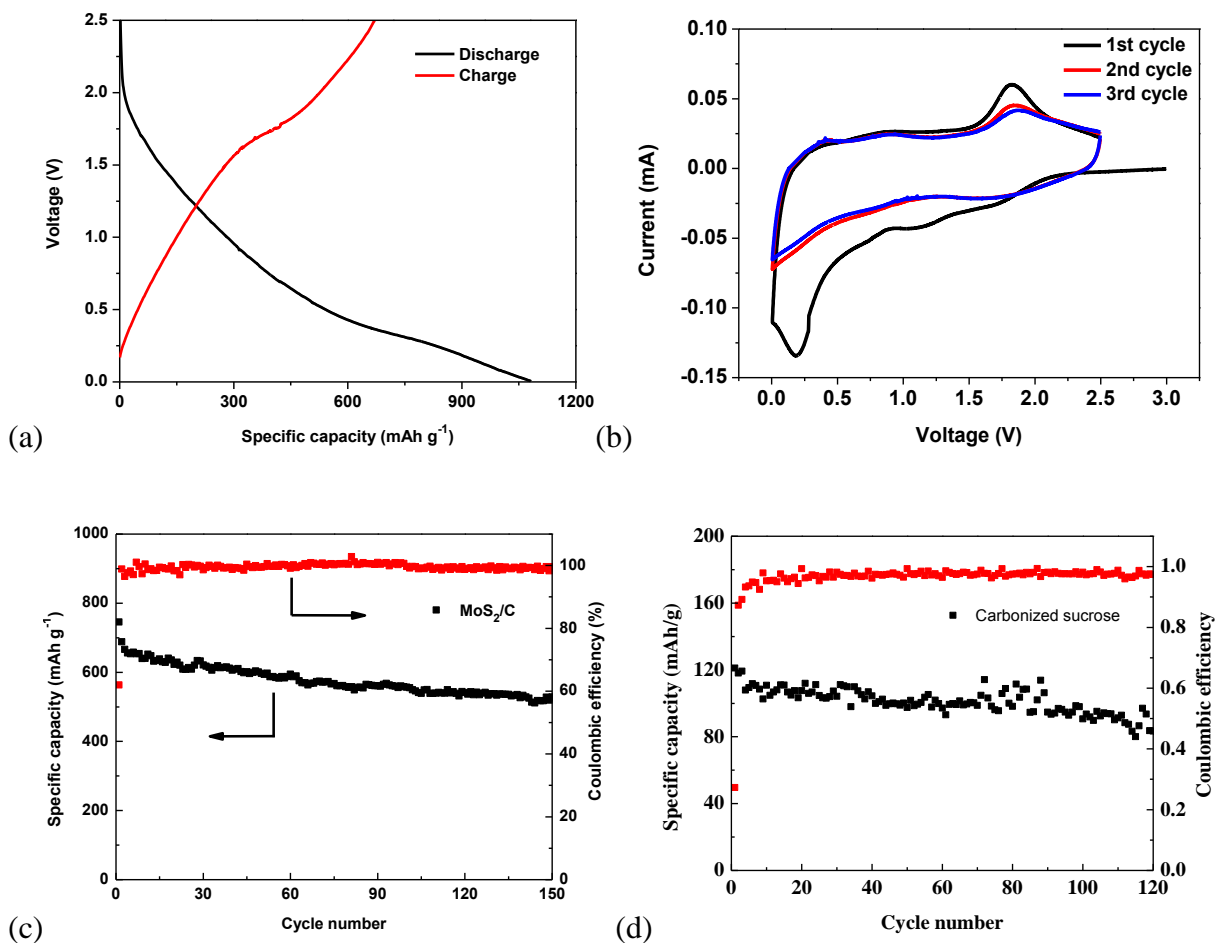
Figure 5.6 (a) charge and discharge profiles of MoS$_2$/C electrode vs. Na$^+$/Na with a cut-off window of 0.005-2.5 V; (b) cyclic voltammograms of MoS$_2$/C electrode between 0.005-2.5 V with a scan rate of 0.1 mV/s; (c) cycling performance of MoS$_2$/C electrode at 0.1 C (1 C = 670 mA/g) in Na-ion batteries; (d) cycling performance of carbonized sucrose in Na-ion batteries.

The corresponding desodiation peak demonstrates the oxidation of Mo to MoS$_2$. During subsequent cycles, the reduction peaks cannot be seen due to the amorphourization of the MoS$_2$ nanostructure and the interference of Na-ion insertion/extraction to carbon coating layer, while the oxidation peak at 1.7 V is still present with decreased intensity. The intensity decrease of the peak at 0.7 V in the following cycles suggests that a solid electrolyte interface (SEI) film is formed on the electrode surface at this potential. SEI film formation leads to irreversible capacity

90

loss and low Coulombic efficiency in the first cycle. Meanwhile, the CV peaks are stable during the subsequent four cycles, demonstrating a highly reversible and stable sodiation/desodiation processes.

Figure 5.6(c) shows the cycling performance of MoS_2/C electrodes at a current density of 0.1 C. All the specific capacities are calculated based on MoS_2 after subtracting the contribution from carbon, which is shown in Fig. 5.6(d) and is about 100 mAh/g at the same current density. Firstly, the Coulombic efficiencies of MoS_2/C electrodes after the initial cycle are close to 100%, revealing highly efficient sodiation/desodiation processes and high stability of the SEI layer formed in FEC-based electrolyte. FEC can stabilize the formation of the SEI layer on the electrode surface, leading to stable cycling performance [173]. The MoS_2/C electrode delivers a high capacity (730 mAh/g) in the first cycle and a charge capacity of 669 mAh/g in the subsequent cycle, which is very close to the theoretical capacity (670 mAh/g) of MoS_2 calculated based on one MoS_2 molecule reacting with four sodium ions in the conversion reaction.

5.3.4 Reaction kinetics of MoS_2/C electrode

Figure 5.7(a) shows the rate capability of the MoS_2/C electrode at various current rates. During the charge/discharge cycles, the MoS_2/C electrode demonstrates stable cycling performance in Na-ion batteries. The electrode delivers high charge capacity even at high current rates, which is an indication of its fast reaction kinetics. After the current density decreases to 0.1 C, the capacity of the electrode recovers to its initial capacity immediately (670 mAh/g).

(a)

(b)
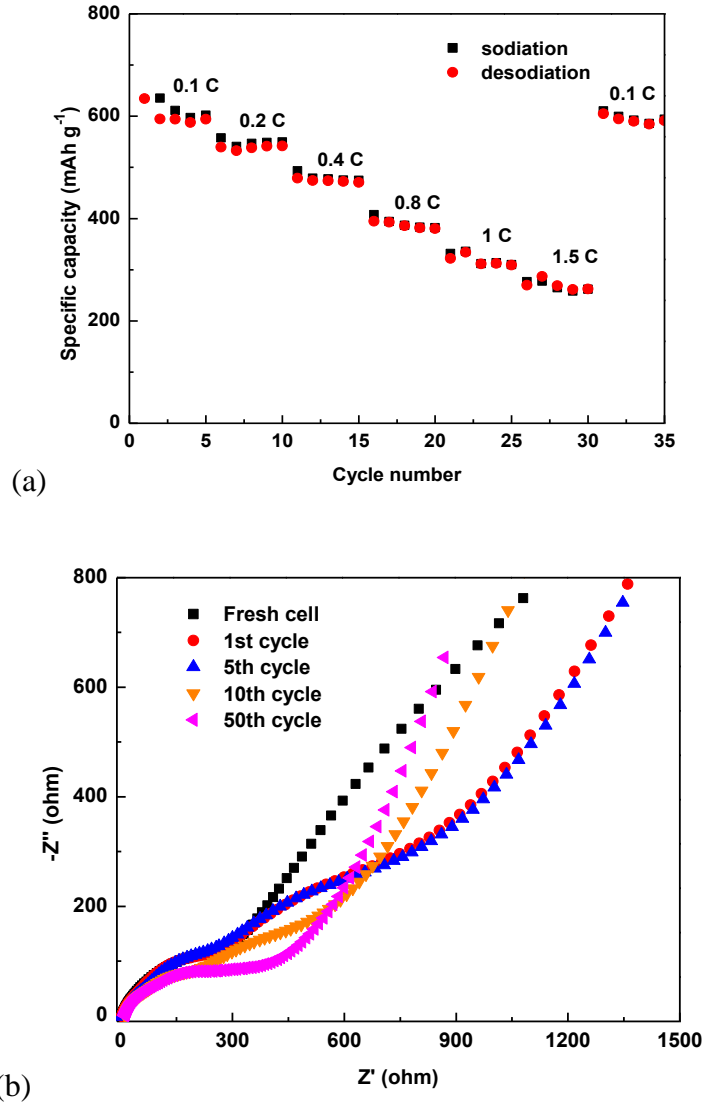
Figure 5.7 (a) Rate capability of MoS$_2$/C electrode in Na-ion batteries. (1C = 670 mA/g); (b) Electrochemical impedance spectra of MoS$_2$/C electrode before and after 1st cycle, 5th, 10th and 50th cycles in Na-ion batteries.

The impedance analysis for the MoS$_2$/C electrode was characterized by electrochemical impedance spectroscopy (EIS) before cycling and after 1st, 5th, 10th and 50th cycles. The EIS of the MoS$_2$/C electrode is characterized by a depressed semi-circle in the high frequency region and a straight sloping line in the low frequency region. The depressed semi-circle corresponds to

92

interface impedances (SEI impedance, and charge transfer resistance), and the low-frequency sloping line is due to the Na-ion diffusion resistance in the MoS_2/C particles. As shown in Fig. 5.7, the interface resistance of the MoS_2/C electrode is about 300 Ω before cycling, and it increases slightly to 360 Ω after 50 cycles in Na-ion batteries. The stable impedance before and after cycling demonstrates the robustness of the stable SEI layer and the robust structural integrity during charge/discharge cycles.
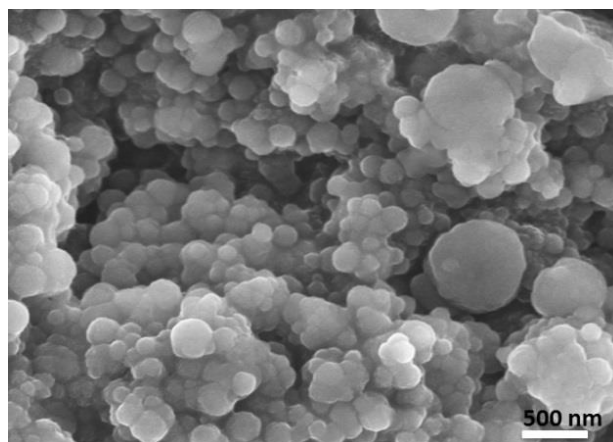
Figure 5.8 SEM image of MoS_2/C electrode after cycling in Na-ion batteries.
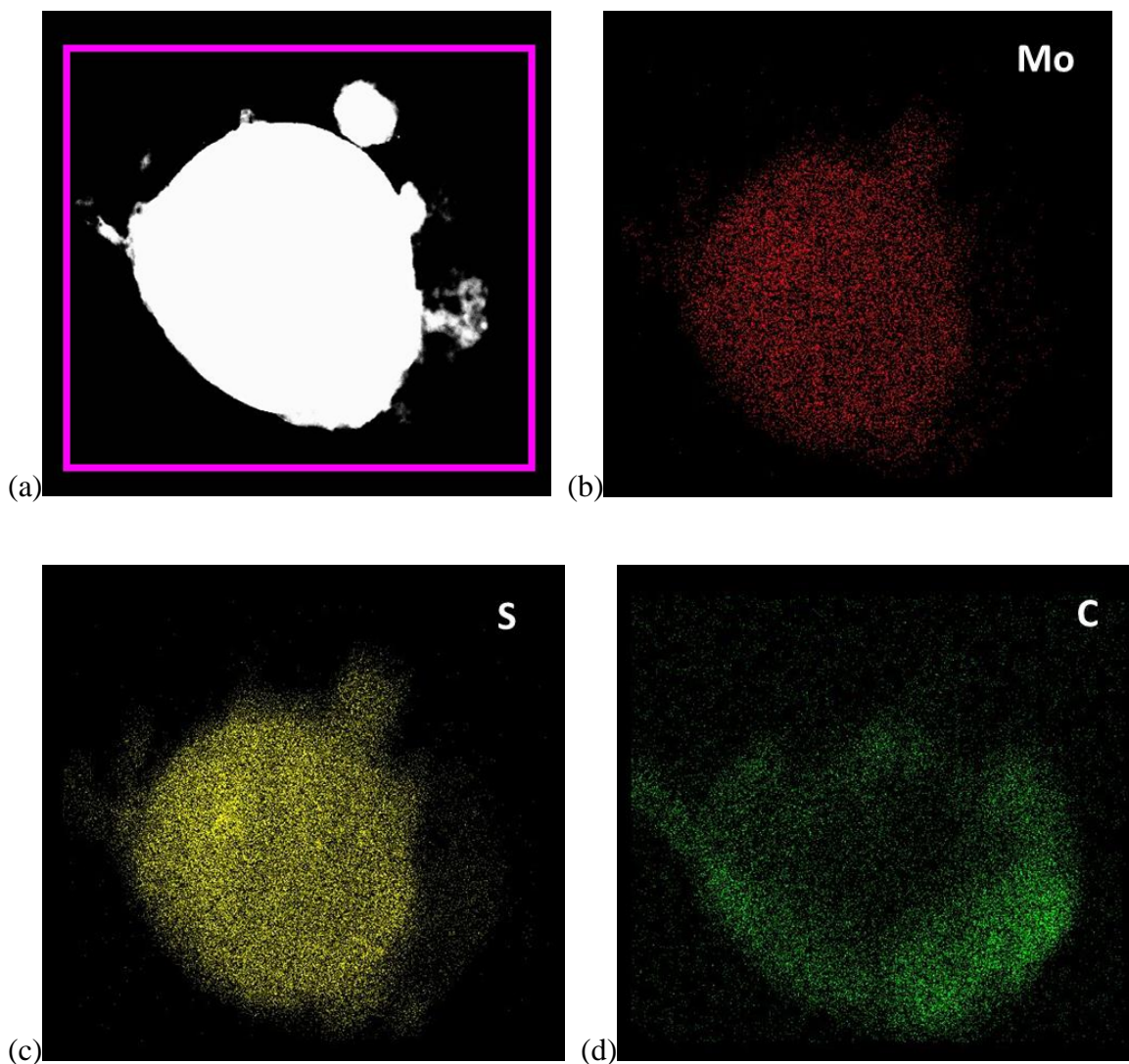
Figure 5.9 (a) elemental mapping images of MoS$_2$/C electrode after cycling in Na-ion batteries; (b) elemental mapping image of Mo; (c) elemental mapping image of S; (d) elemental mapping image of C.

Figure 5.8 shows the morphology of MoS$_2$/C electrode after 50 cycles in SEM image. The regular spherical particles can be clearly observed. The particle size is mainly preserved as 200 nm with a few large particles with a diameter of 500 nm. It shows that the morphology change of MoS$_2$/C nanospheres is negligible before cycling and after 50 cycles, and there are no observable structural cracks, particle pulverization or volume expansion induced by the strain during

repeated charge/discharge cycles. This result demonstrates that MoS_2/C electrode is able to maintain its structural and morphological integrity after cycling without severe particle pulverization, which contributes to the stable cycling performance in Na-ion batteries. Such features make the aerosol spray pyrolysis synthesized MoS_2/C nanospheres promising anode materials for high-performance Na-ion batteries. Figure 5.9 shows EDS mapping images of a MoS_2/C electrode after cycling. The results demonstrate uniform distribution of element Mo and S, indicating the structural integrity of MoS_2 after extended cycling in Na-ion batteries.

5.4 Conclusion

The MoS_2/C composite was synthesized using a one-step aerosol spray pyrolysis with ammonia tetrathiomolybdate $(NH_4)_2MoS_4$ as the precursor and sucrose as the carbon source. This synthetic route enables mass production of MoS_2/C nanomaterials for Na-ion battery application with low cost and facile one-pot synthesis. The annealed MoS_2/C nanomaterials can be directly used for electrode preparation without further purification. This is distinctly different from the hydrothermal method and makes the spray pyrolysis method more feasible for scalable applications. With the introduction of sucrose, the electrical conductivity and reaction kinetics of MoS_2 can be significantly improved since the carbonized sucrose serves as a conductive matrix for MoS_2. The structure of MoS_2 was characterized with XRD and XPS, while the content of MoS_2 in the as-prepared MoS_2/C composite was determined by TGA. The MoS_2 nanoparticles are uniformly dispersed in the carbon matrix to form 200-500 nm MoS_2/C composite spherical particles, as demonstrated by SEM, TEM images and EDS mapping. The MoS_2/C anode can deliver a reversible capacity of 590 mAh/g after 100 cycles. Even at a high current density of 1 C,

a high reversible capacity of 320 mAh/g can be retained. The MoS_2/C composite synthesized using aerosol spray pyrolysis is robust to withstand the volume change during charge/discharge cycles as evidenced by the stable interface resistance in EIS analysis and good morphology maintenance after cycling in SEM and TEM images. Therefore, the aerosol spray pyrolysis synthesized MoS_2/C nanospheres are promising anode materials for high-performance Na-ion batteries.

Chapter 6: Conclusion & Future Work

6.1 Conclusion

Rechargeable lithium ion batteries have promoted considerable revolution to the state-of-the-art energy storage technologies because of the commercialization of portable electronics and the potential for widespread implementation on plug-in hybrid electric vehicles. To advance such technologies, it is of great importance to develop high capacity anode materials with high performance for lithium and sodium storage to substitute for conventional carbonaceous materials. There is growing research interest in layered metal sulfides due to their high theoretical capacities based on conversion reaction mechanism, two-dimensional structure and large availability. This dissertation has aimed to push forward the large-scale application of LIBs and SIBs and reveal the potential of layered metal sulfides as promising anode materials. Modification of the synthesis of tin sulfides nanomaterials has successfully prepared SnS/C and SnS_2/C composites with a facile one-pot synthesis, which enables feasible large-scale production of tin sulfide nanoparticles. SnS/C nanospheres exhibit high capacity (900 mAh/g) and long cycle life (200 cycles) at a current density of C/5 in lithium ion batteries. The slow capacity degradation originates from the large volumetric change caused by the redox reaction of Li-rich alloys as evidenced by *ex-situ* studies. From *ex-situ* SEM images, the cycled SnS/C electrode between 0.01-3 V shows regular spherical shape without structural cracks, demonstrating its ability to maintain structural integrity and contributing to its superior lithium-ion storage capability. The superior cycling performance of the SnS/C electrode and the in-depth mechanism

investigation from *ex-situ* SEM and XRD pave the way for the feasibility of high-performance Li-ion batteries.

Sodium-ion batteries have garnered great attention recently and been considered as alternatives to lithium-ion batteries due to low-cost, large availability and similar chemistry with lithium storage. The research detailed in this dissertation aims to develop advanced anode materials with high specific capacity and long cycle life in sodium-ion batteries. However, it is challenging to achieve stable cycling ability because of the large ion size of Na ions. Tin disulfide (SnS_2) has a potential as an anode material in SIBs owing to its unique layered structure, high theoretical capacity and low cost. A simple solid-state reaction method was developed, in which the carbon coated SnS_2 (SnS_2/C) anode material was synthesized by annealing metallic Sn, sulfur powder and polyacrynitrile (PAN) in a sealed vacuum glass tube. The resulting SnS_2/C nanospheres exhibit a high reversible capacity of 660 mAh/g at a current density of 50 mA/g, and maintain at 570 mAh/g for 100 cycles with a degradation rate of 0.14% per cycle, demonstrating one of the best cycling performances in all reported SnS_2/C anodes for Na-ion batteries to date. The *ex-situ* characterization showed that the stable nanosphere morphology and structural integrity during charge/discharge cycles contributed to the superior cycling performance of SnS_2/C nanospheres.

Molybdenum disulfide (MoS_2) is a promising candidate for a high performance sodium-ion battery anode due to high capacity through successive intercalation and conversion reactions. There are some challenging issues such as poor cycling stability, low rate capability and unclear electrochemical reaction mechanism for the MoS_2 anode in Na-ion batteries. In this study, the findings are as follows: (1) The 3D flower-like MoS_2 nanospheres with carbon coating were synthesized as anodes for Na-ion batteries; (2) The 3D flower-like MoS_2 nanosphere anodes

showed the best cycling performance for Na-ion batteries reported to date, delivering a reversible capacity of 520 mAh/g at 0.1 C and maintaining at 400 mAh/g for 300 cycles at a high current density of 1 C; (3) The mechanism of MoS_2/C for solidation/desolidation was explored and the fully reversible conversion reaction of MoS_2 was confirmed with *ex-situ* X-ray diffraction (XRD) measurements in which a conspicuous signal from MoS_2 was detected after charging to 2.5 V; (4) The formation of a stable SEI layer in fluoroethylene carbonate (FEC) based electrolyte was demonstrated by fourier transform infrared spectroscopy (FTIR) measurements. This paves the way for the feasibility of high performance sodium-ion batteries.

Despite the fact that MoS_2 is well recognized as a competitive anode material in SIBs, the scalable synthesis of MoS_2 with controlled nanostructure design and uniform carbon coating is still challenging. This research optimized the synthetic route of carbon coated MoS_2 nanoparticles via a one-step spray pyrolysis in which sucrose is introduced as a carbon source and uniformly coated on the surface of MoS_2 nanoparticles. This synthetic route enables mass production of MoS_2/C nanomaterials for Na-ion battery application with low cost and facile one-pot synthesis. The annealed MoS_2/C nanomaterials can be directly used for electrode preparation without further purification, which makes the spray pyrolysis method more feasible for scalable application. The resulting MoS_2/C nanomaterial from spray-pyrolysis delivers higher capacity (670 mAh/g at 0.1 C) and superior cycling performance for hundreds of cycles in Na-ion batteries. It is robust to withstand the volume change during charge/discharge cycles, as evidenced by the stable interface resistance in electrochemical impedance spectroscopy (EIS) analysis and good morphology maintenance after cycling in the scanning electron microscopy (SEM) image. This study contributes to the synthesis routes of MoS_2 nanomaterials and is beneficial to the widespread application in Na-ion batteries. Future studies can be carried out to

minimize the nanosize of MoS_2/C nanospheres, and more stable cycling performance should be achieved in Na-ion batteries.

6.2 Future work

6.2.1 Electrospun one-dimensional SnS_2/Carbon fibers for sodium ion battery anodes

Recent approaches on the preparation of one-dimensional nanomaterials demonstrate a new direction for the implementation of sodium-ion batteries. Tin disulfide (SnS_2) is a promising anode material in sodium ion batteries owing to its unique layered structure, high theoretical capacity and low cost. An advanced anode material can be developed by combining the layer-to-layer packed structure of SnS_2, the introduction of a carbon source and one-dimensional nanostructure design. This novel one-dimensional nanostructure possesses several advantages: (1) the incorporation of carbon nanofibers act as a conductive matrix to encapsulate SnS_2 particles with poor electron conduction. (2) the dispersion of SnS_2 nanoparticles in carbon nanofibers mitigate volumetric expansion induced by sodiation/delsodiation process; (3) SnS_2/C nanofibers can be used directly as an electrode without binder and current collector, which remarkably decreases the weight of inactive materials in the electrode; (4) SnS_2 nanoparticles with a smaller size give rise to larger surface area and shorter Na-ion diffusion distance, which enables easier access to Na^+, faster kinetics and smaller volume expansion, leading to exceptional battery performance. Furthermore, PAN is used as the carbonaceous material in this study. PAN is selected because the carbonization percentage of PAN is relatively high compared with other commercial polymers, such as polyethylene glycol and polyacrylic acid.

The electrospinning technique will be employed to prepare SnS_2/C nanofibers, while polyacrynitrile (PAN) can serve as a carbon source. Figure 6.1 shows the schematic diagram of electrospinning equipment. It is an efficient, inexpensive and simple device [174]. It consists of a syringe, a pipette with taylor cone, and a rotating cylinder-shaped collector, powered by an ultrahigh potential supply (10 kV). The precursor solution is filled into the syringe for electrospinning. The liquid is forced out through a very fine needle and numerous fibers with ultra-small size are formed uniformly and spread on the rotating collector.
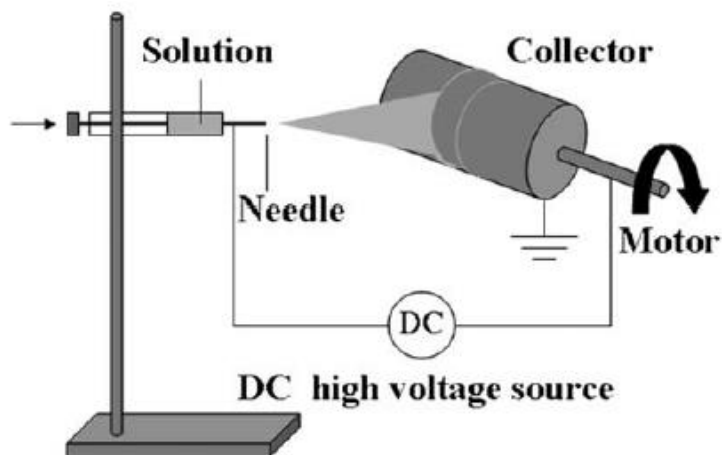
Figure 6.1 Schematic illustration of the electrospinning equipment [174].

The combination of SnS_2 and PAN carbonization is favorable because of the following advantages: i) efficient electron conduction within the SnS_2/C electrode; ii) fast ion transport through the interface and within the SnS_2/C electrode; iii) the incorporation of carbonized PAN immobilizes and disperses the SnS_2 particles, and accommodates volume expansion of SnS_2 particles during sodiation. The carbonization of PAN will be realized simultaneously and thus such a conductive carbon matrix can encapsulate the active material (SnS_2) with high specific

capacity. The resulting SnS$_2$/Carbon fibers could act as a binder free and current collector free electrode for Na-ion batteries.

6.2.2 *In-situ* TEM investigation of structural changes during cycling

Despite the high theoretical capacities of metal sulfides for Li-ion and Na-ion battery anodes, the volumetric expansion during lithiation/sodiation is the primary technology bottleneck. It is well recognized that there are internal stresses stemming from the alloying process (e.g. Sn + 4.4Li$^+$ + 4.4e$^-$ → Li$_{4.4}$Sn). The large amount of lithium intercalation induces anisotropic volume expansion, which triggers particle pulverization and insufficient contact with the current collector and results in rapid battery degradation. Therefore, the large volume change has been considered a critical issue that hinders the practical application of tin sulfides in sodium storage. To further understand the fundamental science during battery cycling, *in-situ* TEM characterizations provide opportunities to directly observe and control the structural changes caused by lithium/sodium insertion.
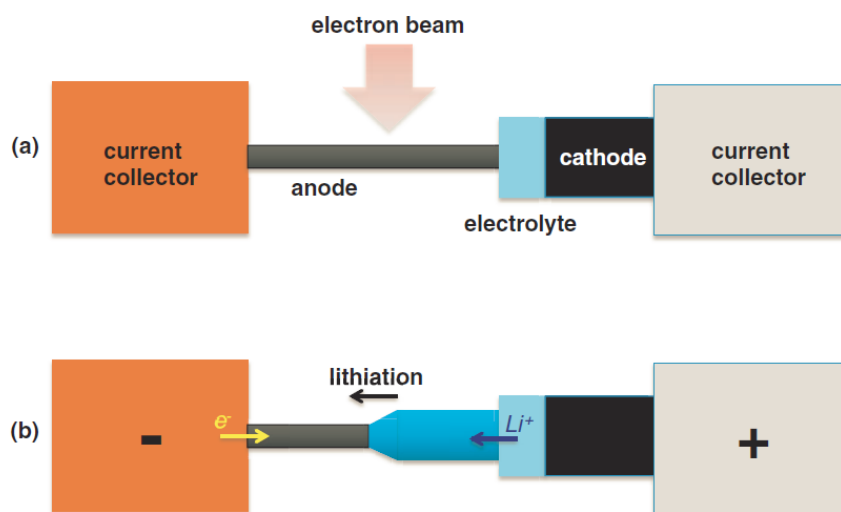
Figure 6.2 Schematic illustration of *in-situ* TEM setup: (a) a nanobattery setup for anode study; (b) operation of the nanobattery for lithiation of the anode [175].

Figure 6.2 shows a schematic setup to investigate the anode material. The *in-situ* TEM experiments require an electron transparent anode with nanostructure or thin film, a vacuum-compatible electrolyte (such as ionic liquids, polymer or other inorganic solid-state electrolytes), and a Li source (such as a discharged cathode) [175, 176]. These can reveal the mechanical degradation during cycling and investigate the sodiation behavior of SnS_2 and MoS_2. A more detailed investigation about the formation mechanism of structural cracks and strains during cycling paves the way for developing advanced anode materials with stable cycling capability in Li-ion and Na-ion batteries.

Bibliography

1. M. Armand, J. M. Tarascon, *Nature* 451 (2008) 652.

2. K. S. Kang , Y. S. Meng , J. Breger, C. P. Grey, G. Ceder, *Science* 311 (2006) 977.

3. J. B. Goodenough, K.S. Park, *J. Am. Chem. Soc.* 135 (2013) 1167.

4. J. Cabana, L. Monconduit, D. Larcher, M. R. Palacín, *Adv. Mater.* 22 (2010) E170.

5. K. T. Lee, Y. S. Jung, S. M. Oh, *J. Am. Chem. Soc.* 125 (2003) 5652.

6. G. Derrien, J. Hassoun, S. Panero, B. Scrosati, *Adv. Mater.* 19 (2007) 2336.

7. M.G. Kim, J. Cho, *Adv. Funct. Mater.* 19 (2010) 1497.

8. W. Xu, J. Wang, F. Ding, X. Chen, E. Nasybulin, Y. Zhang, J. Zhang, *Energy Environ. Sci.* 7 (2014) 513.

9. J. R. Dahn, T. Zheng, Y. H. Liu, J. S. Xue, *Science* 270 (1995) 590.

10. H. Azuma, H. Imoto, S. Yamada, K. Sekai, *J. Power Sources* 81 (1999) 1.

11. J. L. Tirado, *Mater. Sci. Eng. R* 40 (2003) 103.

12. Q. Wang, H. Li, L. Q. Chen, X. J. Huang, *Carbon* 39 (2001) 2211.

13. Q. Wang, H. Li, L. Q. Chen, X. J. Huang, *Solid State Ionics* 152 (2002) 43.

14. P. Roy, S. K. Srivastava, *J. Mater. Chem. A,* 3 (2015) 2454.

15. S.-M. Paek, E. Yoo, I. Honma, *Nano Lett.,* 9 (2009) 72.

16. Y. Idota, T. Kubota, A. Matsufuji, Y. Maekawa, T. Miyasaka, *Science* 276 (1997) 1395.

17. S. Ding, J. S. Chen, G. Qi, X. Duan, Z. Wang, E. P. Giannelis, L. A. Archer and X. W. Lou, *J. Am. Chem. Soc.* 133 (2011) 21.

18. Z. W. Pan, Z. R. Dai, Z. L. Wang, *Science* 291 (2001) 1947.

19. L. Vayssieres, M. Graetzel, *Angew. Chem. Int. Ed.* 43 (2004) 3666.

20. L. Zhao, M. Yosef, M. Steinhart, P. Goring, H. Hofmeister, U. Gosele, S. Schlecht, *Angew. Chem. Int. Ed.* 45 (2005) 311.

21. *Xiong Wen Lou*, *Yong Wang*, *Chongli Yuan*, *Jim Yang Lee*, and *Lynden A. Archer, Adv. Mater.* 18 (2006) 2325.

22. X. Lou, C. Li, L. A. Archer, *Adv. Mater.* 21 (2009) 2536.

23. U. K. Sen, S. Mitra, *ACS Appl. Mater. Interfaces* 5 (2013) 1240.

24. K. Zhang, H. J. Kim, X. J. Shi, J. T. Lee, J. M. Choi, M. S. Song and J. H. Park, *Inorg. Chem.* 52 (2013) 9807.

25. J. Xiao, D. W. Choi, L. Cosimbescu, P. Koech, J. Liu and J. P. Lemmon, *Chem. Mater.* 22 (2010) 4522.

26. M. Wang, G. D. Li, H. Y. Xu, Y. T. Qian and J. Yang, *ACS Appl. Mater. Interfaces* 5 (2013) 1003.

27. C. Q. Feng, L. F. Huang, Z. P. Guo and H. K. Liu, *Electrochem. Commun.* 9 (2007) 119.

28. G. X. Wang, S. Bewlay, J. Yao, H. K. Liu and S. X. Dou, *Electrochem. Solid-State Lett.* 7 (2004) A321.

29. J. T. Jang, S. Jeong, J. W. Seo, M. C. Kim, E. Sim, Y. Oh, S. Nam, B. Park and J. Cheon, *J. Am. Chem. Soc.* 133 (2011) 7636.

30. J. Liu, Y. Wen, P. A. Aken, J. Maier and Y. Yu, *J. Mater. Chem. A* 3 (2015) 5259.

31. J. Wang, L. Lu, M. Lotya, J. N. Coleman, S. Chou, H.-K. Liu, A. I. Minett, and J. Chen, *Adv. Energy Mater.* 3 (2013) 798.

32. J. Lu, C.-Y. Nan, L.-H. Li, Q. Peng, Y.-D. Li, *Nano Res.* 6 (2013) 55.

33. H.-S. Im, Y.-J. Cho, Y.-R. Lim, Ch.-S. Jung, D.M. Jang, J. Park, F. Shojaei, H.S. Kang, *ACS Nano.* 7 (2013) 11103.

34. H. Pan, Y. Hu and L. Chen, *Energy Environ. Sci.* 6 (2013) 2338.

35. D. Kim, E. Lee, M. Slater, W. Lu, S. Rood, C. S. Johnson, *Electrochem. Commun.* 18 (2012) 66.

36. V. Palomares, P. Serras, I. Villaluenga, K. B. Hueso, J. C. Gonzalez and T. Rojo, *Energy Environ. Sci.* 5 (2012) 5884.

37. Y. Wen, K. He, Y. Zhu, F. Han, Y. Xu, I. Matsuda, Y. Ishii, J Cumings, and C. Wang, *Nature Communications* 5(2014) 4033.

38. D. A. Stevens and J. R. Dahn, *J. Electrochem. Soc.* 147 (2000) 1271.

39. K. Gotoh, T. Ishikawa, S. Shimadzu, N. Yabuuchi, S. Komaba, K. Takeda, A. Goto, K. Deguchi, S. Ohki, K. Hashi, T. Shimizu and H. Ishida, *J. Power Sources* 225 (2013) 137.

40. Y. Bai, Z. Wang, C. Wu, R. Xu, F. Wu, Y. Liu, H. Li, Y. Li, J. Lu, and K. Amine, *ACS Appl. Mater. Interfaces* 7 (2015) 5598.

41. V. L. Chevrier and G. Ceder, *J. Electrochem. Soc.* 158 (2011) A1011.

42. S. Komaba, Y. Matsuura, T. Ishikawa, N. Yabuuchi, W. Murata and S. Kuze, *Electrochem. Commun.* 21 (2012) 65.

43. S. Komaba, T. Ishikawa, N. Yabuuchi, W. Murata, A. Ito and Y. Ohsawa, *ACS Appl. Mater. Interfaces* 3 (2011) 4165.

44. J. W. Wang, X. H. Liu, S. X. Mao, and J. Y. Huang, *Nano Lett.* 12 (2012) 5897.

45. Y. Liu, Y. Xu, Y. Zhu, J. N. Culver, C. A. Lundgren, K. Xu, and C. Wang, *ACS Nano*, 7 (2013) 3627.

46. H. Zhu, Z. Jia, Y. Chen, N. Weadock, J. Wan, O. Vaaland, X. Han, T. Li, and L. Hu, *Nano Lett.* 13 (2013) 3093.

47. Q. Sun, Q.-Q. Ren, H. Li and Z.-E. Fu, *Electrochem. Commun.* 13 (2011) 1462.

48. D. Su, H.-J. Ahn and G. Wang, *Chem. Commun.* 49 (2013) 3131.

49. Y. Kim, K.-H. Ha, S. M. Oh, and K. T. Lee, *Chem. Eur. J.* 20 (2014) 11980.

50. J. Park, J.-S. Kim, J.-W. Park, T.-H. Nam, K.-W. Kim, J.-H. Ahn, G. Wang, H.-J. Ahn, *Electrochimica Acta* 92 (2013) 427.

51. L. David, R. Bhandavat, G. Singh, ACS Nano 8 (2014) 1759.

52. S. H. Choi, Y. N. Ko, J.-K. Lee, Y. C. Kang, *Adv. Funct. Mater.* 25 (2015) 1780.

53. X. Xie, D. Su, S. Chen, J. Zhang, S. Dou, G. Wang, *Chem. Asian J.* 9 (2014) 1611.

54. V.Palomares, M. Casas-Cabanas, E. Castillo-Mart´ınez, M. H. Hanb and T.Rojo, *Energy Environ. Sci.* 6 (2013) 2312.

55. J.-S. Kim, H.-J. Ahn, H.-S. Ryu, D.-J. Kim, G.-B. Cho, K.-W. Kim, T.-H. Nam, J. H. Ahn, *J. Power Sources* 178 (2008) 852.

56. T.B. Kima, W.H. Jung, H.S. Ryu, K.W. Kim, J.H. Ahn, K.K. Cho, G.B. Cho, T.H. Nam, I.S. Ahn, H.J. Ahn, *J. Alloys Compd.* 449 (2008) 304.

57. B. Radisavljevic, *et al. Nature Nanotech.* 6 (2011) 147.

58. H. S. S. R. Matte, A. Gomathi, A. K. Manna, D. J. Late, R. Datta, S. K. Pati, and C. N. R. Rao, *Angew. Chem. Int. Ed.* 49 (2010) 4059.

59. Y. Tian, Y. He, Y. Zhu, *Mater. Chem. Phys.* 87 (2004) 87.

60. G. S. Bang, K. W. Nam, J. Y. Kim, J. Shin, J. W. Choi, and S.-Y. Choi, *ACS Appl. Mater. Interfaces* 6 (2014) 7084.

61. Lee, Y-H. *et al. Adv. Mater.* 24 (2012) 2320.

62. K. Chang, W. Chen, *J. Mater. Chem.* 21 (2011) 17175.

63. T. Stephenson, Z. Li, B. Olsen and D. Mitlin, *Energy Environ. Sci.* 7 (2014) 209.

64. Yang, L.Ch.; Wang, S.-N.; Mao, J.-J.; Deng, J.-W.; Gao, Q.-Sh.; Tang, Y.; Schmidt, O. G. *Adv. Mater.* 25 (2013) 1180.

65. Z. Liu, H. Deng, and P. P. Mukherjee, *ACS Appl. Mater. Interfaces* 7 (2015) 4000.

References

66. J. B. Goodenough and Y. Kim, *Chem. Mater.* 22 (2010) 587.

67. B. Kang, G. Ceder, *Nature* 458 (2009) 190.

68. K. T. Lee, Y. S. Jung, S. M. Oh, *J. Am. Chem. Soc.* 125 (2003) 5652.

69. G. Derrien, J. Hassoun, S. Panero, B. Scrosati, *Adv. Mater.* 19 (2007) 2336.

70. M. G. Kim, J. Cho, *Adv. Funct. Mater.* 19 (2010) 1497.

71. Y. Xu, Q. Liu, Y. Zhu, Y. Liu, A. Langrock, M. R. Zachariah, C. Wang, *Nano Lett.* 13 (2013) 470.

72. X. W. Lou, C. M. Li, L. A. Archer, *Adv. Mater.* 21 (2009) 2536.

73. J. Seo, J. Jang, S. Park, C. Kim, B. Park, J. Cheon, *Adv. Mater.* 20 (2008) 4269.

74. D. D. Vaughn II, O. D. Hentz, S. Chen, D. Wang and R. E. Schaak, *Chem. Commun.* 48 (2012) 5608.

75. J.O. Besenhard, J. Yang, M. Winter, *J. Power Sources* 68 (1997) 87.

76. W.-J. Zhang, *J. Power Sources* 196 (2011) 13.

77. H.S. Kim *et al. Electrochim. Acta* 54 (2009) 3606.

78. J.-W. Seo, et. al. *Adv. Mater.* 20 (2008) 4269.

79. J. Jiang, J. Liu, R. Ding, X. Ji, Y. Hu, X. Li, A. Hu, F. Wu, Z. Zhu, X. Huang, *J. Phys. Chem. C.* 114 (2010) 929.

80. J. Cai, Z. Li, P. Shen, *ACS Appl. Mater. Interfaces* 4 (2012) 4093.

81. J. Lu, C.-Y. Nan, L.-H. Li, Q. Peng, Y. Li, *Nano Res.* 6 (2013) 55.

82. H. S. Im, Y. J. Cho, Y. R. Lim, C. S. Jung, D. M. Jang, J. Park, F. Shojaei, and H. S. Kang, *ACS Nano* 7 (2013) 11103.

83. S. Biswas, S. Kar, S. Chaudhuri, *Appl. Surf. Sci.* 253 (2007) 9259.

84. B. Subramanian, C. Sanjeeviraja, M. Jayachandran, *Sol. Energy Mater. Sol. Cells* 79 (2003) 57.

85. J. Chao, Z. Wang, X. Xu, Q. Xiang, W. Song, G. Chen, J. Hu, D. Chen, *RSC Advances* 3 (2013) 2746.

86. M. Sevilla, A. B. Fuertes, *Carbon* 47 (2009) 2281.

87. V. Palomares, P. Serras, I. Villaluenga, K. B. Hueso, J. Carretero-González, T. Rojo, *Energy Environ. Sci.* 5 (2012) 5884.

88. S. P. Ong, V. L. Chevrier, G. Hautier, A. Jain, C. Moore, S. Kim, X. Ma, G. Ceder, *Energy Environ. Sci.* 4 (2011) 3680.

89. C. Luo, Y. Xu, Y. Zhu, Y. Liu, S. Zheng, Y. Liu, A. Langrock, C. Wang, *ACS Nano* 9 (2013) 8003.

90. M. Xie, R. Luo, J. Lu, R. Chen, F. Wu, X. Wang, C. Zhan, H. Wu, H. M. Albishri, A. S. Al-Bogami, D. A. El-Hady, K. Amine, *ACS Appl. Mater. Interfaces* 6 (2014) 17176.

91. J. W. Wang, X. H. Liu, S. X. Mao, J. Y. Huang, *Nano Lett.* 12 (2012) *12*, 5897.

92. S. M. Oh, S. T. Myung, J. Hassoun, B. Scrosati, Y. K. Sun, *Electrochem. Commun.* 22 (2012) 149.

93. S. Xin, Y. Yin, Y. Guo, L. Wan, *Adv. Mater.* 26 (2014) 1261.

94. Y. Jiang, M. Hu, D. Zhang, T. Yuan, W. Sun, B. Xu, M. Yan, *Nano Energy* 5 (2014) 60.

95. H. Song, N. Li, H. Cui, C. Wang, *Nano Energy* 4 (2014) 81.

96. K. Hong, L. Qie, R. Zeng, Z. Yi, W. Zhang, D. Wang, W. Yin, C. Wu, Q. Fan, W. Zhang, Y. Huang, *J. Mater. Chem. A* 2 (2014) 12733.

97. Y. Cao, L. Xiao, M. L. Sushko, W. Wang, B. Schwenzer, J. Xiao, Z. Nie, L. V. Saraf, Z. Yang, J. Liu, *Nano Lett.* 12 (2012) 3783.

98. J. Ding, H. Wang, Z. Li, A. Kohandehghan, K. Cui, Z. Xu, B. Zahiri, X. Tan, E. Lotfabad, B. C. Olsen, D. Mitlin, *ACS Nano* 7 (2013) 11004.

99. S. M. Oh, S. T. Myung, M. W. Jang, B. Scrosati, J. Hassoun, Y. K. Sun, *Phys. Chem. Chem. Phys.* 15 (2013) 3827.

100. H. Zhu, Z. Jia, Y. Chen, N. Weadock, J. Wan, O. Vaaland, X. Han, T. Li, L. Hu, *Nano Lett.* 13 (2013) 3093.

101. M. He, K. Kravchyk, M. Walter, M. V. Kovalenko, *Nano Lett.* 14 (2014) 1255.

102. Y. Jiang, M. Hu, D. Zhang, T. Yuan, W. Sun, B. Xu, M. Yan, *Nano Energy* 5 (2014) 60.

103. C. Deng, S. Zhang, Z. Dong, Y. Shang, *Nano Energy* 4 (2014) 49.

104. J. Wang, C. Luo, T. Gao, A. Langrock, A. C. Mignerey, C. Wang, *Small* 11 (2015) 473.

105. L. Wu, X. Hu, J. Qian, F. Pei, F. Wu, R. Mao, X. Ai, H. Yang, Y. Cao, *J. Mater.Chem. A* 1 (2013) 7181.

106. D. Y. Yu, P. V. Prikhodchenko, C. W. Mason, S. K. Batabyal, J. Gun, S. Sladkevich, A. G. Medvedev, O. Lev, *Nat. Commun.* 4 (2013) 2922.

107. B. Luo, Y. Fang, B. Wang, J. Zhou, H. Song, L. Zhi, *Energy Environ. Sci.* 5 (2012) 5226.

108. Y.Liu, H. Kang, L. Jiao, C. Chen, K. Cao, Y. Wang, H. Yuan, *Nanoscale*, 7 (2015) 1325.

109. S. Liu, X. Lu, J. Xie, G. Cao, T. Zhu, X. Zhao, *ACS Appl. Mater. Interfaces* 5 (2013) 1588.

110. B. Qu, C. Ma, G. Ji, C. Xu, J. Xu, Y. S. Meng, T. Wang, J. Y. Lee, *Adv. Mater.* 26 (2014) 3854.

111. P. Chen, Y. Su, H. Liu, Y. Wang, *ACS Appl. Mater. Interfaces* 5 (2013) 12073.

112. Z. Liu, H. Deng, P. P. Mukherjee, *ACS Appl. Mater. Interfaces.* 7 (2015) 4000.

113. G. Wang, J. Peng, L. Zhang, J. Zhang, B. Dai, M. Zhu, L. Xia, F. Yu, *J. Mater. Chem. A,* 3 (2015) 3659.

114. X. Xie, D. Su, S. Chen, J. Zhang, S. Dou, G. Wang, *Chem. Asian J.* 9 (2014) 1611.

115. Y. Zhang, P. Zhu, L. Huang, J. Xie, S. Zhang, G. Cao, X. Zhao, *Adv. Funct. Mater.* 25 (2015) 481.

116. T. Zhou, W. Pang, C. Zhang, J. Yang, Z. Chen, H. K. Liu, Z. Guo, *ACS Nano* 8 (2014) 8323.

117. D. G. Mead, J. C. Irwin, *Solid State Commun.* 20 (1976) 885.

118. C. Wang, K. Tang, Q. Yang, Y. Qian, *Chem. Phys. Lett.* 357 (2002) 371.

119. M. Sevilla, A. B. Fuertes, *Carbon* 47 (2009) 2281.

120. R. Bissessur, D. Schipper, *Mater. Lett.* 62 (2008) 1638.

121. X. Sun, Y. Li, *J. Colloid Interface Sci.* 291 (2005) 7.

122. Q. Wu, L. Jiao, J. Du, J. Yang, L. Guo, Y. Liu, Y. Wang, H. Yuan, *J. Power Sources* 239 (2013) 89.

123. C. Luo , Y. Zhu , Y. Wen , J. Wang , and C. Wang, *Adv. Funct. Mater.* 26 (2014) 4082.

124. C. Luo, Y. Xu, Y. Zhu, Y. Liu, S. Zheng, Y. Liu, A. Langrock, and C. Wang, *ACS Nano* 9 (2013) 8003.

125. C. Luo, Y. Zhu, T. Gao, Y. Xu, Y. Liu, J. Wang, C. Wang, *J. Power Sources* 250 (2014) 372.

126. A. Abouimrane, D. Dambournet, K.W. Chapman, P. J. Chupas, W. Weng, K. Amine, *J. Am. Chem. Soc.* 134 (2012) 4505.

127. V. Palomares, M. Casas-Cabanas, E. Castillo-Martınez, M. H. Hanb and T. Rojo, *Energy Environ. Sci.* 6 (2013) 2312.

128. N. Yabuuchi, M. Kajiyama, J. Iwatate, H. Nishikawa, S. Hitomi, R. Okuyama, R. Usui, Y. Yamada and S. Komaba, *Nat mater.* 11 (2012) 512.

129. D. A. Stevens and J. R. Dahn, *J. Electrochem. Soc.* 147 (2000) 1271.

130. Y. Liu, Y. Xu, Y. Zhu, J. Culver, C. Lundgren, K. Xu, C. Wang, *ACS Nano* 7 (2013) 3627.

131. Y. Zhu, X. Han, Y. Xu, Y. Liu, S. Zheng, K. Xu, L. Hu, and C. Wang, *ACS Nano* 7 (2013) 6378.

132. H. Xiong, M. D. Slater, M. Balasubramanian, C.S. Johnson, T. Rajh, *J. Phys. Chem. Lett.* 2 (2011) 2560.

133. Q. Sun, Q. Ren, H. Li, Z. Fu, *Electrochem. Commun.* 13 (2011) 1462.

134. L. Wu, X. Hu, J. Qian, F. Pei, F. Wu, R. Mao, X. Ai, H. Yang and Y. Cao, *J. Mater. Chem. A* 1 (2013) 7181.

135. L. Dai, D. W. Chang, J.-B. Baek, and W. Lu, *small* 8 (2012) 1130.

136. J. Ding, H. Wang, Z. Li, A. Kohandehghan, K. Cui, Z. Xu, B. Zahir, X. Tan, E. M. Lotfabad, B. C. Olsen, and D. Mitlin, *ACS Nano* 7 (2013) 11004.

137. Y. Cao, L. Xiao, M. L. Sushko, W. Wang, B. Schwenzer, J. Xiao, Z. Nie, L. V. Saraf, Z. Yang, J. Liu, *Nano Lett.* 12 (2012) 3783.

138. Y. Shi, Y. Wang, J. I. Wong, A. Y. S. Tan, C.-L. Hsu, L.-J. Li, Y.-C. Lu, H. Y. Yang *Sci. Rep.* 3 (2013) 2169.

139. Y. Wang, G. Xing, Z. J. Han, Y. Shi, J. I. Wong, Z. X. Huang, K. Ostrikov and H. Y. Yang, *Nanoscale* 6 (2014) 8884.

140. L. David, R. Bhandavat, and G. Singh, *ACS Nano* 8 (2014) 1759.

141. B. Radisavljevic, A. Radenovic, J. Brivio, V. Giacometti1 and A. Kis, *Nat. Nanotechnol.* 6 (2011) 147.

142. M. Chhowalla, H. S. Shin, G. Eda, L.-J. Li, K.-P. Loh, H. Zhang, *Nat. Chem.* 5 (2013) 263.

143. G. Du, Z. Guo, S. Wang, R. Zeng, Z. Chen, H. Liu, *Chem. Commun.* 46 (2010) 1106.

144. K. Chang, W. Chen, *Chem. Commun.* 47 (2011) 4252.

145. Y. Miki, Y. D. Nakazato, H. Ikuta, T. Uchida, M. Wakihara, *J. Power Sources* 54 (1995) 508.

146. L.Ch Yang, S.-N. Wang, J.-J. Mao, J.-W. Deng, Q.-Sh. Gao, Y. Tang, O. G. Schmidt, *Adv. Mater.* 25 (2013) 1180.

147. H. Hwang, H. Kim, J. Cho, *Nano Lett.* 11 (2011) 4826.

148. J. Wang, L. Lu, M. Lotya , J. N. Coleman, Sh.-L. Chou, H.-K. Liu, A. I. Minett, J. Chen, *Adv. Energy Mater.* 3 (2013) 798.

149. K. Chang, D. Geng, X. Li , J. Yang, Y. Tang , M. Cai, R. Li, X. Sun, *Adv. Energy Mater.* 3 (2013) 839.

150. X. Fang, X. Guo, Y. Mao, Ch. Hua, L. Shen, Y. Hu, Zh. Wang, F. Wu, L. Chen, *Chem. Asian J.* 7 (2012) 1013.

151. T. Stephenson, Zh. Li, B. Olsen, D. Mitlin, *Energy Environ. Sci.* 7 (2014) 209.

152. X. Cao, Y. Shi, W. Shi, X. Rui, Q. Yan , J. Kong, and H. Zhang, *Small,* 9 (2013) 3433.

153. K. Chang, W.-X. Chen, L. Ma, H. Li, H. Li, F. Huang, Z. Xu, Q. Zhang, J.-Y. Lee, *J. Mater. Chem.* 21 (2011) 6251.

154. G. Huang, T. Chen, W.-X. Chen, Z. Wang, K. Chang, L. Ma, F. Huang, D. Chen, J. Y. Lee, *Small* 9 (2013) 3693.

155. T. Yang, Y. Chen, B. Qu, L. Mei, D. Lei, H. Zhang, Q. Li, T. Wang, *Electrochimi. Acta* 115 (2014) 165.

156. B. C. Windom, W. G. Sawyer, D. W. Hahn, *Tribol Lett.* 42 (2011) 301.

157. M. Sevilla, A.B. Fuertes, *Carbon* 47 (2009) 2281.

158. Z. Wang, T. Chen, W. Chen, K. Chang, L. Ma, G. Huang, D. Chen and J. Y. Lee, *J. Mater. Chem. A,* 1 (2013) 2202.

159. S. M. Oh, S. T. Myung, M. W. Jang, B. Scrosati, J. Hassoun, Y. K. Sun, *Phys. Chem. Chem. Phys.* 15 (2013) 3827.

160. X. M. Sun and Y. D. Li, *J. Colloid Interface Sci.* 291 (2005) 7.

161. H. Du, C. T. Williams, A. D. Ebner, and J. A. Ritter, *Chem. Mater.* 22 (2010) 3519.

162. J. Xiao, X. Wang, X. Q. Yang, S. Xun, G. Liu, P. K. Koech, J. Liu and J. P. Lemmon, *Adv. Funct. Mater.* 21 (2011) 2840.

163. W.-H. Ryu, J.-W. Jung, K. Park, S.-J. Kima and I.-D. Kim, *Nanoscale* 6 (2014) 10975.

164. J. Wang, C. Luo, T. Gao, A. Langrock, A. C. Mignerey, C. Wang, *Small* 11 (2015) 473.

165. S. H. Choi, Y. N. Ko, J.-K. Lee, Y. C. Kang, *Adv. Funct. Mater.* 25 (2015) 1780.

166. X. Xie, Z. Ao, D. Su, J. Zhang, G. Wang, *Adv. Funct. Mater.* 25 (2015) 1393.

167. X. M. Sun, Y. D. Li, *J. Colloid Interface Sci.* 291 (2005) 7.

168. K. Chang, W.-X. Chen, L. Ma, H. Li, H. Li, F. Huang, Z. Xu, Q. Zhang, J.-Y. Lee, *J. Mater. Chem.* 21 (2011) 6251.

169. H. Hwang, H. Kim, J. Cho, *Nano Lett.* 11 (2011) 4826.

170. B. C. Windom, W. G. Sawyer, D. W. Hahn, *Tribol Lett.* 42 (2011) 301.

171. M. Sevilla, A. B. Fuertes, *Carbon* 47 (2009) 2281.

172. Z. Wang, T. Chen, W. Chen, K. Chang, L. Ma, G. Huang, D. Chen, J. Y. Lee, *J. Mater. Chem. A,* 1 (2013) 2202.

173. S. M. Oh, S. T. Myung, M. W. Jang, B. Scrosati, J. Hassoun, Y. K. Sun, *Phys. Chem. Chem. Phys.* 15 (2013) 3827.

174. G. Dong, X. Xiao, L. Zhang, Z. Ma, X. Bao, M. Peng, Q. Zhang and J. Qiu, *J. Mater. Chem.* 21 (2011) 2194.

175. X. Liu, Y. Liu, A. Kushima, S. Zhang, T. Zhu, J. Li, J. Huang, *Adv. Energy Mater*. 2 (2012) 722.

176. Y. Liu, F. Fan, J. Wang, Y. Liu, H. Chen, K. L. Jungjohann, Y. Xu, Y. Zhu, D. Bigio, T. Zhu, C. Wang, *Nano Lett.* 14 (2014) 3445.